

**DOKUZ EYLÜL UNIVERSITY**  
**GRADUATE SCHOOL OF NATURAL AND APPLIED SCIENCES**

**PREDICTIVE CONTROL OF GRID CONNECTED  
PHOTOVOLTAIC SYSTEM**



**by**

**Adnan SAMARJI**

**October, 2019**

**İZMİR**

# **PREDICTIVE CONTROL OF GRID CONNECTED PHOTOVOLTAIC SYSTEM**

**A Thesis Submitted to the  
Graduate School of Natural and Applied Sciences of Dokuz Eylül University  
In Partial Fulfillment of the Requirements for the Degree of Master of Science  
in Electrical and Electronics Engineering Program**



**by**

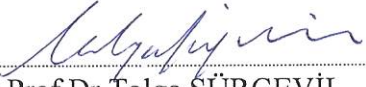
**Adnan SAMARJI**

**October, 2019**


**İZMİR**


## M.Sc THESIS EXAMINATION RESULT FORM

We have read the thesis entitled “**PREDICTIVE CONTROL OF GRID CONNECTED PHOTOVOLTAIC SYSTEM**” completed by **ADNAN SAMARJI** under supervision of **ASSIST.PROF.DR. TOLGA SÜRGEVİL** and we certify that in our opinion it is fully adequate, in scope and in quality, as a thesis for the degree of Master of Science.

  
Assist.Prof.Dr.Tolga SÜRGEVİL

Supervisor

  
Doç.Dr.Muthu BOZTERPE  
(Jury Member)

  
Dr.Öğr.Üye Abdül Balıkcı  
(Jury Member)

  
Prof.Dr. Kadriye ERTEKİN  
Director

Graduate School of Natural and Applied Sciences

## **ACKNOWLEDGMENTS**

I would like to take this opportunity to thank my previous advisor Prof.Dr.Eyup Akpinar for his patience and time he gave in which without his guidance I would have never been able to complete my master's thesis. With his expertise I became more familiar with how scientific research is carried out for which he played a leading role in my academic development.

I would also like to express my deepest gratitude to my new advisor Dr.Tolga Surgevil for his guidance, and Prof.Dr. Yesim Zoral for her full support for the success of my thesis.

I would like to take this opportunity also to express my deepest appreciation towards my family for their support, and love they gave for which without them, I wouldn't have had the opportunity to start and complete my journey in Turkey. I would like to show my undying love towards my mother who has been the backbone of my life from childhood. I would like to dedicate this achievement to my late father who has sacrificed everything for his children's education. Finally, I thank to Government of Turkey for their scholarship they bestowed upon me.

Adnan SAMARJI

# **PREDICTIVE CONTROL OF GRID CONNECTED PHOTOVOLTAIC SYSTEM**

## **ABSTRACT**

In this thesis, grid connected photovoltaic (PV) array with DC to DC boost converter, and DC /AC neutral point clamped (NPC) three level inverter has been analyzed. The DC to DC boost converter is used to extract the maximum power from the solar panels. The single phase three level inverter has been used to interface between the DC to DC converter and grid.

In this study, maximum power point tracking (MPPT) methodologies has been investigated and compared in which both the conventional perturb and observe (P&O), and the particle swarm optimization (PSO) methodologies have been introduced. The three-level inverter with its unique structure and gate signal operation gives a constant common mode voltage. The control of the output power of the inverter was carried out with orthogonal signal generation methodology in which proportional resonant controller (PR), and harmonic compensator controllers (HC) were used. The simulation model of the complete system has been designed and analyzed in the MATLAB/SIMULINK environment.

In addition, the predictive current control has been used to control the inductance current of the DC to DC boost converter during maximum power point tracking operation of the photovoltaic array. The fastness and robustness of various MPPT methodologies equipped with predictive current control has been demonstrated in the study. The duty controlled P&O and PSO algorithms, and voltage controlled P&O and PSO based predictive current control methods have been implemented and simulation of these methodologies has been carried out via MATLAB/Simulink.

**Keywords:** PV, Three level NPC inverter, common mode voltage, maximum power point tracking, predictive current control, particle swarm optimization, perturb and observe method, DC to DC boost converter, orthogonal signal generation

# KESTİRİLEBİLİR KONTROLLÜ ŞEBEKE BAĞLANTILI FOTOVOLTAİK SİSTEM

## ÖZ

Bu tezde, DC-DC yükseltici dönüştürücülü ve DC / AC nötr kenetlemeli (NPC) üç seviyeli eviricili şebekeye bağlı fotovoltaik (PV) dizisi analiz edilmiştir. DC-DC'ye yükseltici dönüştürücü, güneş panellerinden maksimum gücü çıkarmak için kullanılır. Tek fazlı üç seviye evirici, DC - DC çevirici ve şebeke arasında ara yüz oluşturmak için kullanılmıştır.

Bu çalışmada, maksimum güç noktası izleme (MPPT) metodolojileri araştırılmış, geleneksel değiştir ve gözlemle (P&O) ve parçacık sürüsü optimizasyonu (PSO) yöntemleri karşılaştırılmıştır. Üç seviyeli invertör kendine özgü anahtarlama yapısıyla sabit bir ortak mod voltajı sağlamaktadır. Evirici çıkış gücünün kontrolü, oransal rezonans ve harmonik kompensatör denetçilerinin kullanıldığı ortogonal sinyal üretim metodolojisi ile gerçekleştirilmiştir. Sistemin modellenmesi MATLAB / SIMULINK ortamında tasarlanmış ve analiz edilmiştir.

Ek olarak, fotovoltaik dizinin maksimum güç noktası takip işlemi sırasında DC-DC'ye yükseltici dönüştürücünün endüktans akımını kontrol etmek için kestirilebilir akım kontrolü kullanılmıştır. Çalışmada kestirilebilir akım kontrolü ile çalışan çeşitli MPPT metodolojilerinin hızları ve sağlamlığı gösterilmiştir. Görev zamanlı P&O ve PSO algoritmaları, ve gerilim tabanlı P&O ve PSO tabanlı kestirilebilir akım kontrol yöntemlerinin simülasyon modelleri oluşturulmuş ve bu yöntemlerin simülasyonları MATLAB/Simulink' te yapılmıştır.

**Anahtar Kelimeler:** PV, Üç seviye NPC evirici, Ortak mod gerilimi, Maksimum güç noktası takibi, Kestirilebilir akım kontrolü, Parçacık sürüsü optimizasyonu, Değiştir ve Gözlemle yöntemi, DC-DC yükseltici dönüştürücü, Ortogonal sinyal üretimi

## CONTENTS

	<b>Page</b>
M.Sc. THESIS EXAMINATION RESULT FORM.....	ii
ACKNOWLEDGMENTS .....	iii
ABSTRACT.....	iv
ÖZ.....	v
LIST OF FIGURES.....	ix
LIST OF TABLES.....	xiv

### **CHAPTER ONE - INTRODUCTION ..... 1**

### **CHAPTER TWO - DC-DC BOOST CONVERTER WITH PREDICTIVE CURRENT CONTROL.....7**

2.1 Boost Converter Analysis:.....	7
2.2 DC to DC Boost Converter for MPPT Operation: .....	9
2.3 Predictive Current Control of Boost Converter:.....	12

### **CHAPTER THREE - METHODOLOGIES IN MPPT ALGORITHM FOR PV ARRAY ..... 19**

3.1 Conventional Perturb and Observe Method .....	19
3.2 Particle Swarm Optimization-Based MPPT .....	20
3.3 The Flowchart of the Particle Swarm Optimization.....	24
3.4 Transfer Function Between Duty Cycle and Inductor Current .....	25
3.5 Operation of the Perturb and Observe MPPT Algorithm With the Boost converter.....	27
3.6 Selecting the Input Capacitor of Boost Converter with respect to the PV Panel.....	31
3.7 Simulation of PV array with duty controlled boost converter and resistive load.....	32
3.7.1 Simulation of PV array with duty based PO algorithm.....	34

3.7.2 Simulation of PV array with duty based PSO algorithm.....	38
3.8 Simulation of PV array with predictive current controlled boost converter and resistive load.....	42
3.8.1 MPPT Based Predictive Valley Current Control.....	43
3.8.1.1 Voltage oriented PO based predictive valley current control of PV array.....	44
3.8.1.2 Voltage oriented PSO based predictive valley current control of PV array.....	48
3.8.2 MPPT Based Predictive Average Current Control.....	52
3.8.2.1 Voltage oriented PO based predictive average current control of PV array.....	52
3.8.2.2 Voltage oriented PSO based predictive average current control of PV array.....	56
<b>CHAPTER FOUR - NEUTRAL POINT CLAMPED INVERTER.....</b>	<b>60</b>
4.1 Three level Inverter Approach.....	60
4.1.1 Selecting the proper DC bus link capacitance for NPC three-level Inverter.....	63
4.2 Common Mode Voltage of the Neutral Point Clamped Inverter: .....	64
4.3 Proportional Resonant Controller for the Grid-connected Operation: .....	67
4.4 Orthogonal Signal Generator (OSG):.....	70
<b>CHAPTER FIVE - GRID CONNECTED NEUTRAL POINT CLAMPED INVERTER WITH PV ARRAY.....</b>	<b>72</b>
5.1 Duty Cycle-based P&O and Neutral Point Clamped Inverter:.....	72
5.2 Duty Cycle-based PSO and Neutral Point Clamped Inverter: .....	75
5.3 Voltage Oriented P&O with predictive current control and Neutral Point Clamped Inverter.....	76
5.4 Voltage Oriented PSO with predictive current control and Neutral Point Clamped Inverter.....	79



<b>CHAPTER SIX - SIMULATION RESULTS.....</b>	<b>80</b>
6.1 Control of Inverter Connected to grid (OSG) .....	80
6.1.1 Implementing OSG with Inverter .....	86
6.2 Two Different MPPT Methods with Inverter Connected to the Grid .....	89
6.2.1 Duty Cycle Based Perturb and Observe .....	89
6.2.2 Duty Cycle Based Particle Swarm Optimization .....	93
6.2.3 Voltage Oriented Perturb and Observe Based Predictive Valley Current Control.....	97
6.2.4 Voltage Oriented PSO Based Predictive Valley Current Control .....	102
6.2.5 Voltage Oriented PO Based Predictive Average Current Control.....	106
6.2.6 Voltage Oriented PSO Based Predictive Average Current Control.....	111
<b>CHAPTER SEVEN – CONCLUSIONS.....</b>	<b>116</b>
<b>REFERENCES.....</b>	<b>118</b>

## LIST OF FIGURES

	<b>Page</b>
Figure 1.1 (a) Photovoltaic cell, (b) Photovoltaic Module.....	1
Figure 1.2 Equivalent circuit of a PV array .....	2
Figure 1.3 Nonlinear characteristic curves of PV panel at different irradiation levels and the temperature of 25 degrees. (Obtained from MATLAB/Simulink model.....	3
Figure 2.1 Boost converter equivalent circuit .....	7
Figure 2.2 (a) Gate signal of the switch S, (b) Inductance current of boost converter, (c) Inductance voltage of boost converter, (d) Current of output capacitance.....	8
Figure 2.3 Resistance between solar panel and DC -DC boost converter .....	9
Figure 2.4 MPPT curve illustration for boost converter .....	11
Figure 2.5 General structure of the predictive current controlled system.....	12
Figure 2.6 Trailing edge modulation.....	14
Figure 2.7 Leading edge modulation .....	14
Figure 2.8 Trailing triangle modulation .....	14
Figure 2.9 Boost converter states of operation.....	15
Figure 2.10 Valley current control of boost inductor.....	16
Figure 2.11 Average current control .....	17
Figure 3.1 Flow chart for conventional Hill Climbing type MPPT algorithm.....	20
Figure 3.2 PSO mechanism.....	21
Figure 3.3 (a) First iteration of the PSO operation projected on I-V curve of PV array, (b) Second iteration of the PSO operation projected on I-V curve of PV array,(c) Third iteration of the PSO operation projected on I-V curve of PV array.....	23
Figure 3.4 Flow chart of the PSO .....	24
Figure 3.5 BODE response of $T_{pi}(s)$ .....	26
Figure 3.6 Step response of inductance current with respect to duty cycle (perturbation 0.05) .....	27
Figure 3.7 Equivalent circuit of ideal boost converter for small signal analysis .....	28
Figure 3.8 Bode diagram of $G_{pv}sd$ .....	30

Figure 3.9 Step response of Gpvdsd .....	30
Figure 3.10 Capacitance between solar panel and DC –DC boost converter terminals.....	31
Figure 3.11 MATLAB Simulink Composition of PV array with Boost converter .....	32
Figure 3.12 MPPT Simulink block.....	33
Figure 3.13 Gate signal generation of the MPPT.....	33
Figure 3.14 Output voltage, duty cycle, and current of the PV array under constant 1kW/m <sup>2</sup> irradiation.....	35
Figure 3.15 Voltage output and inductance current of the boost converter.....	36
Figure 3.16 Power output of the PV array.....	37
Figure 3.17 Voltage and current outputs of the PV array.....	39
Figure 3.18 Output voltage and inductance current of boost converter.....	40
Figure 3.19 Active output power of the PV array.....	41
Figure 3.20 Particles of the PSO with their duty cycles.....	41
Figure 3.21 MATLAB Simulink Composition of PV array with Boost converter.....	42
Figure 3.22 Implementation of the voltage oriented MPPT algorithm.....	42
Figure 3.23 Predictive model valley control.....	44
Figure 3.24 Voltage and current output of the PV array.....	45
Figure 3.25 Output voltage and inductance current of boost converter.....	46
Figure 3.26 Active power output of the PV array .....	46
Figure 3.27 Equivalent resistance of the PV array .....	47
Figure 3.28 Reference output voltage of the MPPT algorithm.....	48
Figure 3.29 Voltage and current output of the PV array .....	49
Figure 3.30 Voltage output and inductance current of the boost converter .....	50
Figure 3.31 Active output power of the PV array .....	51
Figure 3.32 Particles of the PSO with their voltage values .....	51
Figure 3.33 Model of the predictive average current control .....	52
Figure 3.34 Voltage and current output of the PV array.....	53
Figure 3.35 Output voltage and inductance current of boost converter .....	54
Figure 3.36 Active output power of the PV array.....	55

Figure 3.37 Output reference voltage of the voltage oriented PO MPPT algorithm.....	55
Figure 3.38 Equivalent output resistance of the PV array .....	56
Figure 3.39 Voltage and current output of the PV array .....	57
Figure 3.40 Output voltage and inductance current of the boost converter.....	58
Figure 3.41 Active power output of the PV array.....	59
Figure 3.42 Particles of the PSO with their voltage values.....	59
Figure 4.1 Single phase 3 level neutral clamped inverter.....	61
Figure 4.2 In phase modulation of three level inverter.....	63
Figure 4.3 Equivalent Circuit of grid connected H Bridge based Inverter with PV array.....	64
Figure 4.4 (a) Active current path of positive half cycle of grid current, (b) Freewheeling current path of positive half cycle of grid current.....	66
Figure 4.5 (a) Active current path of negative half cycle of grid current, (b) Freewheeling current path of negative half cycle of grid current.....	67
Figure 4.6 Equivalent representation of a PR controller.....	67
Figure 4.7 Bode diagram for PR .....	69
Figure 4.8 Bode diagram for HC (3rd, 5th) .....	69
Figure 4.9 OSG control with power calculation .....	70
Figure 4.10 Active and reactive power control using OSG .....	71
Figure 5.1 General structure of the entire grid connected PV array with duty based PO MPPT algorithm.....	73
Figure 5.2 Gate signal generation of the duty based perturb and observe MPPT algorithm .....	74
Figure 5.3 Generation of inverter gate signals block .....	75
Figure 5.4 General structure of the entire grid connected PV array with duty based PSO MPPT algorithm.....	76
Figure 5.5 General structure of the entire grid connected PV array with voltage- oriented PO MPPT algorithm, and predictive current control.....	77
Figure 5.6 Predictive model block (Valley based).....	78
Figure 5.7 Predictive model block (Average based).....	78

Figure 5.8 General structure of the entire grid connected PV array with PSO MPPT algorithm, and predictive current control.....	79
Figure 6.1 Structure of three level inverter .....	81
Figure 6.2 The DC to AC three level inverter connected to grid.....	82
Figure 6.3 OSG with power calculation.....	83
Figure 6.4 Orthogonal System Generator .....	83
Figure 6.5 OSG scheme with independent active and reactive control .....	84
Figure 6.6 PR and HC controllers.....	85
Figure 6.7 Simulink PWM generator (3- level) block .....	85
Figure 6.8 In phase switching gate signals.....	86
Figure 6.9 Phase DC Gnd output voltages of 3 level inverter .....	87
Figure 6.10 Phase to phase inverter output voltage waveform .....	87
Figure 6.11 Common mode voltage waveform.....	87
Figure 6.12 Active and reactive output of three level inverter .....	88
Figure 6.13 Reference and inverter current waveforms.....	88
Figure 6.14 Calculated active and reactive power outputs of OSG .....	88
Figure 6.15 Grid connected PV array with both boost converter and NPC inverter..	89
Figure 6.16 PV array voltage and current output waveforms .....	90
Figure 6.17 Boost voltage and inductance current output waveforms.....	91
Figure 6.18 Grid current output waveform .....	91
Figure 6.19 Real output power of inverter connected to grid .....	92
Figure 6.20 PV array voltage and current output waveforms .....	94
Figure 6.21 Boost voltage and inductance current output waveform .....	95
Figure 6.22 Particle Swarm Particles w.r.t time.....	95
Figure 6.23 Real output power of inverter connected to grid .....	96
Figure 6.24 Grid current output waveform .....	96
Figure 6.25 PV array voltage and current output waveforms .....	98
Figure 6.26 Boost voltage and inductance current output waveforms.....	99
Figure 6.27 Predictive valley current control voltage reference output waveform (MPPT).....	100
Figure 6.28 Output real power of inverter connected to grid.....	101
Figure 6.29 PV array voltage and current output waveform.....	103

Figure 6.30 Boost voltage and inductance current output waveforms.....	104
Figure 6.31 Particle Swarm Particles w.r.t time.....	105
Figure 6.32 Output real power of inverter connected to grid.....	106
Figure 6.33 PV array voltage and current output waveforms .....	107
Figure 6.34 Boost voltage and inductance current output waveforms.....	108
Figure 6.35 Predictive valley current control voltage reference output waveform(PO MPPT).....	109
Figure 6.36 Output real power of inverter connected to grid.....	110
Figure 6.37 PV array voltage and current output waveform.....	112
Figure 6.38 Boost voltage and inductance current output waveforms.....	113
Figure 6.39 PSO Particles and reference voltage output w.r.t time .....	114
Figure 6.40 Output real power of inverter connected to grid.....	115

## LIST OF TABLES

	<b>Page</b>
Table 2.1 Critical constant and conversion ratio.....	10
Table 3.1 Parameters of the PV array with duty-controlled boost converter connected to resistive load.....	34
Table 3.2 Parameters of the PV array with predictive current- controlled boost converter connected to resistive load.....	43
Table 4.1 Switching sequence of three level inverter.....	61
Table 6.1 Parameters of the PV array with predictive current- controlled boost converter connected to resistive load.....	83
Table 6.2 Summary of the results obtained.....	115

## CHAPTER ONE

### INTRODUCTION

Solar panels have been the main focus of researchers for quite some time. In addition, the reduce in cost of manufacturing solar panels have led to a great deal of increase in the amount of research being conducted to optimize the solar panel efficiency in the maximum amount of power that can be extracted.

Solar panels are easy to be mounted especially in rural areas where the grid has not yet been installed which is considered one of its major advantages from its applications. The global demand towards solar energy is increasing due to the fact it's both economically and environmentally friendly in which it is estimated approximately 505.2 GW in 2018 and is projected to reach a level of 1270.5 GW by the end of 2022 (SolarPower Europe, 2018). With that put into prospective, the need to optimize algorithms that drive these solar panels to reach maximum output power being extracted has become a necessity for today's modern way of life.

Solar cells are p-n based injunctions that happen between silicon and other materials that upon exposure to irradiation from sunlight create a difference in voltage or a change in electron number counts which act as a current source component. The photovoltaic cell, and module are shown in Figure 1.1. (Durbaba, 2018).

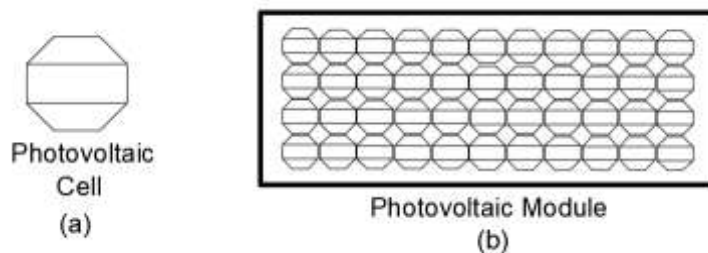


Figure 1.1 (a) Photovoltaic cell, (b) Photovoltaic Module



The equivalent circuit of the PV array is shown in Figure 1.2 (Femia et al, 2005).

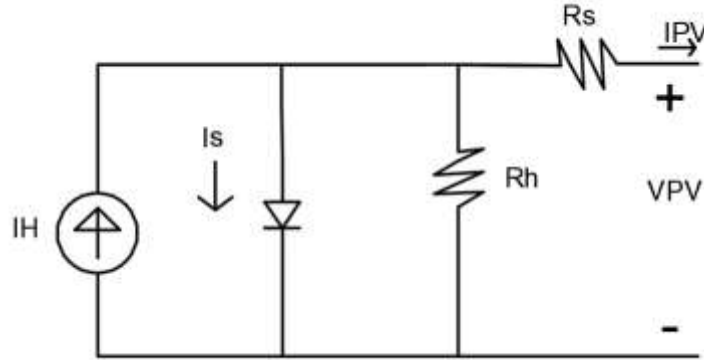


Figure 1.2 Equivalent circuit of a PV array

The relation between the output voltage of PV array  $V_{pv}$ , and PV output current  $I_{pv}$  is of the following equation (Femia et al, 2005):

$$I_{PV} = I_H - I_S \left[ e^{\left( \frac{V_{PV} + R_S I_{PV}}{\eta V_T} \right)} - 1 \right] - \frac{V_{PV} + R_S I_{PV}}{R_h} \quad (1.1)$$

where  $R_s$  is the series resistance,  $R_h$  is the shunt resistance,  $I_H$  is the light induced current,  $I_S$  is the diode saturation current,  $\eta$  is the diode ideality factor, and  $V_T$  is the thermal voltage.  $I_H$  depends on irradiation level and array temperature. For this reason the photovoltaic array has a nonlinear voltage and current characteristic with one maximum power point (MPP) attributed to a specific irradiation and temperature level as shown in Figure 1.3. This has been the main concern for researchers to be able to create an algorithm to drive the PV solar panel in tracking down this point. There are many algorithms in the literature that were developed for the sole purpose of being able to successfully track down the MPP, and extracting the energy as such increasing the efficiency of the PV solar array.

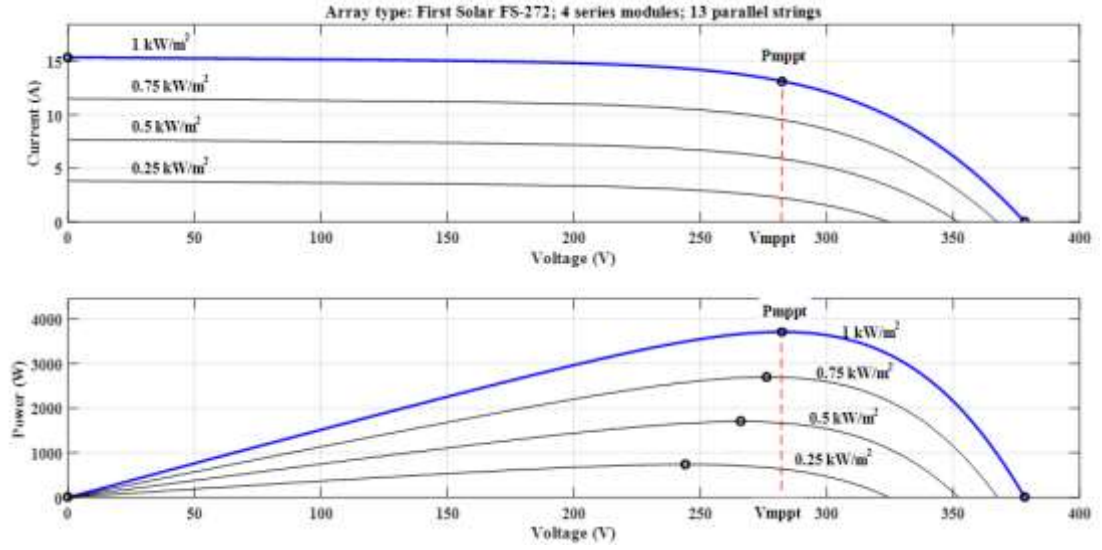


Figure 1.3 Nonlinear characteristic curves of PV panel at different irradiation levels and the temperature of 25 degrees (Obtained from MATLAB/Simulink model)

Due to the fact that PV array is completely dependent on its environment with the change in sunlight intensity during the day, maximum power point tracking (MPPT) algorithm is used to track the MPP point and extract the energy from the solar panel efficiently. The DC to DC converters can be used to track this maximum power upon connection with the solar panel. These converters are able to change the input impedance of the converter equating it with MPP impedance of the PV panel (Enrique et al, 2006; Durbaba, 2018). Various types of the DC to DC converters controlled under MPPT techniques have been researched. Moreover, researchers are increasingly interested in implementing MPPT algorithms with predictive control techniques, in order to obtain a shorter transient time with less steady state error concerning PV power output. Recently, a study was conducted concerning the predictive current control of boost converter with two different voltage oriented MPPT algorithms, namely perturb and observe (P&O) and particle swarm optimization (PSO) (Durbaba, 2018).

The solar panel generates DC power in which in order for it to deliver direct active power to any AC load or grid, it is essential to connect the solar panel to an inverter for DC to AC energy conversion. Researchers have been quite interested for the last few decades with regards to which inverter is optimum for grid tied operations. There are various types of inverters for example two level, three level inverters in which each

type has its own unique combination of switches and bridges to follow its own signal switching. There are standards in which the inverter must meet for which grid tied PV application can be possible. In addition, demands from the PV array must be met from which the voltage fluctuations at PV terminals must not exceed a certain level so as not to effect the efficiency of the PV array which leads to loss in power output (Kjaer et al, 2005). For PV grid tied applications, omitting the transformer is very beneficial in which it reduces the cost, and increases efficiency the overall system. Usually the consequence is that it leads to circulation of leakage current because of the common mode voltage variations which leads to safety hazards (Durbaba, 2018; Gonzalez et al, 2008). One method to provide constant common mode voltage is to use three-level inverters which utilize the neutral level found between its two capacitors for clamping the diodes (Gonzalez et al, 2008). The first three level inverter ever examined with PWM implementation was back in 1981 in which it introduced a new methodology for PWM switching to eliminate the 5<sup>th</sup> and 7<sup>th</sup> harmonics created (Nabae et al, 1981).

The objectives of this thesis are to design and simulate PV system that is forced to operate around the maximum power point using various MPPT algorithms such as Perturb and Observe methodology, and Particle Swarm Optimization methodology. The PV system will be connected to the grid and synchronized using two stage system consisting of a DC to DC boost converter and dc to ac three level inverter. Predictive current control will be also implemented on the boost converter for further investigation on which is the optimum methodology for MPPT operation. Based on the simulation results, the comparative study of various MPPT algorithms with the utilization of predictive current control methods an optimum methodology will be concluded for two staged grid tied PV arrays. A study will be carried out to investigate the source of occurrence of 2<sup>nd</sup> order fluctuations on the output waveforms of the PV system upon duty cycle disturbance, and how to damp out these fluctuations successfully. In addition, there will be a brief investigation regarding common mode voltage, and which gate signal pattern will be adopted on the three level inverter to achieve constant common mode voltage. The study will take into consideration the settling time, power output of the system, and steady state power fluctuation percentage as criteria for choosing the optimum methodology. The simulation results

will be within the MATLAB/ SIMULINK environment in which both design and implementation of the system will be dealt within its constraints. The contents of the thesis are organized as follows:

In chapter two, DC to DC converter is covered specifically the boost converter. In this section, a study will be induced on how the converter parameters are designed, and how the converter mechanism works connected to the PV array. In addition, in this section predictive current control will be covered in which all three types of predictive current control will be mentioned as well as a detailed study on how implementation of both valley and average predictive current can be applied to the system.

In chapter three, conventional P&O as well as the PSO is covered in which the PSO is considered as one of the MPPT algorithms that is recently used in PV systems for maximum power tracking. This section will illustrate how the particle swarm methodology works, demonstrating its unique mechanism, and showing its advantages and disadvantages with regards to switching frequency and power tracking. The simulations of the PO and PSO algorithms with duty control and predictive current control were constructed and tested in MATLAB/SIMULINK. In addition, a unique study will cover the converter's components effect on the entire system in which fluctuations that are of 2<sup>nd</sup> order created by duty cycle disturbances of the boost converter on the PV voltage and current. These fluctuations nature will be examined thoroughly to find an optimum solution for PV MPPT operation.

In chapter four, the neutral point clamped (NPC) three level inverter will be discussed showing how the gate signals are obtained in which a brief study will be conducted on how its unique gate signal firing sequence creates a constant common mode voltage. In addition, the orthogonal system generator (OSG) control methodology will be evaluated as such to show how active and reactive power can be controlled independently with the help of PI (proportional integrator), PR (proportional resonant integrator), and HC (harmonic compensators).

In chapter five, the whole system will be brought together in which the power that is delivered from the PV array will be controlled by the OSG model and fed to the grid via the three-level inverter. The system will be comprised of two stages in which the first stage consists of PV array connected to the DC to DC boost converter and operated by MPPT algorithms. The second stage will be DC to AC in which the boost converter output will be directly connected to a three-level inverter that is directly synchronized to the grid.

In chapter six, all simulations that were conducted via MATLAB/SIMULINK will be presented within the scope of comparing between various MPPT methodologies. The results will be analyzed as such to bring forward conclusions regarding which methodology is more convenient for two staged grid tied PV arrays, and also with regards to the various control methodologies utilized in DC to DC converter with predictive current control and DC to AC inverter with OSG control. These remarks will be made in the conclusion section

## CHAPTER TWO

### DC-DC BOOST CONVERTER WITH PREDICTIVE CURRENT CONTROL

#### 2.1 Boost Converter Analysis

The DC to DC boost converter has one switch  $S$  with an uncontrolled diode as shown in the equivalent circuit of the boost converter in Figure 2.1. The output of the boost converter is higher than its input. The energy stored in the inductor  $L$  when the switch is closed is directed towards the boost's output terminals when the switch is open (Durbaba, 2018; Hart, 2011).

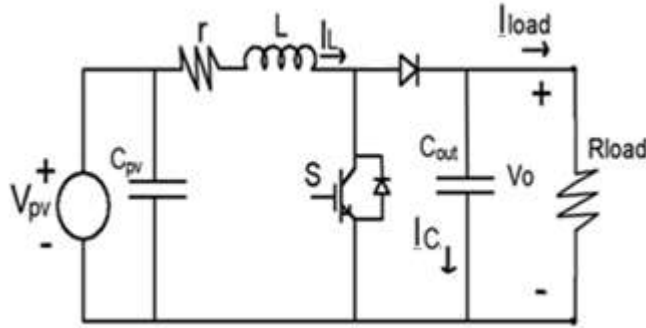


Figure 2.1 Boost converter equivalent circuit

As the boost converter is working in continuous conduction mode as shown in Figure 2.2 , with  $D$  representing the duty cycle the following equations can be obtained accordingly (Hart, 2011):

The output voltage with respect to the input voltage is

$$V_o = \frac{V_{pv}}{(1-D)} \quad (2.1)$$

The average inductor current is

$$I_L = \frac{V_{pv}}{(R_{load}) * (1-D)^2} \quad (2.2)$$

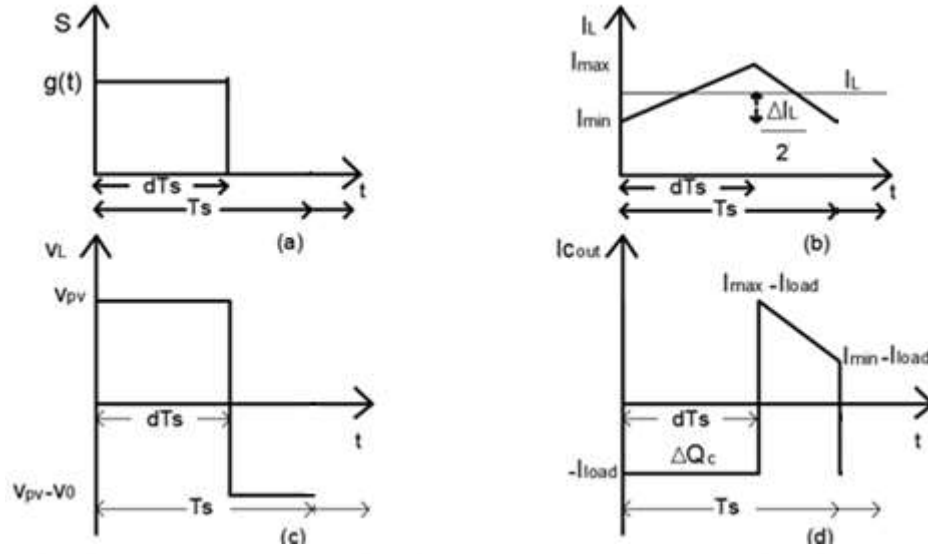


Figure 2.2 (a) Gate signal of the switch S, (b) Inductance current of boost converter, (c) Inductance voltage of boost converter, (d) Current of output capacitance.

The ripple current  $\Delta I_L$  with respect to duty cycle  $D$ , input voltage  $V_{pv}$ , inductance of coil  $L$ , and switching period  $T_s$ :

$$\Delta I_L = V_{pv} * \frac{D * T_s}{L} \quad (2.3)$$

$$I_{max} = I_L + \frac{\Delta I_L}{2} \quad (2.4)$$

$$I_{min} = I_L - \frac{\Delta I_L}{2} \quad (2.5)$$

Thus the ripple voltage  $\Delta v_o$  with respect to duty cycle  $D$ , load resistance  $R_{load}$ , switching period  $T_s$ , and the capacitance of output capacitor  $C_{out}$  can be expressed as follows :

$$\Delta v_o = \frac{\Delta Q_c}{C_{out}} = \frac{V_o * D * T_s}{R_{load} C_{out}} \quad (2.6)$$

$$\Delta v_o = V_{pv} * \frac{D * T_s}{(1-D) * (R_{load} * C_{out})} \quad (2.7)$$

where  $Q_c$  is the stored charge in the output capacitance  $C_{out}$ .

The minimum coil inductance value  $L_{min}$  for continuous conduction mode of operation is :

$$L_{\min} = (D * R_{\text{load}}) * \frac{(1-D)^2 * T_s}{2} \quad (2.8)$$

## 2.2 DC to DC Boost Converter for MPPT Operation

In order to extract maximum power from the PV array, the MPPT system injects a resistance value to the output of the PV array. By doing so, the equivalent resistance seen at the input terminals of the boost converter will be equal to the equivalent resistance of the solar array operating at MPP. This equivalent resistance  $R_{\text{MPP}}$  is the division of the voltage to the current of the PV  $V_{\text{MPP}}/I_{\text{MPP}}$ . During the process of MPPT operation the boost converter changes the duty cycle  $D$  to alter the resistance at the output of the PV array as shown in Figure 2.3. Here,  $R_{\text{load}}$  represents the equivalent resistance of the load connected to the output terminals of the boost converter, and  $R_i$  represents the input equivalent resistance between the input terminals of the boost converter. (Enrique et al, 2006; Durbaba, 2018).

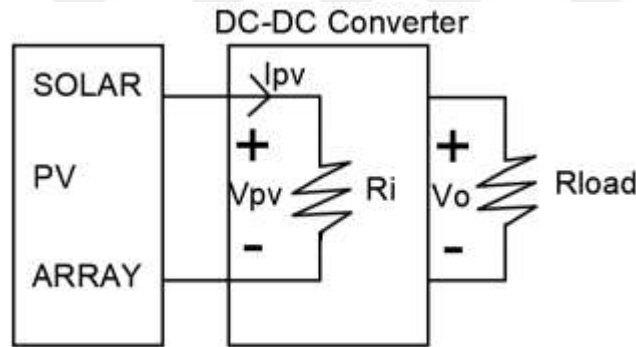


Figure 2.3 Resistance between solar panel and DC -DC boost converter

Generally all DC to DC converters have critical operating points in which beyond it they will begin operating in discontinuous conduction mode leaving the inductance current null for a fraction of the switching period. Table 2.1 shows both the critical constant of the DC to DC boost converter with respect to the duty cycle  $D$ , and the conversion ratio between the input resistance and the load resistance assuming continuous conduction mode criteria (CCM) is met. (Enrique et al, 2006).



Table 2.1 Critical constant and conversion ratio

Converter	$K_{critical}$	$R_i$ (CCM)
Boost	$D*(1-D)^2$	$R_{LOAD}*(1-D)^2$

$K_{operation}$  is the system's own unique critical constant. It is directly related to the switching frequency or switching period  $T_s$ , the inductance  $L_{eq}$  and the load resistance seen between the output terminal of the DC to DC boost converter as follows:

$$K_{operation} = 2 * \frac{L_{eq}}{R_{load} * T_s} \quad (2.9)$$

For example, Boost converter's parameters are given as follows :

$L_{eq}=5$  mH ,  $T_s= 0.0001$  sec,  $R_{LOAD}= 43.24 \Omega$  (3700 watts resistive load at 400 V ), and  $D=1/3$  (considering the largest factor possible) yields to the below constants thus ensuring that the system is operating in CCM:

$$K_{operation} = 2.31 \gg K_{critical}=0.1481$$

Figure 2.4 introduces a concept in MPPT operation called 'non-capture zone' in which during the boost converter operation , if the equivalent resistance seen on the input terminals of the DC to DC boost converter  $R_i$  is not matching  $R_{MPP}$  as defined earlier , the system will not be able to extract maximum power from the PV array. Depending on the value of the duty cycle  $D$  of which the boost converter is operating at , the resistance value of  $R_i$  is aimed to match  $R_{mpp}$ . For this reason  $R_{load}$  should not be chosen to be less than  $R_{mpp}$  since the system will not be able to track to track the MPP since the system operates in the 'non-capture zone' pointed out in Figure 2.4. This has to do with the mechanism of the boost converter that deals with being able to only amplify the voltage to a certain level (Enrique et al, 2006).

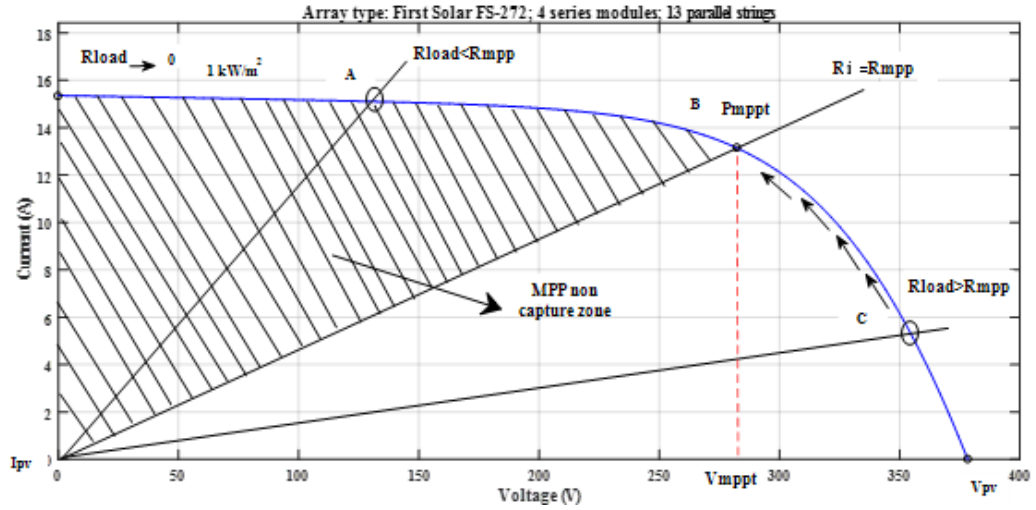


Figure 2.4 MPPT curve illustration for boost converter

According to the I-V curve of the pv panel array shown in Figure 2.4 it can be seen clearly that the maximum point of operation has a specific voltage and current value for which maximum power can be extracted from the solar panels.

For operation at  $1 \text{ kW/m}^2$  irradiance and  $25^\circ\text{C}$ , MPPT point is :  $P_{\text{active}} = 3700 \text{ W}$  at  $282.2 \text{ V}$  and  $13.14 \text{ A}$ .  $R_{\text{pv}}$  is the input equivalent resistance of the PV array seen on the input of the boost converter.

$$R_{\text{pv}} = \frac{v^2}{P_{\text{active}}} \quad (2.10)$$

$R_{\text{MPP}}$  can be found using equation 2.10 gives the following:

$$R_{\text{MPP}} (1\text{kw/m}^2) = 21.476 \Omega$$

### 2.3 Predictive Current Control of Boost Converter

In this thesis the predictive current control is employed to drive the DC to DC boost converter to extract the maximum active power from the PV array via voltage oriented MPPT algorithms. A comparative study will be held between the conventional PO algorithm and the PSO algorithm in which both methodologies will provide the reference point on the nonlinear I-V characteristic curve of the PV array for operation. A purely resistive load is used for the study in which the general structure of the whole topology is shown in Figure 2.5 with  $v^*$  being the reference voltage. (Durbaba, 2018).

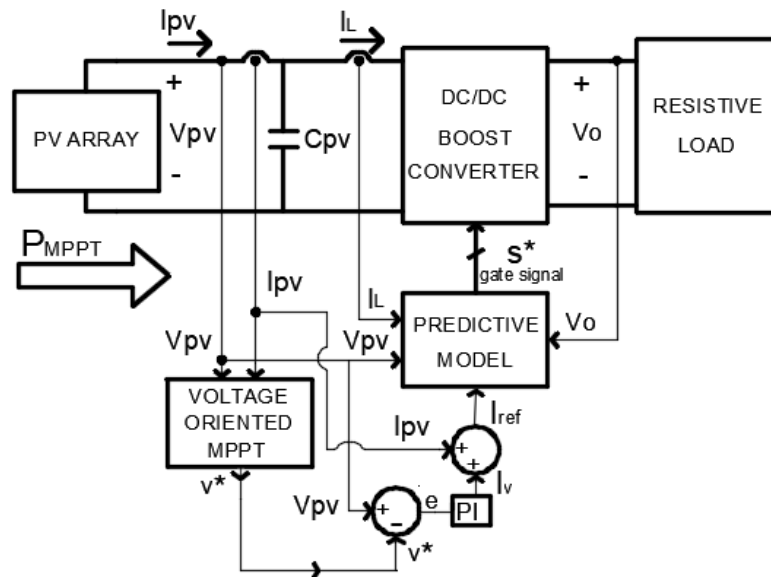


Figure 2.5 General structure of the predictive current controlled system

When the voltage oriented MPPT algorithm is used, a PI controller is necessary for obtaining the reference current  $I_{ref}$  from the reference voltage of the MPPT algorithm for the predictive model to work around as shown in Figure 2.5. As the algorithm tracks down the MPP, a reference duty cycle or in the case of voltage oriented MPPT, a reference voltage level will be provided as a reference point for the predictive model to work on. The PV output voltage  $V_{pv}$  is subtracted from the reference voltage  $v^*$  in which the error  $e$  between them is put as input to the PI controller. The addition of the output of the PI controller  $I_v$  with the output current of the PV array  $I_{pv}$  will provide

the reference current that the predictive model will follow to control the inductance current accordingly (Durbaba, 2018).

In general there are 3 types of control methodologies in which each methodology targets the sampled valley, peak, and average inductance current of the boost converter respectively. Each methodology requires a suitable modulation as such to give gate signals to the DC-DC converter according to the sampled inductance current of the boost converter (Kakosimos et al, 2013). In Figure 2.6 the trailing edge modulation  $C_1$  is utilized for predictive control in which the control signal  $V_{con}$  is compared with the sawtooth. During the sampling time period  $T_s$ , when the control signal is higher than that of  $C_1$ , the gate signal sent to the DC to DC boost converter is high otherwise the gate signal will be low for the whole sampling period  $T_s$ . When the gate signal is in high, the time interval is depicted as  $dT_s$  which is the conduction sampling time period. In Figure 2.7 the leading edge modulation  $C_1$  is compared with the control signal  $V_{con}$  in which the gate signal is null whenever  $C_1$  amplitude is greater than that of  $V_{con}$ . This time period is depicted as  $(1-d)T_s$  which represents part of the sampling time period  $T_s$  where the switching diode is on. For the valley current control the trailing edge modulation is suitable since when used the sampled current at each switching period is the valley inductance current. Unlike the peak current control in which a leading edge modulation is suitable since when used the sampled current at each switching period is the peak inductance current. However the average current control a different approach is needed. Trailing triangular modulation shown in Figure 2.8 can be used for the average value control of inductance current (Chen et al, 2003; Durbaba, 2018).

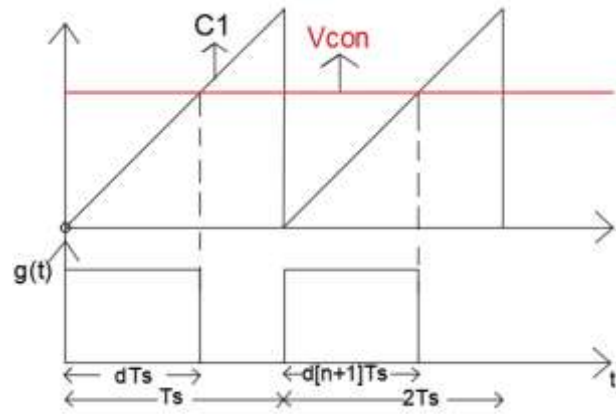


Figure 2.6 Trailing edge modulation

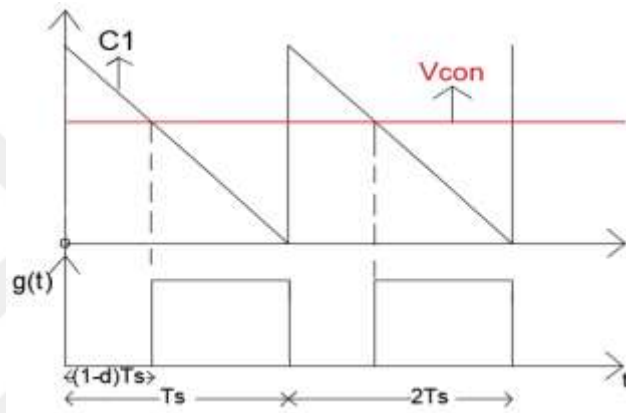


Figure 2.7 Leading edge modulation

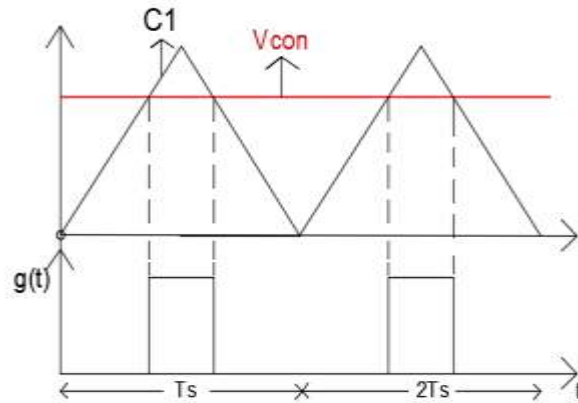


Figure 2.8 Trailing triangle modulation

The inductance current can be controlled via predictive current control according to the switch states. The switch states are shown in Figure 2.9 (Durbaba, 2018).

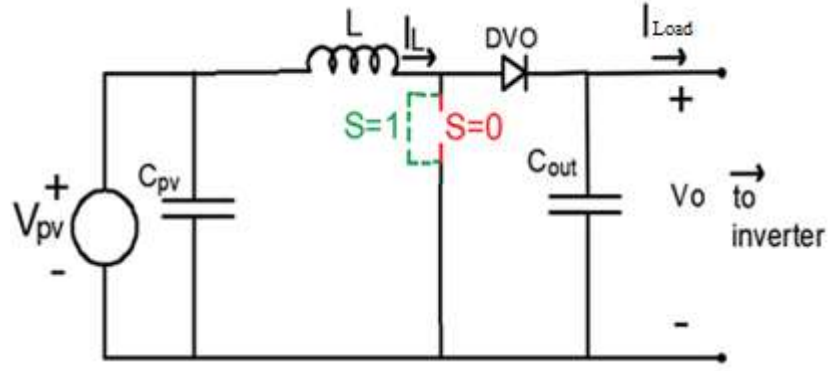


Figure 2.9 Boost Converter States of Operation

If the switch  $S=1$

$$\frac{L \cdot d[i_L]}{dt} = V_{pv} \quad (2.11)$$

If the switch  $S=0$

$$\frac{L \cdot d[i_L]}{dt} = V_{pv} - v_o \quad (2.12)$$

The above equations can both be expressed in discrete time as follows:

$$i_L[n+1] - i_L[n] = v_{pv}[n] * \frac{T_s}{L} \quad (2.13)$$

$$i_L[n+1] - i_L[n] = (v_{pv}[n] - v_o[n]) * \left(\frac{T_s}{L}\right) \quad (2.14)$$

The overall schematic is to sample the coil current waveform from the boost converter in which using trailing edge modulation as seen in Figure 2.10 , gate signals can be provided for predictive control operation. The input and output voltage can be considered constant due to the small sampling time period thus the sampled inductor current  $i_L[n]$  at time  $nT_s$  can be found as function of the previous inductor current  $i_L[n-1]$ . In conclusion duty cycle can be predicted from the input and output voltage with the sampled inductor current, in which the duty cycle found represents one step or two step horizon of the predicted inductance current as follows (Kakosimos et al ,2013; Durbaba ,2018):

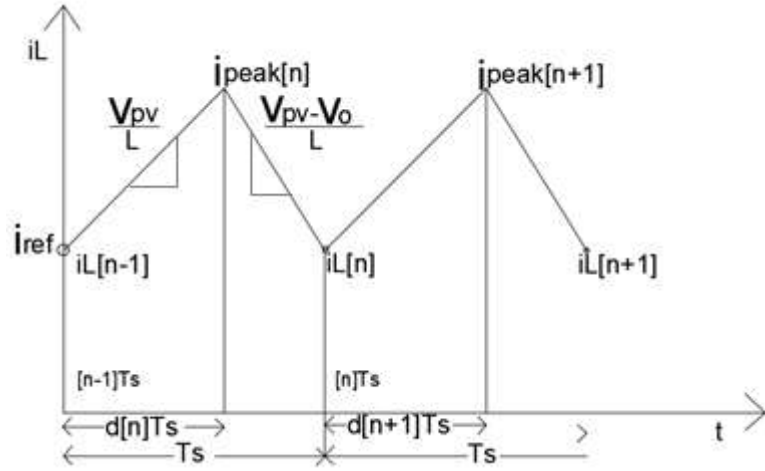


Figure 2.10 Valley current control of boost inductor

One step horizon inductor current can expressed as the following:

$$i_L[n] = i_L[n-1] + v_{pv} * d[n] * \frac{T_s}{L} + (v_{pv} - v_o) * d'[n] * \frac{T_s}{L} \quad (2.15)$$

where  $d'[n] = 1 - d[n]$ . Substituting in Equation 2.15 gives:

$$i_L[n] = i_L[n-1] + (v_{pv}) * \frac{T_s}{L} - (v_o) * d'[n] * \frac{T_s}{L} \quad (2.16)$$

Extending the equation for two step horizon operation using Equation 2.15 gives:

$$i_L[n+1] = i_L[n-1] + (2 * v_{pv}) * \frac{T_s}{L} - (v_o) * d'[n] * \frac{T_s}{L} - (v_o) * d'[n+1] * \frac{T_s}{L} \quad (2.17)$$

Now solving for  $d[n+1]$  the control equation 2.18 necessary for predictive valley current control is obtained in which predictive current control operation using two-step horizon prediction (Chen, 2003; Durbaba, 2018).

$$d[n+1] = 2 - d[n] - \frac{L * (i_L[n-1] - i_{ref})}{V_o * T_s} - \frac{2 * v_{pv}}{v_o} \quad (2.18)$$

Average predictive current control utilizes the trailing edge modulation as well to control the average value of the inductance current however unlike the predictive valley current control, the average predictive control samples one average period of the inductance current as shown in Figure 2.11 (Chen et al, 2003; Durbaba, 2018).

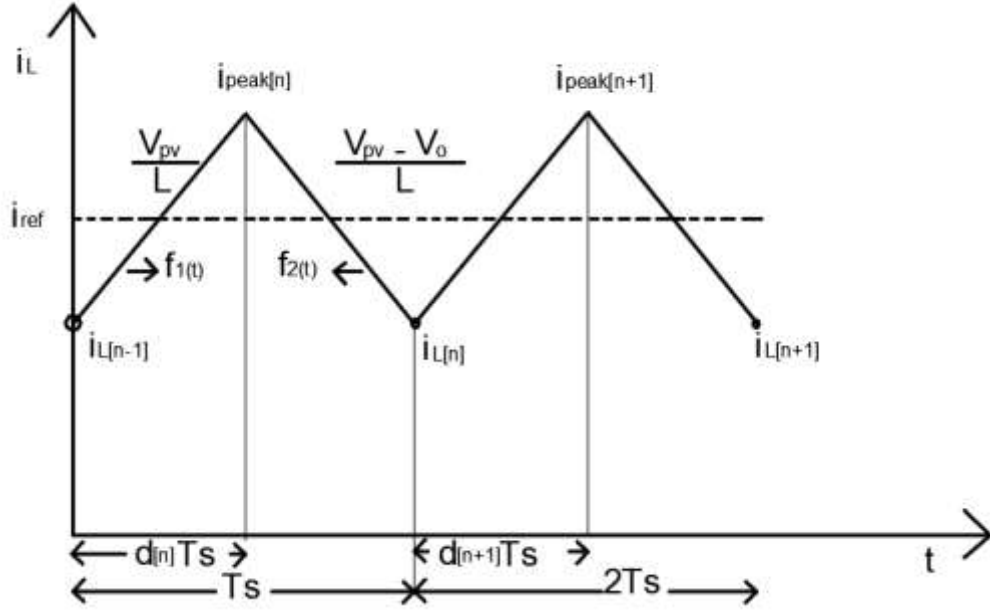


Figure 2.11 Average current control

Considering the function of the periodic wave to be  $f_k(t) = a_k * t + b_k$  then the average value is equal to integral from 0 to  $T_s$   $\langle f_k(t) \rangle = \frac{1}{T_s} \int f_k(t)$ . By using both  $f_1(t)$  and  $f_2(t)$  in the integration process the following average reference current can be obtained (Durbaba, 2018):

$$\langle i_L(t) \rangle = (a_1 - a_2) \left( \frac{T_s}{2} \right) (d[n+1])^2 + b_1 d[n+1] + b_2 - b_2 d[n+1] + \frac{a T_s}{2} \quad (2.19)$$

$$a_1 = \frac{v_{pv}}{L}, \quad a_2 = \frac{v_{pv} - v_o}{L}, \quad b_1 = i[n], \quad b_2 = \frac{v_o * d[n+1] * T_s}{L} + i[n]$$

Substituting the above variables with the average inductor current gives equation 2.20 which is nonlinear and will create computational problems in which it is best to



constrain from using it especially at switching frequencies that are in the thousands of hertz:

$$\langle i_{\text{ref}} \rangle = -\left(\frac{V_o * T_s}{2L}\right) * (d[n+1])^2 + i[n] + \frac{v_{pv} * T_s}{2L} + \left(\frac{V_o * T_s}{L}\right) * (d[n+1])^1 - \left(\frac{V_o * T_s}{2L}\right) \quad (2.20)$$

Linearization can be obtained using the two following equations with equation 2.21 representing the valley control of boost converter for one step horizon predictive control, and equation 2.22 representing the duty cycle for continuous conduction state. :

$$i_L[n+1] = i_L[n] + (v_{pv}) * \frac{T_s}{L} - (v_o) * d'[n+1] * \frac{T_s}{L} \quad (2.21)$$

$$d = 1 - \frac{v_{pv}}{v_o} \quad (2.22)$$

By substituting the equations 2.21, and 2.22 in the  $i_{\text{ref}}$  the average reference current equation can be obtained for predictive operation as follows:

$$i_{\text{ref}} = \left(\frac{v_{pv} * T_s}{L}\right) * \left(\frac{3}{2} - \frac{v_{pv}}{2v_o}\right) + i[n] - \left(\frac{v_o * T_s}{L}\right) + \frac{v_{pv} * d[n+1] * T_s}{L} \quad (2.23)$$

Solving for duty cycle gives equation 2.24 which represents the one step predictive average current control modulation with trailing edge triangular signal used in comparative manner, and gate signals can be obtained for the boost converter to operate correctly (Durbaba, 2018).

$$d[n+1] = 1 - \left(\frac{v_{pv}}{2v_o}\right) * \left(3 - \frac{v_{pv}}{v_o}\right) + \frac{L * (i_{\text{ref}} - i[n])}{v_o * T_s} \quad (2.24)$$

### **CHAPTER THREE**

#### **METHODOLOGIES IN MPPT ALGORITHM FOR PV ARRAY**

In PV solar panels the most important issue to be addressed is the I-V curve or the nonlinear relation between the current short circuited and the open circuit voltage of the PV which gives different power outputs for different radiations and temperatures. The first type of algorithm examined is the perturb and observe method, which relies on the perturbation of voltage or current using the present and previous operating power points. If  $\Delta P = P - P_{old}$  is positive the direction or the duty cycle of the DC converter will be positive and vice versa thus reaching the maximum point of power. Despite the algorithm being simple, the success of P&O method depends on the tracking speed and the oscillations around the MPP. A small value perturbation decreases the oscillations but reduces tracking speed. Another disadvantage of P&O is that during severe change of irradiation, the algorithm may lose its direction while tracking the MPP. The P&O MPPT algorithm can perturb directly the duty cycle as well thus simplifying the control unlike voltage oriented MPPT shown in Section 2.3. With no use of the PI loop, the approach is fairly simple. Second type of MPPT algorithm is the particle swarm optimization in which it is used instead of the conventional P&O to locate and lock the MPP at a higher or faster pace thus being more robust (Ishaque et al, 2012). However, its effectiveness is directly related with the search frequency.

In this thesis the conventional PSO algorithm will be investigated in which a comparative study will be made between the PSO and the conventional P&O MPPT algorithm. In addition to both algorithms will be used to equip the predictive current control to maneuver through the I-V PV array curve and deliver active power from the PV array.

### 3.1 Conventional Perturb and Observe Method

The algorithm changes the duty cycle by a fixed step size with the direction of the derivative of the power. The perturbation direction is changed if  $P_{(k)} < P_{(k-1)}$ , which means  $\Delta P$  the tracking is not towards the MPP. The tracking point is moving alongside the non-linear characteristic curve of the PV array as shown in Figure 2.4. Figure 3.1 represents the flowchart of the perturbation based Hill Climbing algorithm showing its simplicity. Using the duty cycle incrimination and identifying the PV array output voltage and current values, the maximum power point can be identified with incremental step changes in the duty cycle to reach MPP. This can be expressed as follows (Ishaque et al, 2012):

$$d_i^{k+1} = d_i^k + \phi_i^{k+1} \text{ if } P > P_{old} \quad (3.1)$$

$$d_i^{k+1} = d_i^k - \phi_i^{k+1} \text{ if } P < P_{old} \quad (3.2)$$

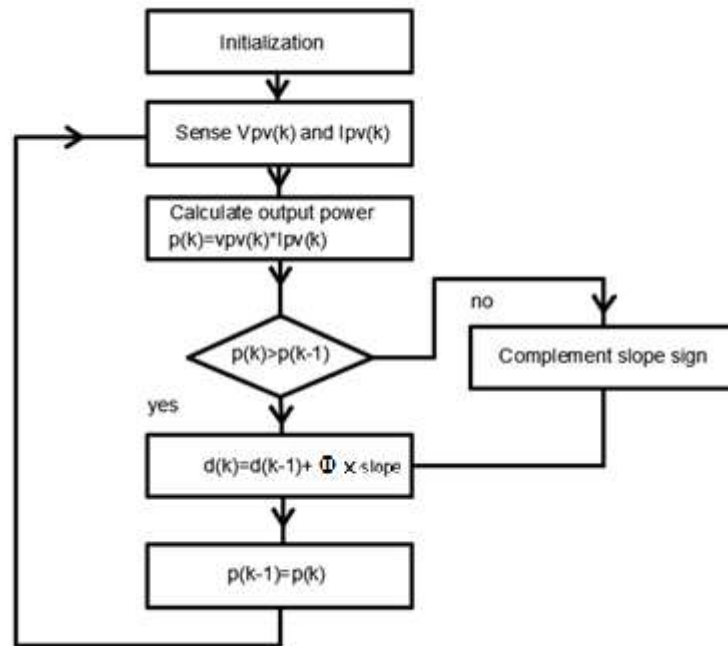


Figure 3.1 Flow chart for conventional Hill Climbing type MPPT algorithm

### 3.2 Particle Swarm Optimization-Based MPPT

The method is simple in concept and is inspired from the behavior of birds in which they fly in flocks. The neighboring bird will influence the others to a certain extent that the pack will reach their destination via teamwork effort. The method is based on the same concept in which a finite number of particles which are named agents are used. Each particle has its own duty cycle which is randomly created from a number ranging between 0 and 1. From those duty cycles randomly created a focus on the power generated is observed and  $P_{best}$  and  $G_{best}$  are assigned accordingly for the first iteration. Afterwards the duty cycle is changed according to each of the particles  $P_{best}$ ,  $G_{best}$ 's position on the P-V curvature. The change in duty cycle is applied according to equations 3.3, and 3.5. The proposed duty cycles' powers are calculated. Afterwards  $P_{best}$ , and  $G_{best}$  are reassigned according to their respective powers with  $G_{best}$  having the highest power thus the agents represent the local best powers, while one agent represents the global best power generated from its respective duty cycle.  $\omega$  is the internal inertia of the system with  $r_1, r_2$  two random numbers from 0 to 1, and  $c_1, c_2$  are acceleration coefficients. Finally  $\phi_i^k$  represent the duty cycle of the agents at the  $k^{th}$  iteration while  $\phi_i^k$  represents the velocity of the  $k^{th}$  iteration at which the duty cycle will be changed accordingly. Figure 3.2 shows the mechanism of the PSO (Ishaque et al, 2012).

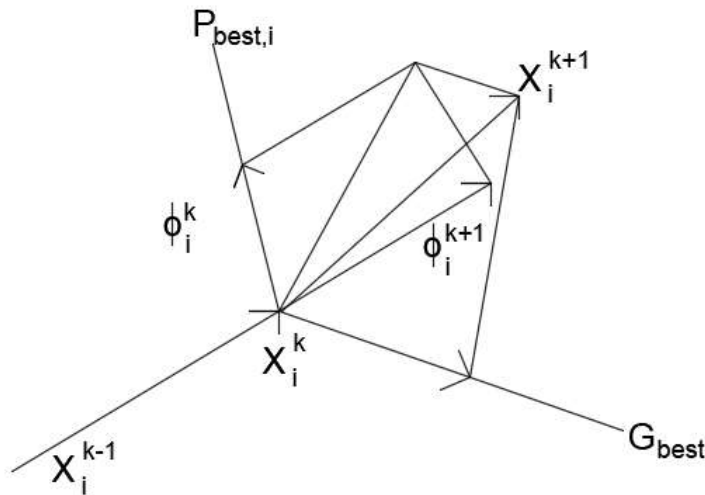


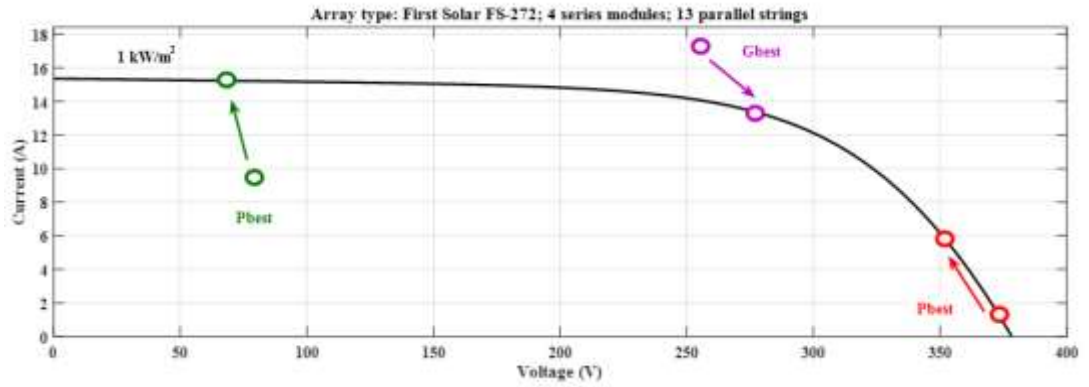
Figure 3.2 PSO mechanism

$$\phi_i^{k+1} = \omega \phi_i^k + c_1 r_1 [P_{best_i} - x_i^k] + c_2 r_2 [G_{best} - x_i^k] \quad (3.3)$$

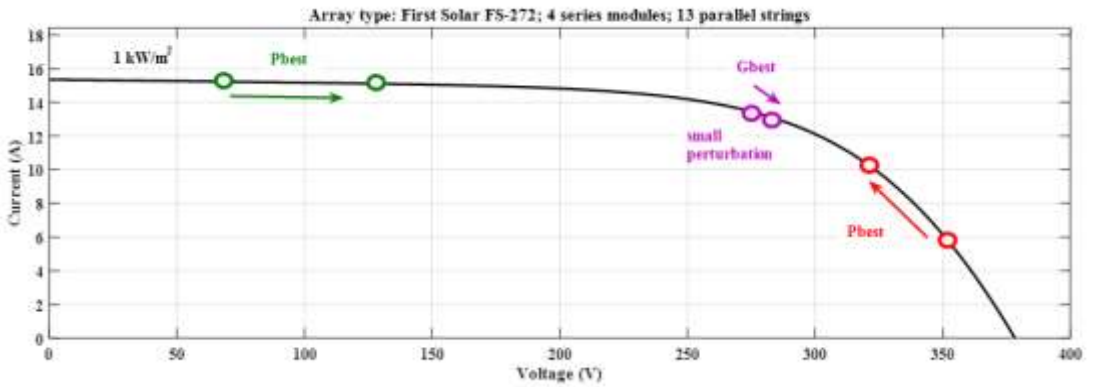
$$x_i^{k+1} = x_i^k + \phi_i^{k+1} \quad (3.4)$$

$$d_i^{k+1} = d_i^k + \phi_i^{k+1} \quad (3.5)$$

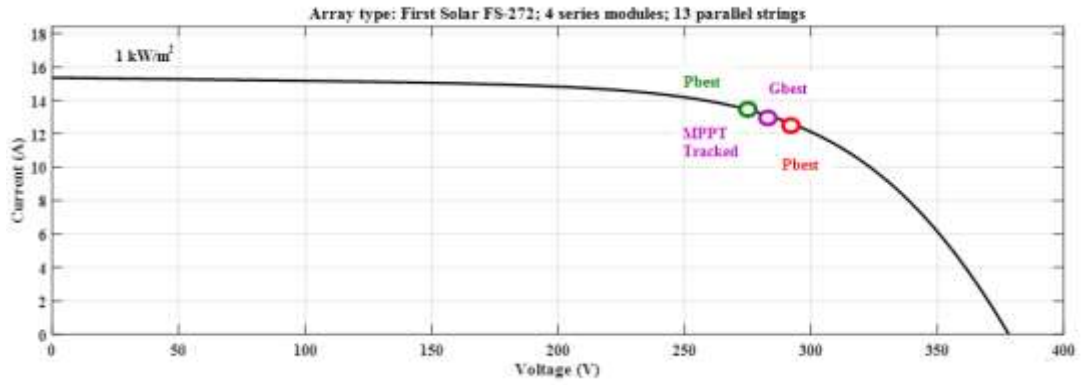
A general view can be observed on how the PSO approaches MPP with its own unique particles of duty cycles. In Figure 3.3 (a) first iteration is occurring and the particles are approaching in which  $G_{best}$  is one of the particles that has the highest output active power. In Figure 3.3 (b) the second iteration is occurring and due to the factor  $P_{best} - P_{previous}$ , and  $G_{best} - G_{previous}$  are both zero, the velocity will be null and exploration process will be held on stall, thus a small perturbation is introduced. In Figure 3.3 (c) the third iteration has successfully carried out all particles close to the MPP with one having the highest active power being found as  $G_{best}$ . It is worth noting that the duty based particle swarm optimization technique can be voltage driven with the PV voltage being searched instead of the duty cycle. For implementing this methodology to various current based applications such as predictive current control, this voltage driven PSO requires a PI controller for which its input is the subtraction between the output reference voltage  $v^*$  and the output voltage of the PV array  $V_{pv}$ . The output of the PI controller is added to the output current of the PV array  $I_{pv}$  which in turn represents the reference current obtained from particle swarm MPPT operation as explained in Section 2.3.



(a)



(b)



(c)

Figure 3.3 (a) First iteration of the PSO operation projected on I-V curve of PV array, (b) Second operation of the PSO operation projected on I-V curve of PV array, (c) Third iteration of the PSO operation projected on I-V curve of PV array

### 3.3 The Flowchart of the Particle Swarm Optimization

In Figure 3.5 the flowchart of the complete particle swarm optimization schematics is shown in which at the start of the program the particles are launched towards the DC to DC converter acting as independent duty cycles. Afterwards the particles begin to affect each other with their own position after assigning  $P_{best}$ , and  $G_{best}$ . Boundaries are checked in which no violation has occurred for the weight of the acceleration coefficient and the particles are re-launched to the system. The process is carried on for a limited number of iterations which is a convergence criterion, in which MPP will be successfully tracked via  $G_{best}$ , with the other particles  $P_{best}$  close to their target. The converter is tracking MPP with two different slopes using  $P_{best}$  and  $G_{best}$ , as a result its operating faster and more robust. Once steady state is reached the method will not cause any fluctuations due to the fact that the velocity used for perturbation will be entirely null (Ishaque et al, 2012).

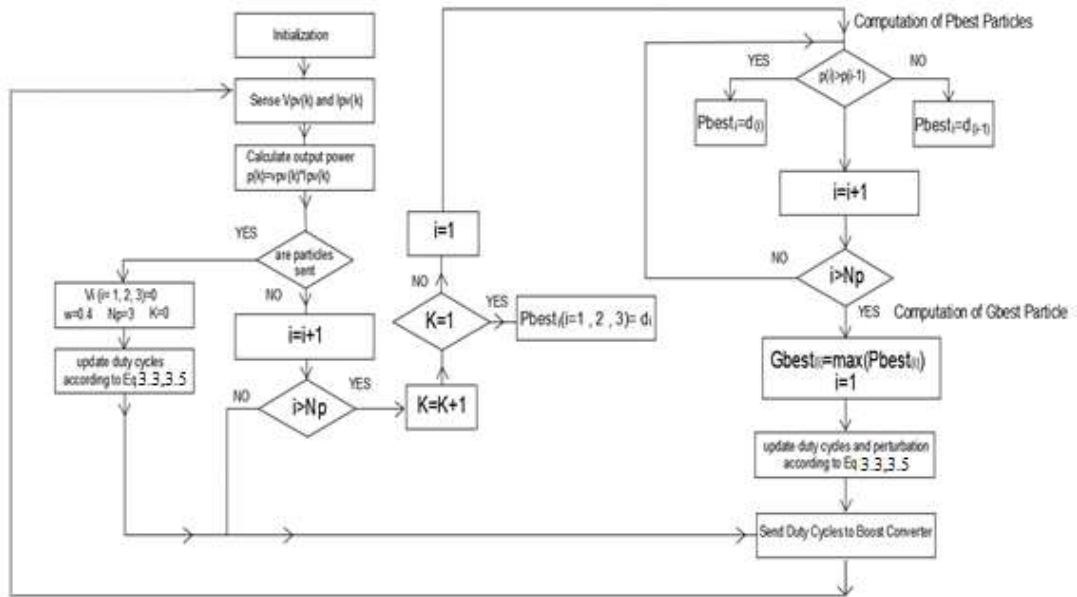


Figure 3.4 Flow chart of the PSO

### 3.4 Transfer Function Between Duty Cycle and Inductor Current

In the DC to DC boost converter while as operating in continuous conduction mode(CCM), there has been realized a relation between the inductor current response with respect to the small duty cycle variation. As far as the boost converter analyzation is put into perspective, this relation can be illustrated into a transfer function comprised of a combination of series and parallel capacitor , inductor, and resistance which make up the components of the system.

There are also transfer function relations regarding the change in output voltage of the DC to DC boost converter with respect to the inductor current as well ,but in this thesis the focus will be mainly on the repeating oscillation that exists in the inductor current with respect to the duty cycle for which using PO MPPT algorithm the duty cycle is continously changed even though reaching steady state operation Taking into consideration the internal resistance  $r$  of the coil  $L$ , and neglecting all the other component's internal resistance the following small signal transfer function between the inductor current and duty cycle variation is obtained (Bryant et al, 2004; 2005).

$$T_{pi(s)} = \frac{I_L}{d} = T_{pix} * \frac{s + \omega_{zi}}{s^2 + 2\zeta\omega_n s + \omega_n^2} \quad (3.6)$$

$$T_{pix} = \frac{V_O}{L} \quad (3.7)$$

$$\omega_{zi} = \frac{1}{C_{out} * \left(\frac{R_{Load}}{2}\right)} \quad (3.8)$$

$$\omega_n = \sqrt{\frac{(1-D)^2 * R_{Load} + r}{LC(R_{Load})}} \quad (3.9)$$

$$\zeta = \frac{C_{out}[r(R_{Load})] + L}{2\sqrt{LC_{out}(R_{Load})[r + (1-D)^2 R_{Load}]}} \quad (3.10)$$



Considering  $L=0.005$  H,  $C_{out}=0.00277$  F,  $R_{load}=43.24$   $\Omega$ ,  $r=0.2$   $\Omega$  which is the internal resistance of the inductor,  $V_O=400$  V, and  $D=0.295$  gives the following:

$$T_{pix} = 80000$$

$$\omega_{zi} = 16.698 \frac{\text{rad}}{\text{sec}}$$

$$\omega_n = 190.316 \frac{\text{rad}}{\text{sec}}$$

$$\zeta = 0.127$$

Using MATLAB SIMULINK the following bode diagram and step response were able to be acquired by the transfer function  $T_{pi}(s)$  in which it is worth to be noted that due to the fact that  $\omega_{zi} < \omega_n$  for this reason the fluctuations are of 2<sup>nd</sup> order nature (Bryant et al,2004; Bryant et al ,2005). In Figure 3.5 the bode diagram shows the 2<sup>nd</sup> order fluctuations that occur on the inductance current with each disturbance on the operating duty cycle of the boost converter with Figure 3.6, illustrating the step response with perturbation being 0.05 .

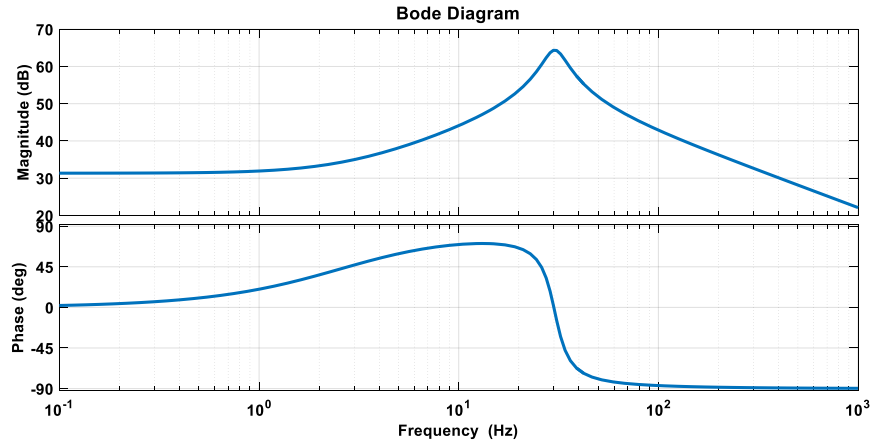


Figure 3.5 BODE response of  $T_{pi}(s)$

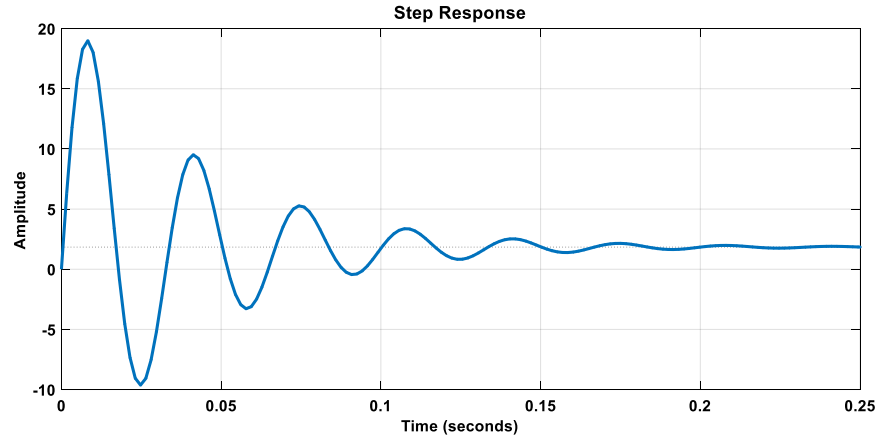


Figure 3.6 Step response of inductance current with respect to duty cycle (perturbation 0.05)

### 3.5 Operation of the Perturb and Observe MPPT Algorithm With the Boost Converter

The DC to DC converter extracts the active power from the solar panel by alternating the load equivalent resistance using the duty cycle. With this concept put into perspective the major drawback of the conventional PO MPPT algorithm is its continuous duty cycle variation even when reaching steady state. Each disturbance creates 2<sup>nd</sup> order fluctuations on the boost converter all the way to the PV outputs thus creating power fluctuations and leading to the confusion of the MPPT algorithm in tracking the maximum power point. Assuming the boost converter is both ideal and it is working in continuous conduction mode, Figure 3.7 which is the equivalent circuit of small signal duty modulation of a PV connected to an ideal boost converter can be analyzed under the small signal disturbance. The transfer function between the array voltage and duty cycle is given in (3.11) as  $G_{pv(s)}^d$  representing the 2<sup>nd</sup> order fluctuations that occur in the system (Femia et al, 2005).

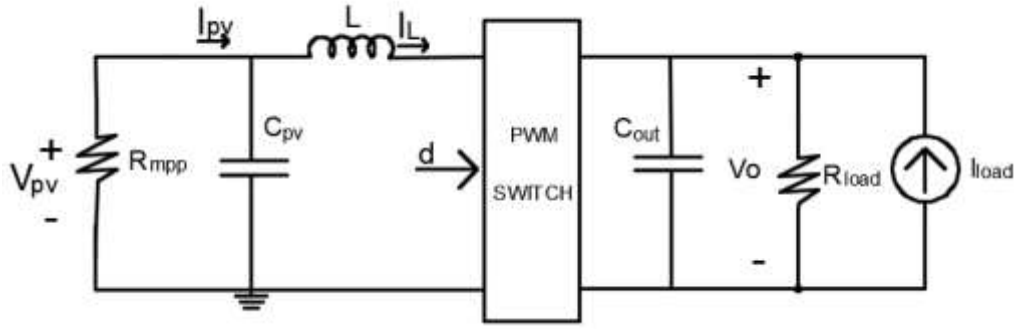


Figure 3.7 Equivalent circuit of ideal boost converter for small signal analysis

The transfer function  $G_{pv(s)}^d$  with ideal boost converter is of the following:

$$G_{pv(s)}^d = \frac{\mu * \omega_n}{s^2 + 2\xi\omega_n * s + \omega_n^2} \quad (3.11)$$

$$\mu = -V_0 \quad (3.12)$$

$$\omega_n = \sqrt{\frac{1}{LC_{pv}}} \quad (3.13)$$

$$\xi = \frac{\sqrt{\frac{L}{C_{pv}}}}{2R_{mpp}} \quad (3.14)$$

$I_L$  is the inductance current,  $I_{pv}$ , and  $V_{pv}$  are the current and voltage outputs of the PV array respectively.  $V_0$  is the voltage output of the boost converter with  $I_{load}$  being the current of the load.  $C_{pv}$ , and  $C_{out}$  are the input and output capacitance of the boost converter's terminals respectively.  $R_{mpp}$ , and  $R_{load}$  are the equivalent resistance of the input and output terminals of the boost converter respectively. Finally,  $d$  is small duty cycle variation on the PWM switch.  $\xi$  damping factor dependent on both the boost converter parameters,  $\varepsilon$  is the threshold in which a value of 0.1 is generally used for consideration of the transient over, and the PV array equivalent resistance operating at a specific irradiance and temperature for MPPT operation  $R_{MPP}$ . For the MPPT operation to run smooth with minimum fluctuations occurring in the system, the MPPT frequency should be selected according to both the PV array being used, and the boost converter's components. Time constant  $T_{(\xi)}$  can be expressed as follows and delay of disturbance can be selected above this time constant for minimum fluctuation (Femia et al, 2005) :

$$T_{(\xi)} = -\frac{1}{\xi * \omega_n} \ln(\varepsilon) \quad (3.15)$$

Considering the system's components from boost converter parameter to irradiance and temperature level effects on the value of  $R_{MPP}$  gives  $L=0.005$  H,  $C_{pv}=3.705$   $\mu$ F (explained in Section 3.6),  $V_o=400$  V , and  $R_{MPP}$  ( $1\text{kW/m}^2$ )  $=21.476$   $\Omega$  which in part yields to the following:

$$\omega_n = 7347.183 \frac{\text{rad}}{\text{sec}}$$

$$\xi = 0.855$$

$$T_{(\xi)} = 0.000366 \text{ s}$$

Due to the intrinsic transient oscillations of the PV system, the PO methodology can loose track of the MPP. To avoid this problem and avoid these 2<sup>nd</sup> order oscillations the MPPT operating frequency or the MPPT period should be chosen as such  $T_{mppt} \geq T_{(\xi)}$  ,and taking into consideration duty cycle variation to be of low value constant  $\Delta d$  . Choosing  $T_{mppt}=0.001$  will yield to a search frequency of 1000 Hz that is considered a proper value for the above mentioned conditions of operation for as to avoid these 2<sup>nd</sup> order fluctuations ,and the duty cycle remains only oscillating between three values  $[d_{MPP}- \Delta d, d_{MPP}, d_{MPP}+ \Delta d]$ . In Figure 3.8 the bode digaram represents the 2<sup>nd</sup> order flucuations that occur in all of the voltage and current outputs of the PV as well as the boost converter with each small signal disturbance on the operating duty cycle of the boost converter ,and Figure 3.9 illustrating the step response as well with duty cycle perturbation being 0.05.

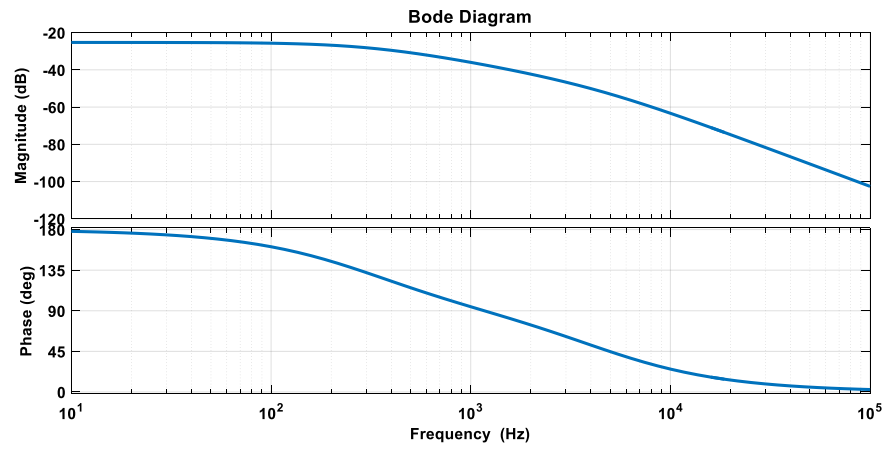


Figure 3.8 Bode diagram of  $G_{pv(s)}^d$

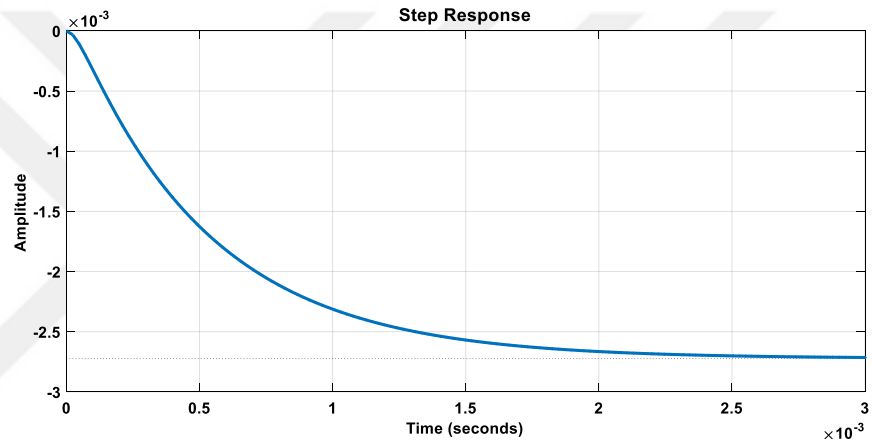


Figure 3.9 Step response of  $G_{pv(s)}^d$

### 3.6 Selecting the input capacitor of boost converter with respect to the pv panel

The input capacitor shown in Figure 3.10 plays a major role in the PV system in which selecting the appropriate input capacitor on the output terminals of the solar PV array will limit the voltage fluctuations seen on  $V_{pv}$  which is the output voltage of the PV array, thus the DC to DC boost converter successfully extracts the active power with minimum voltage fluctuations. The input capacitor  $C_{pv}$  is calculated according to the desired voltage ripple, the equivalent resistance of the PV panel  $R_{pv}$ , and the MPPT switching frequency  $f_{MPPT}=1000$  Hz as shown in equation 3.16 (Zengin et al, 2013).

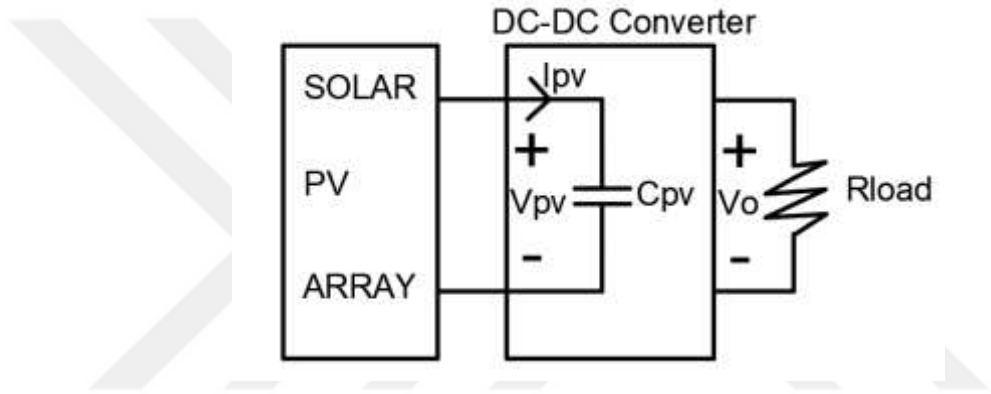


Figure 3.10 capacitance between solar panel and DC –DC boost converter terminals

$$\Delta V_o = V_{pv} * \frac{1}{(R_{pv} * C_{pv} * 2 * f_{MPPT})} \quad (3.16)$$

Taking Figure 2.1 into consideration and focusing on extracting the maximum amount of active power from the PV array, the output equivalent resistance of the PV array is equal to the equivalent resistance of the PV array operating at  $R_{MPP}$ . Input capacitance for 0.5 % voltage fluctuation  $C_{pv} = 15.0 \mu F$  in which  $R_{pv}=R_{MPP}= 21.476 \Omega$ . The mechanism of the perturb and observe has to be taken into consideration in which this strict voltage perturbation will restrict the mobility of the system during operation, thus taking into account this restrain  $C_{pv}= 3.75 \mu F$  is used for 2 % fluctuation in voltage of PV.

### 3.7 Simulation of PV array with duty controlled boost converter and resistive load

The simulations have been carried out for single PV array under the control of the DC to DC boost converter with duty based PO, and PSO algorithms implemented as mentioned in chapter 2, and 3 connected to a purely resistive load. All the simulations have been carried out in the MATLAB /SIMULINK environment in which the figures below show how implementation was carried out possible. Figures 3.11, 3.12, and 3.13 represent the simulink composition of the MPPT operated PV array connected to the boost converter. The system parameters are given in Table 3.1 .

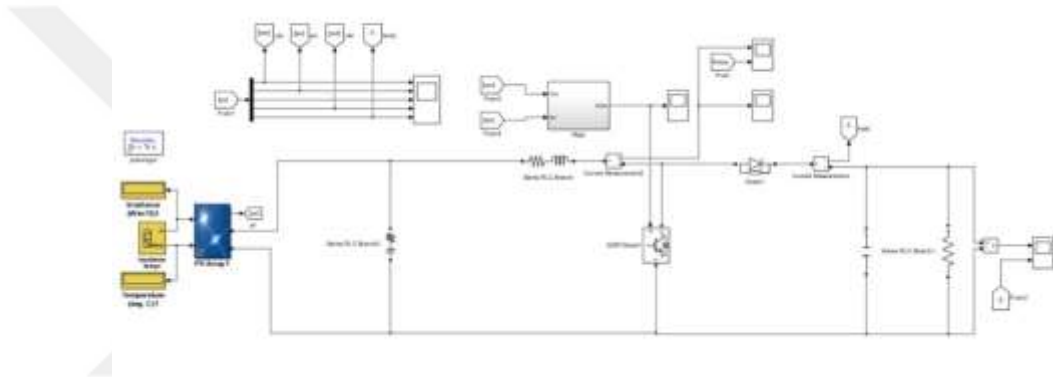


Figure 3.11 MATLAB Simulink Composition of PV array with boost converter

In Figure 3.12 the Matlab function block has two inputs which are the output voltage of the PV array  $V_{pv}$ , and the output current of the PV array  $I_{pv}$ . The output of the function block is duty reference as a result of the either P&O or PSO based algorithms according to both flowcharts in Figure 3.1, and Figure 3.4. This reference duty cycle is then fed through a comparator with trailing edge modulation at a switching frequency of boost converter as shown in Figure 3.13.

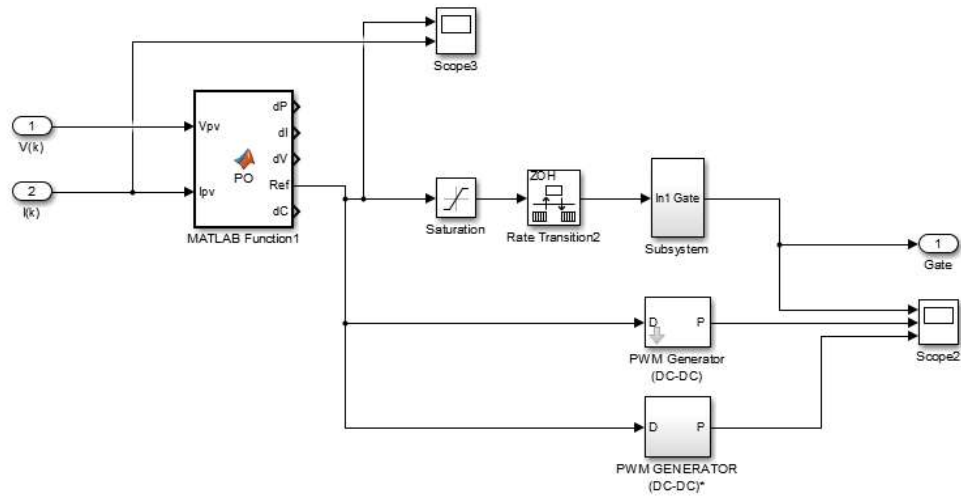


Figure 3.12 MPPT Simulink block

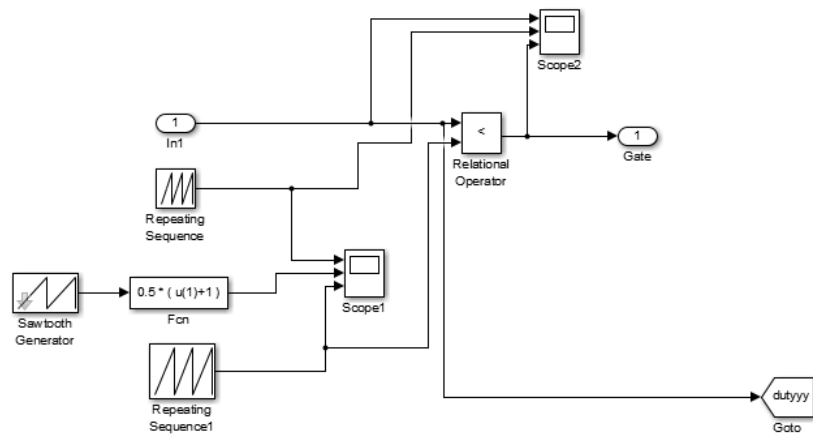


Figure 3.13 Gate signal generation of the MPPT



Table 3.1 Parameters of the PV array with duty-controlled boost converter connected to resistive load

Symbol	Parameter	Value
$f_s$	Switching frequency of Boost converter	10000 Hz
$f_{MPPT}$	Switching frequency of MPPT algorithm	1000 Hz (PO) 1000 Hz(PSO)
$C_{pv}$	input capacitance of boost converter	3.705 $\mu$ F
$C_{out}$	output capacitance of boost converter	2.77 mF
$L_b$	boost inductance	5 mH
$R$	Internal resistance of boost inductance	0.2 $\Omega$
$T_{delay}$	Delay time for boost gate signal	0.1 s

### 3.7.1 Simulation of PV array with duty based PO algorithm

In this case study the boost converter's output terminals are connected to a constant resistive load drawing 3700 Watt at 400V thus it's equivalent resistance is  $400^2/3700 = 43.24 \Omega$  which is the maximum active power the PV array can provide under constant  $1 \text{ kW/m}^2$  of irradiation and 25 degrees celcius of temperature. The outputs of the PV array in Figure 3.14 show clearly that the MPP point is met in which the voltage  $V_{pv}$  is varying between 280 and 288 volts while as the current  $I_{pv}$  is varying between 12.75 and 13.25 amperes. Both outputs of the PV array are close to the actual  $V_{mpp} = 282 \text{ volts}$ , and  $I_{mpp} = 13.14 \text{ amperes}$  which are extracted from the PV array's own I-V curve. Due to the nature of the PO algorithm there is a constant search for MPP thus explaining these variations at steady state. Figure 3.15 represents the voltage output and inductance current of the boost converter in which an approximately constant 400 volt level is obtained with the inductance current varying similar to  $I_{pv}$ . Figure 3.16 shows the active output power extracted from the PV array in which 3700 watts is being drawn that is the maximum power available after a 50 ms transient period.

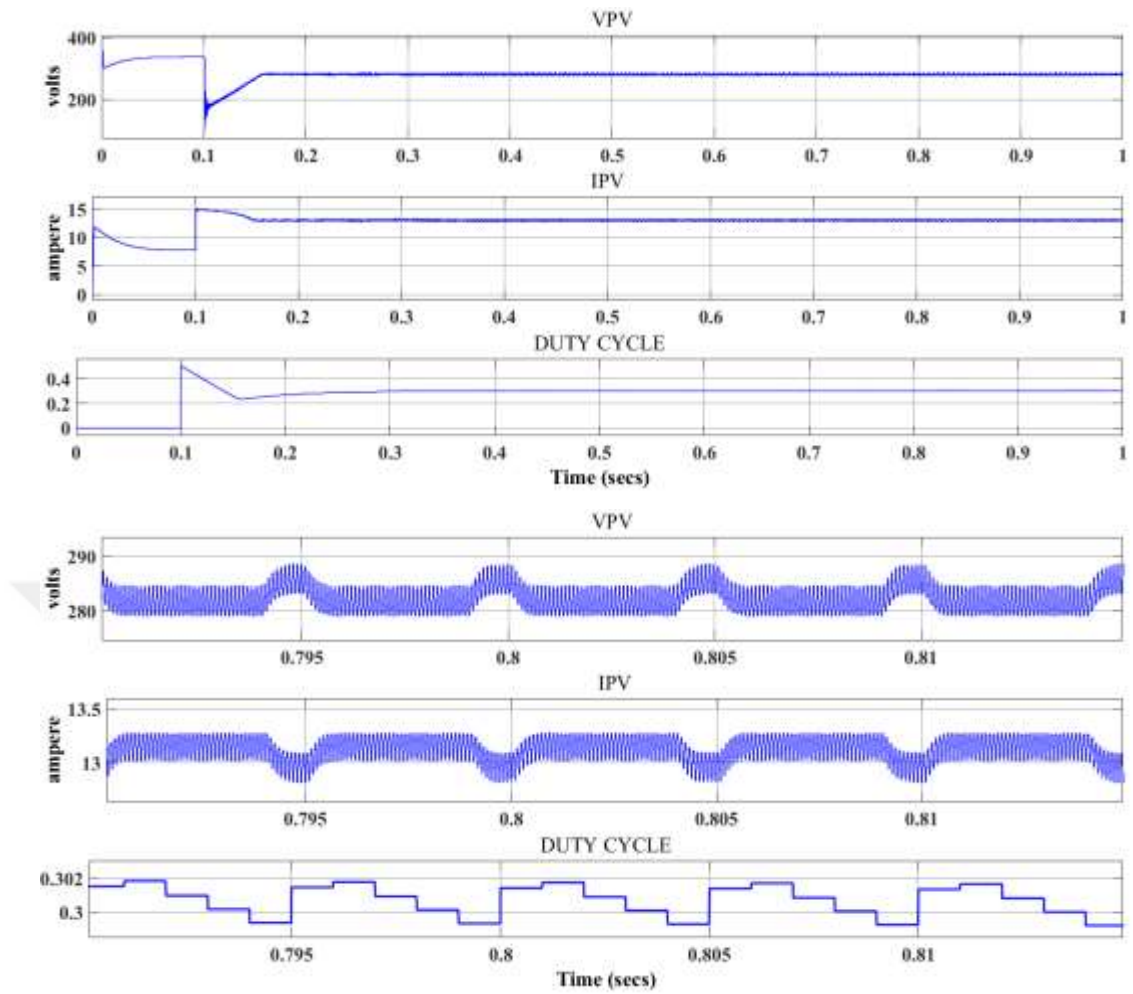


Figure 3.14 Output voltage, duty cycle, and current of the PV array under constant 1 kw/m<sup>2</sup> irradiation

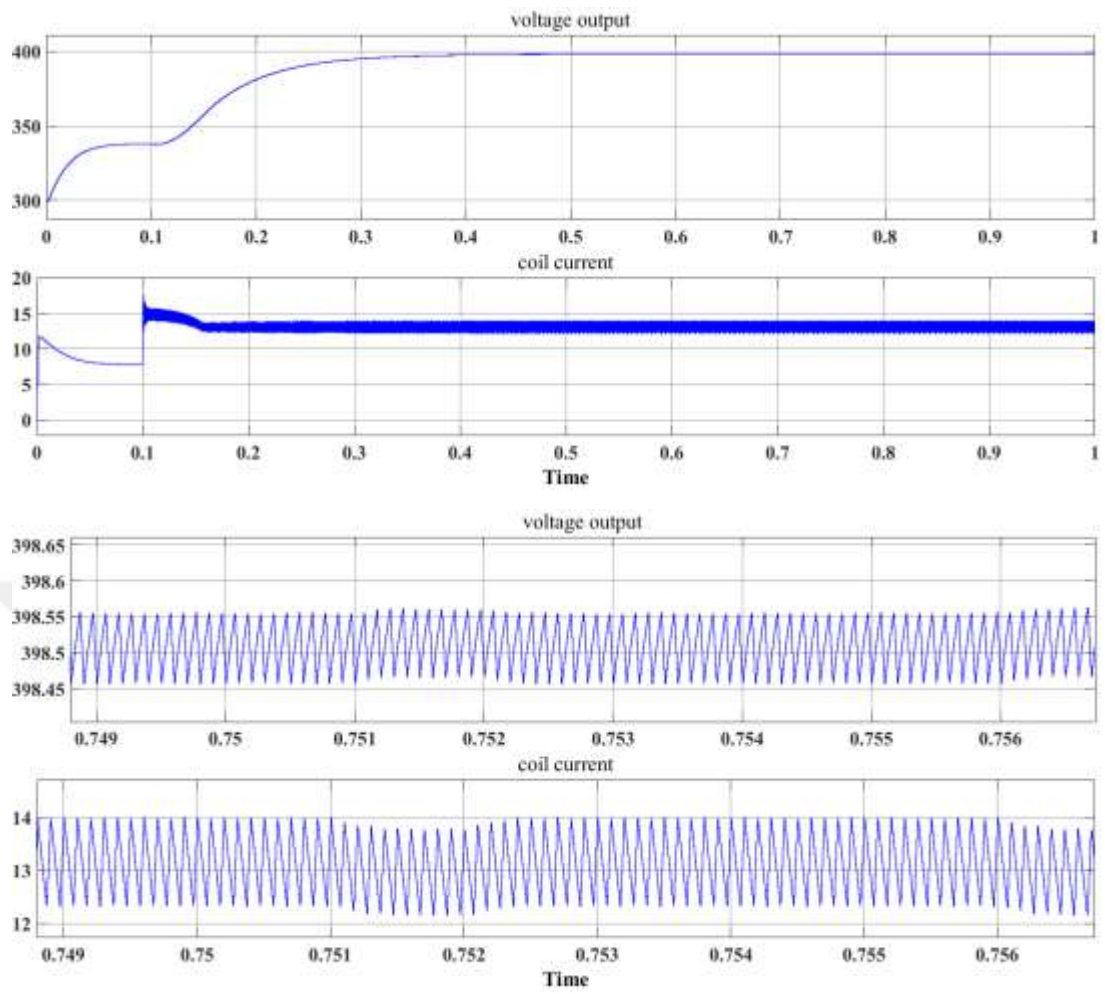


Figure 3.15 Voltage output and inductance current of the boost converter

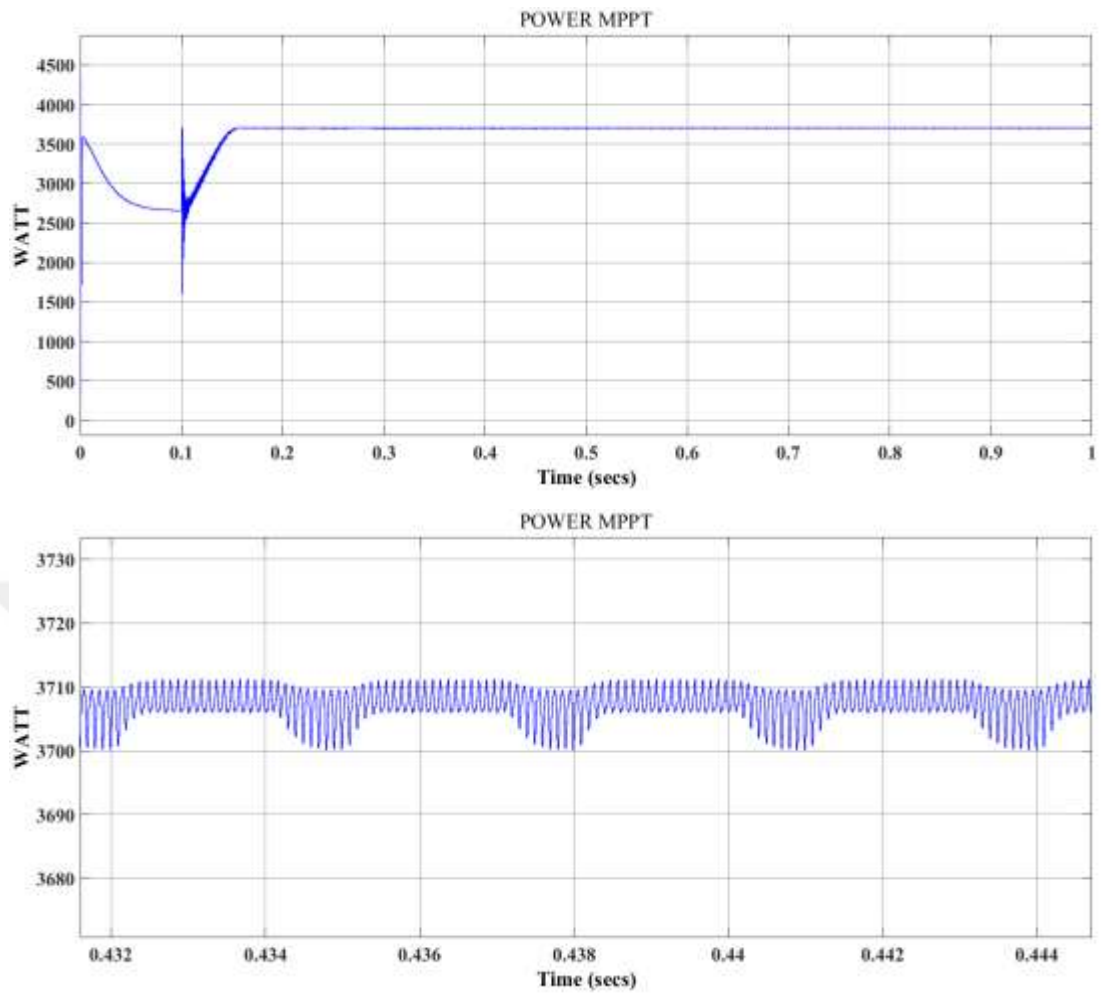


Figure 3.16 Power output of the PV array

### ***3.7.2 Simulation of PV array with duty based PSO algorithm***

In this case study the boost converter's output terminals are connected to a resistive load 3700 watt which is the maximum active power the PV array can provide under constant  $1 \text{ kw/m}^2$  of irradiation and 25 degrees celcius of temperature. The outputs of the PV array in figure 3.17 show clearly that the MPP point is met in which the voltage  $V_{pv}$  is varying between 284 and 288 volts while as the current  $I_{pv}$  is varying between 12.75 and 13.1 amperes. Both outputs of the PV array are close to the actual  $V_{mpp}=282$  volts , and  $I_{mpp}= 13.14$  amperes which are extracted from the PV array's own I-V curve. Figure 3.18 represents the voltage output and inductance current of the boost converter in which an approximately constant 400 volt level is obtained with the inductance current varying similar to  $I_{pv}$ . Figure 3.19 shows the active output power extracted from the PV array in which 3700 watts is being drawn at steady state. Figure 3.20 shows the three particles of the PSO algorithm in which steady state is met after 10 ms of transient period.

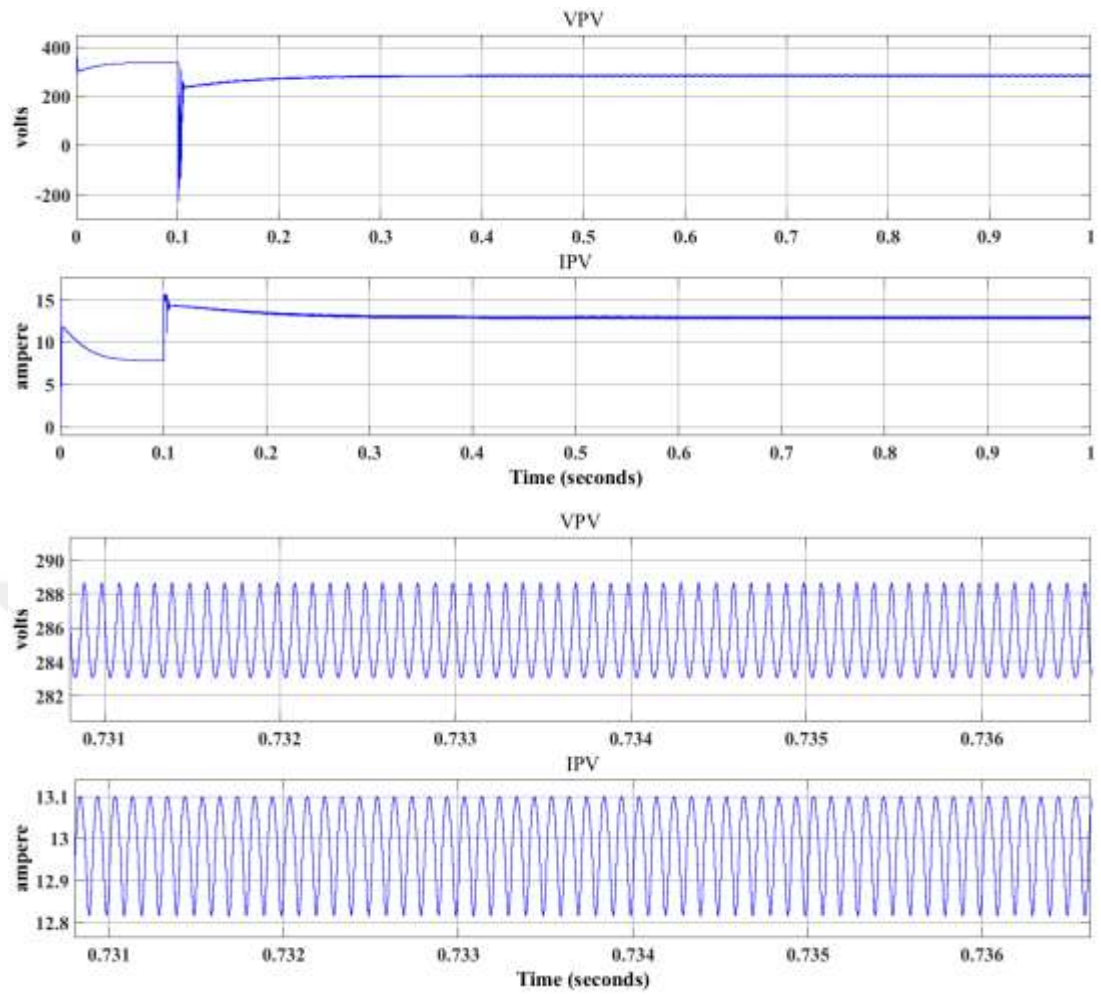


Figure 3.17 Voltage and current outputs of the PV array

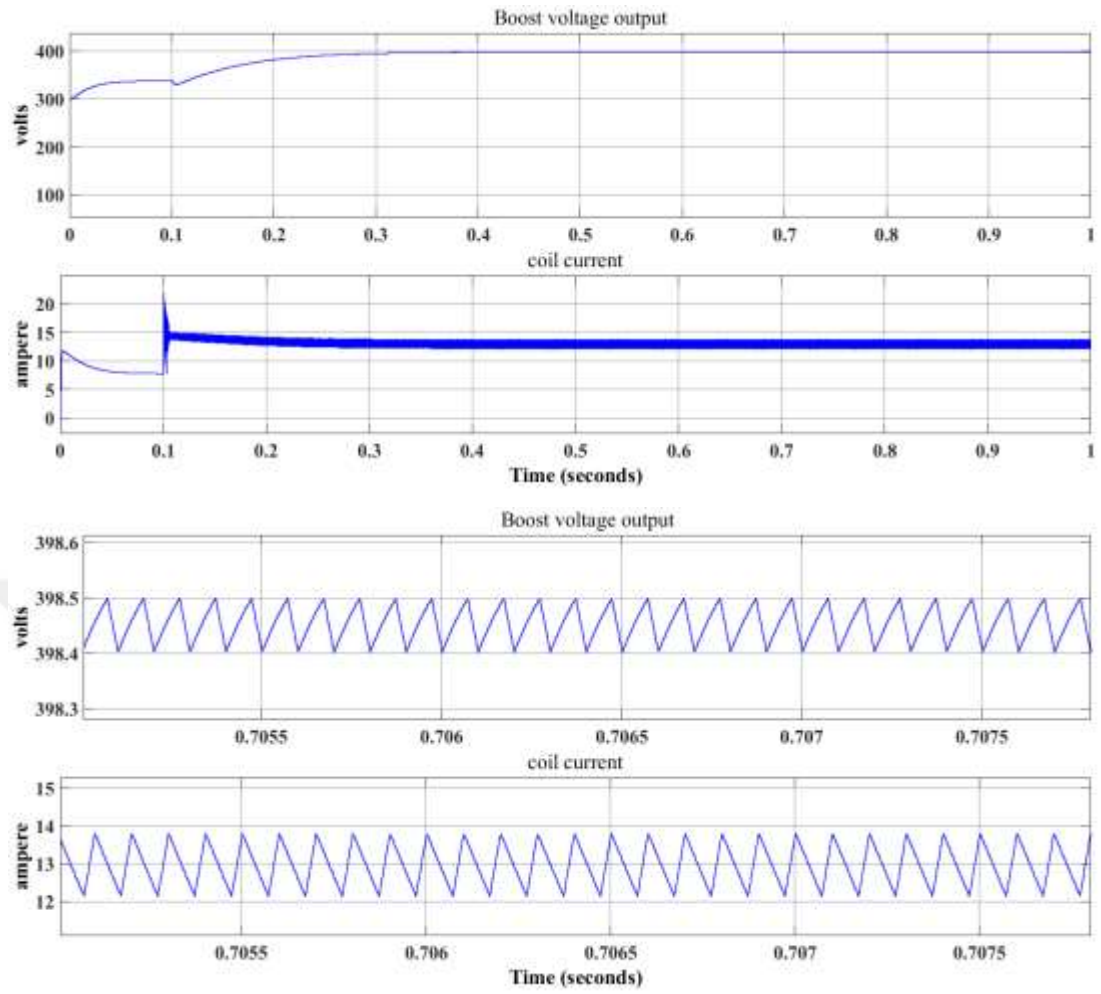


Figure 3.18 Output voltage and inductance current of boost converter

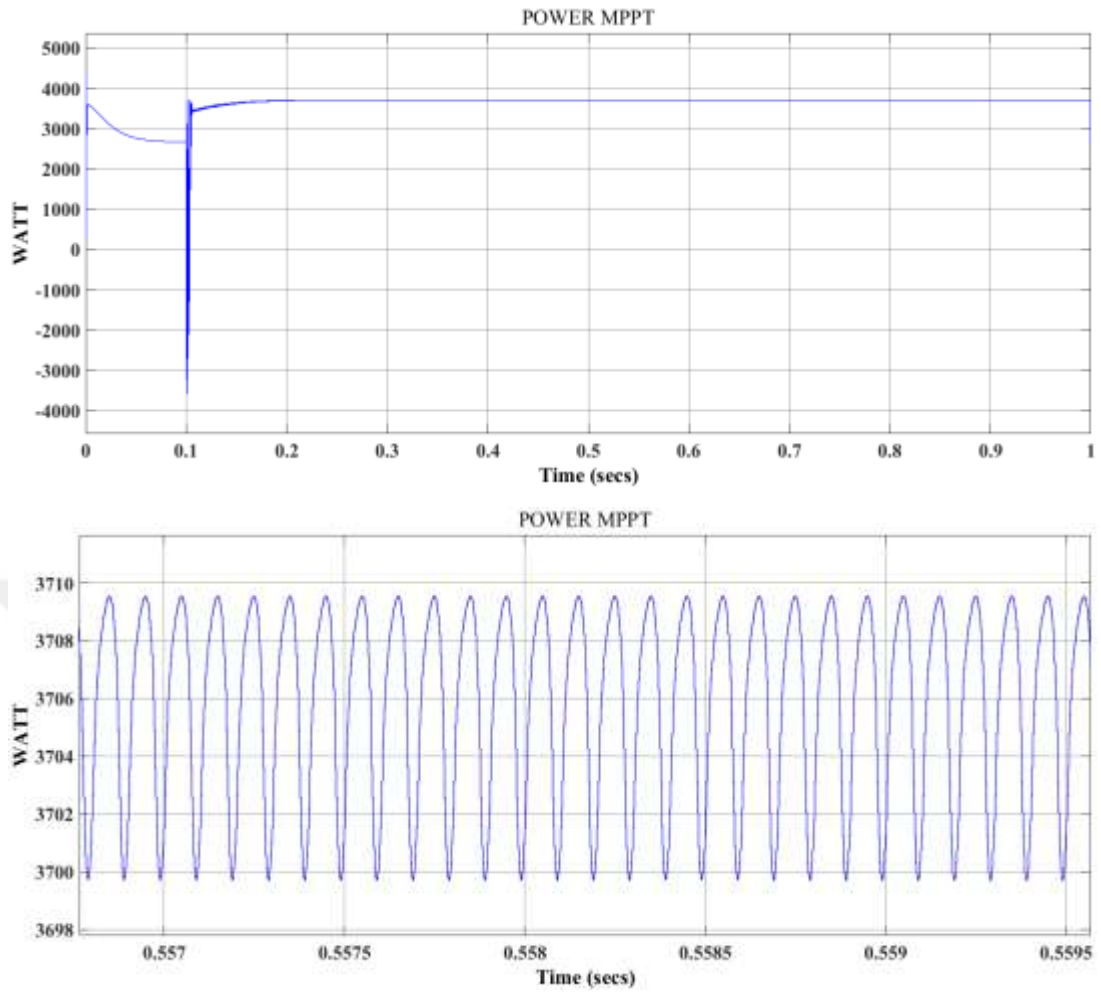


Figure 3.19 Active output power of the PV array

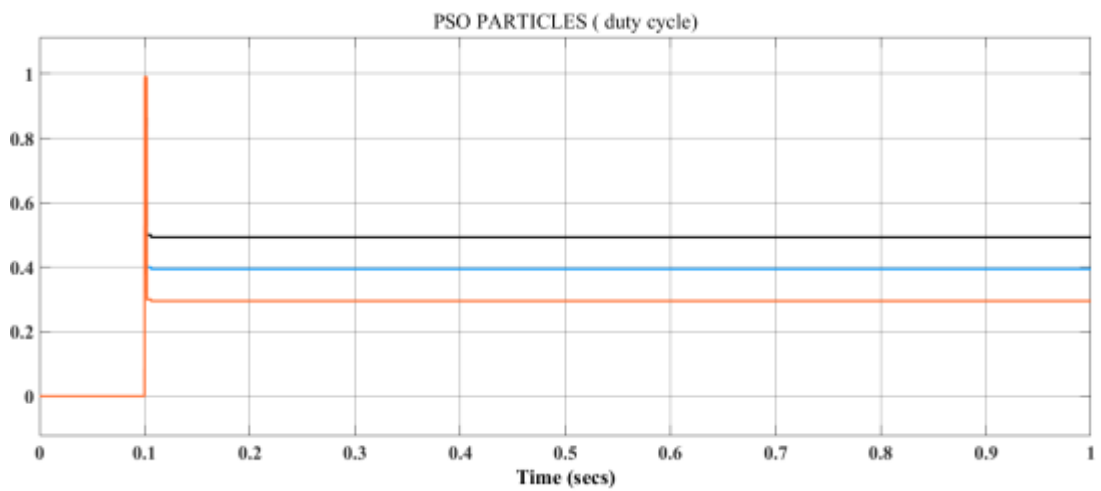


Figure 3.20 Particles of the PSO with their duty cycles



### 3.8 Simulation of PV array with predictive current controlled boost converter and resistive load

The simulations have been carried out for single PV array under the control of the DC to DC boost converter with duty based PO, and PSO algorithms implemented upon the predictive current control as mentioned in Section 2.3. All the simulations have been carried out in the MATLAB /SIMULINK enviroment in which the figures below show how implementation was carried out possible. Figures 3.21, and 3.22 represent the Simulink composition of the MPPT operated PV array connected to the boost converter with PI controller that controls the reference voltage output of the MPPT with  $V_{pv}^*$  in which system parameters are given in Table 3.2.

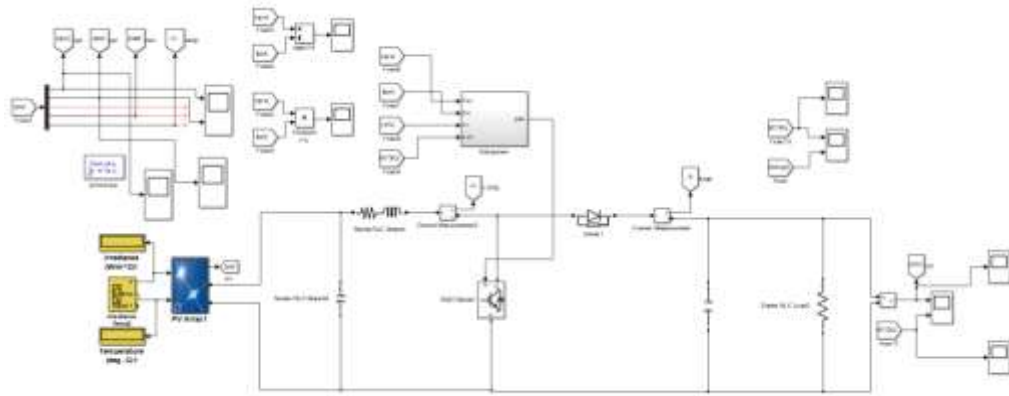


Figure 3.21 MATLAB Simulink Composition of PV array with Boost converter

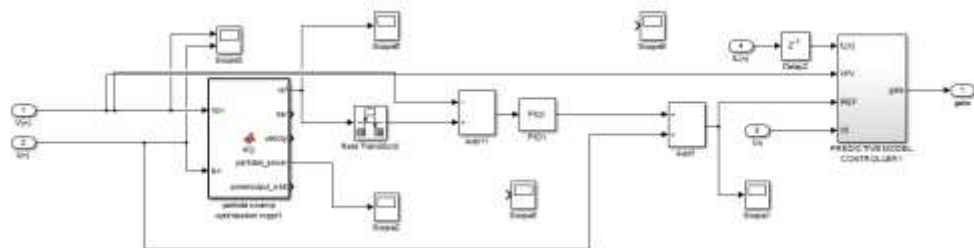


Figure 3.22 Implementation of the voltage oriented MPPT algorithm

Table 3.2 Parameters of the PV array with predictive current-controlled boost converter connected to resistive load

Symbol	Parameter	Value
$f_{s2}$	Switching frequency of Boost converter	10000 Hz
$f_{MPPT}$	Switching frequency of voltage oriented MPPT algorithm	1000 Hz (PO) 1000 Hz(PSO)
$C_{pv}$	input capacitance of boost converter	3.705 $\mu$ F
$C_{out}$	output capacitance of boost converter	2.77 mF
$L_b$	boost inductance	5 mH
$r$	Internal resistance of boost inductance	0.2 $\Omega$
$T_{delay}$	Delay time for boost gate signal	0.02 s

### 3.8.1 MPPT Based Predictive Valley Current Control

The following two step horizon valley predictive current control equation 3.17 is implemented using Simulink Block models in which the input  $I_{ref}$  of the predictive control is taken from the voltage oriented MPPT algorithm. This voltage reference is subtracted from the output voltage of the PV array  $V_{pv}$  fed to the PI controller. The output of the PI controller with the summation of the output current of the PV array  $I_{pv}$  creates  $I_{ref}$  for the predictive valley current control system to follow. In addition PSO MPPT algorithm can be applied with the same concept in which using the output of the PSO with a voltage oriented MPPT algorithm,  $I_{ref}$  can be obtained with the addition of the output current of the PV array  $I_{pv}$ . Its implementation can be seen in Figure 3.23.

$$d[n + 1] = 2 - d[n] - \frac{L \cdot (i_L[n-1] - i_{ref})}{V_o \cdot T_s} - \frac{2 \cdot V_{pv}}{V_o} \quad (3.17)$$

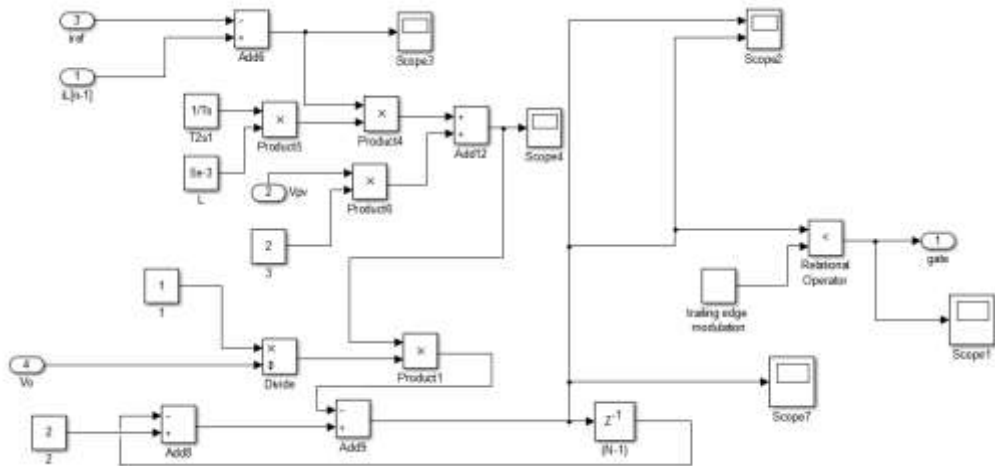


Figure 3.23 Predictive model valley control

### 3.8.1.1 Voltage oriented PO based predictive valley current control of PV array

In this case study the boost converter's output terminals are connected to a resistive load 3700 watt which is the maximum active power the PV array can provide under constant  $1 \text{ kw/m}^2$  of irradiation and 25 degrees celcius of temperature. The outputs of the PV array in figure 3.24 show clearly that the MPP point is met in which the voltage  $V_{pv}$  is varying between 260 and 300 volts while as the current  $I_{pv}$  is varying between 12 and 14 amperes. Both outputs of the PV array are close to the actual  $V_{mpp}=282$  volts , and  $I_{mpp}= 13.14$  amperes which are extracted from the PV array's own I-V curve . Figure 3.25 represents the voltage output and inductance current of the boost converter in which a constant 400 volt level is obtained with the inductance current varying similar to  $I_{pv}$ . Figure 3.26 shows the active output power extracted from the PV array in which 3700 watts is being drawn after a 0.1 second transient period. Figure 3.28 shows the output equivalent resistance of the PV array which can be obtained from  $V_{PV}/I_{PV}$  ratio in which  $R_{mpp}= V_{mpp}/I_{mpp}=21.476$  ohms on average thus proving the system was able to reach MPP conditions. Figure 3.28 represents the output reference voltage of the voltage oriented MPPT algorithm in which  $V_{ref}$  is identical to  $V_{mpp}=282$  volts. The PI controller's constants are as follows  $K_p=0.1$  , and  $K_i=5$ .

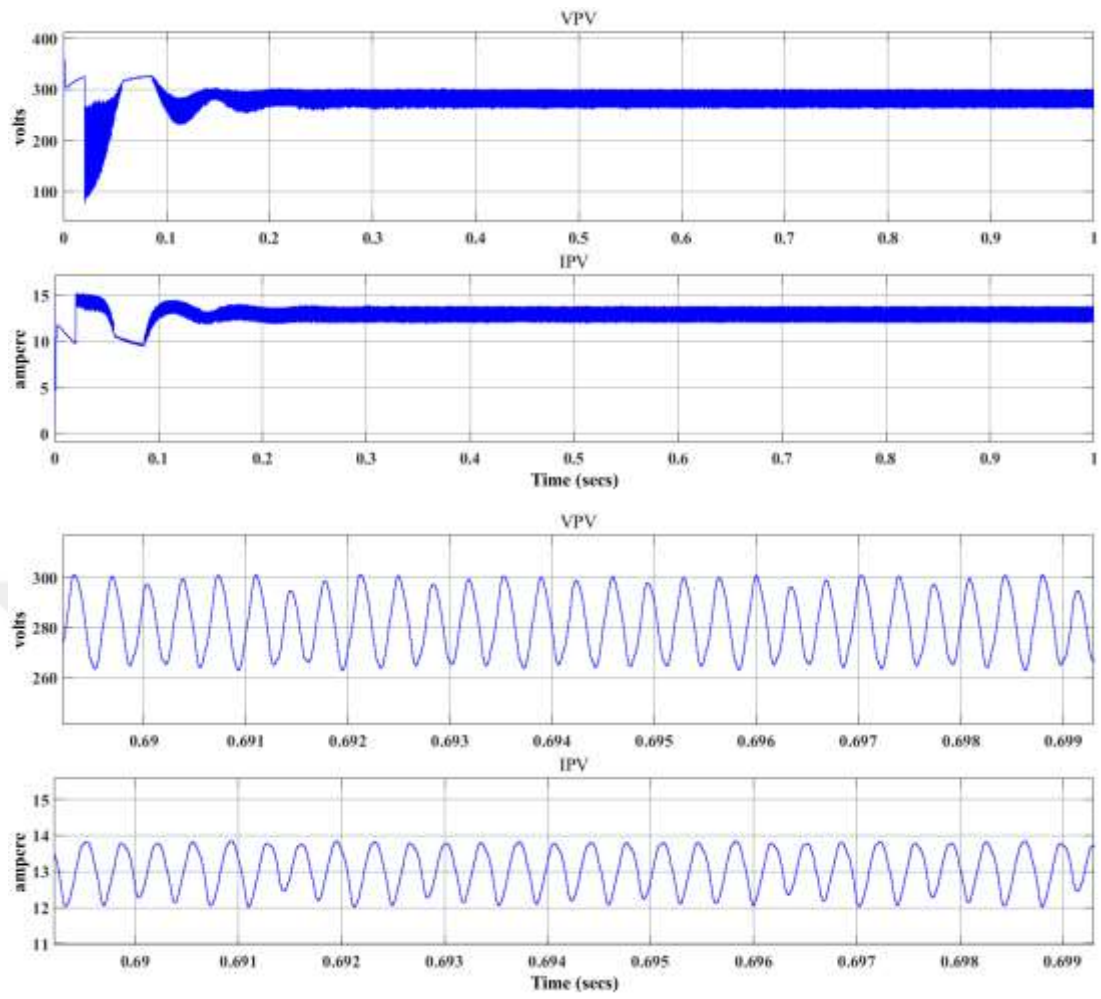


Figure 3.24 Voltage and current output of the PV array

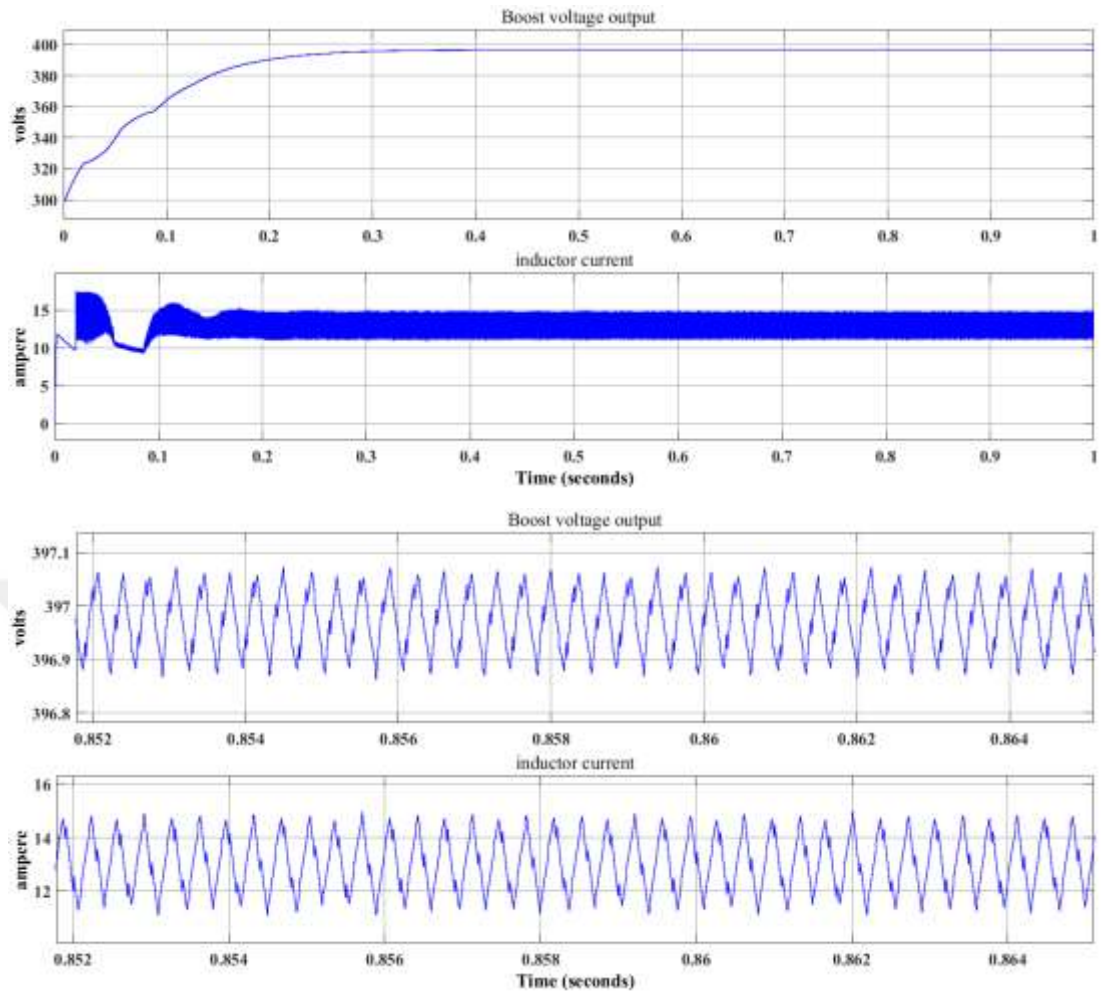


Figure 3.25 Output voltage and inductance current of boost converter

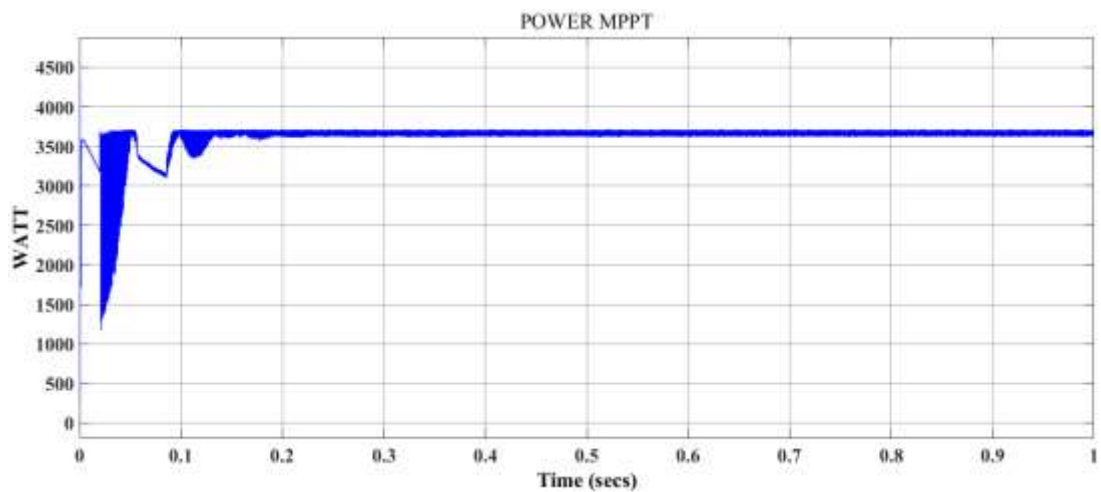


Figure 3.26 Active power output of the PV array

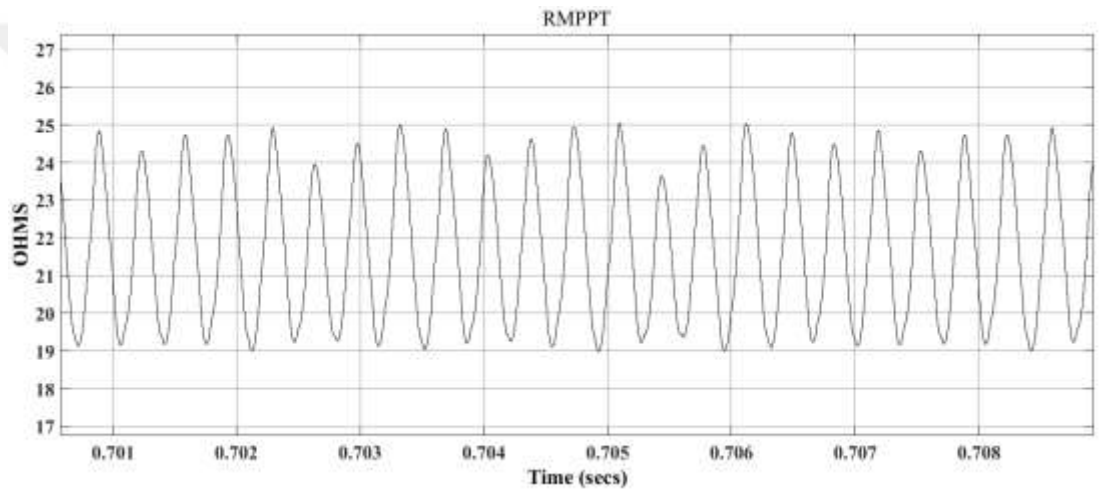
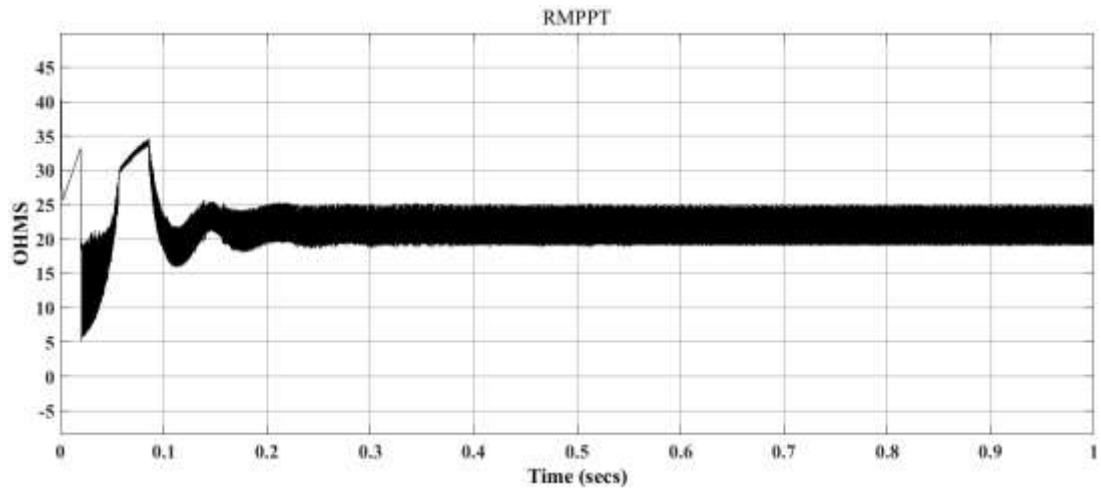


Figure 3.27 Equivalent resistance of the PV array

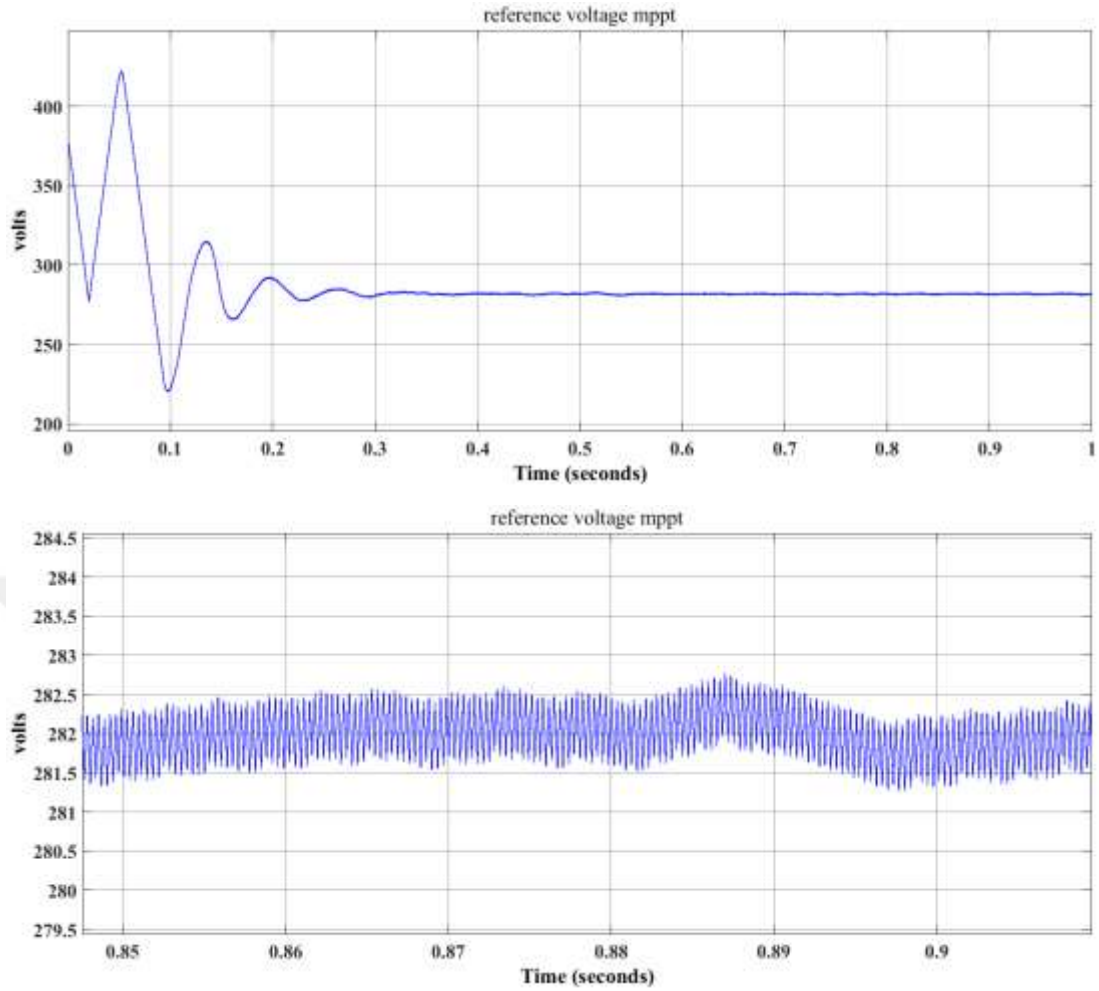


Figure 3.28 Reference output voltage of the PO MPPT algorithm

### 3.8.1.2 Voltage oriented PSO based predictive valley current control of PV array:

In this case study the boost converter's output terminals are connected to a resistive load 3700 watt which is the maximum active power the PV array can provide under constant  $1 \text{ kW/m}^2$  of irradiation and 25 degrees celcius of temperature. The outputs of the PV array in Figure 3.29 show clearly that the MPP point is approximately met in which the voltage  $V_{pv}$  is varying between 260 and 300 volts while as the current  $I_{pv}$  is varying between 12 and 14.0 amperes. Both outputs of the PV array are close to the actual  $V_{mpp}=282$  volts , and  $I_{mpp}= 13.14$  amperes which are extracted from the PV array's own I-V curve. Figure 3.30 represents the voltage output and inductance current of the boost converter in which a constant 400 volt level is obtained with the inductance current varying similar to  $I_{pv}$ . Figure 3.31 shows the active output power extracted from the PV array in which 3700 watts is being drawn after a 0.1 second

transient period. Figure 3.32 shows the three particles of the PSO algorithm in which steady state is met after 0.05 ms of transient period. The PI controller's constants are as follows  $K_p = 0.1$ , and  $K_i = 5$ .

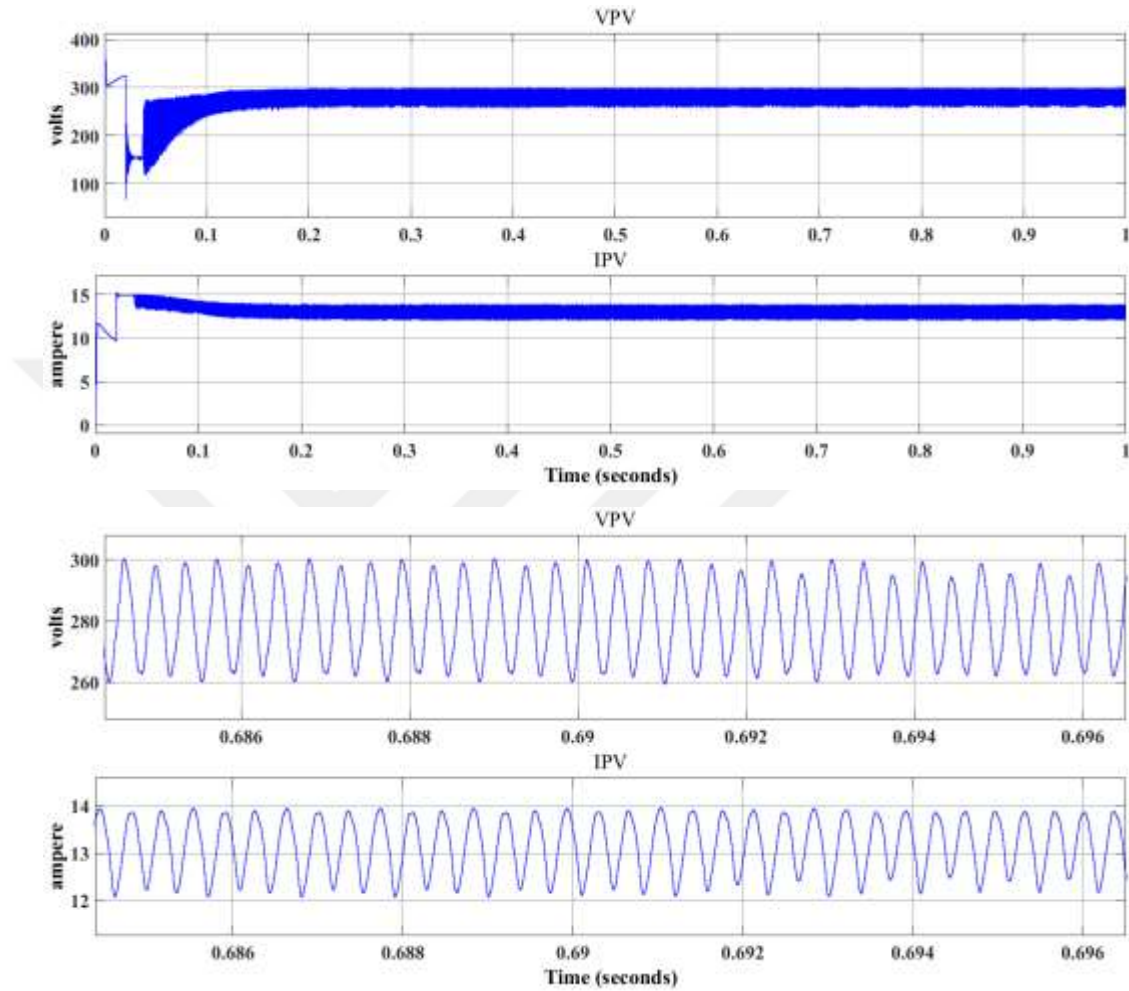


Figure 3.29 Voltage and current output of the PV array



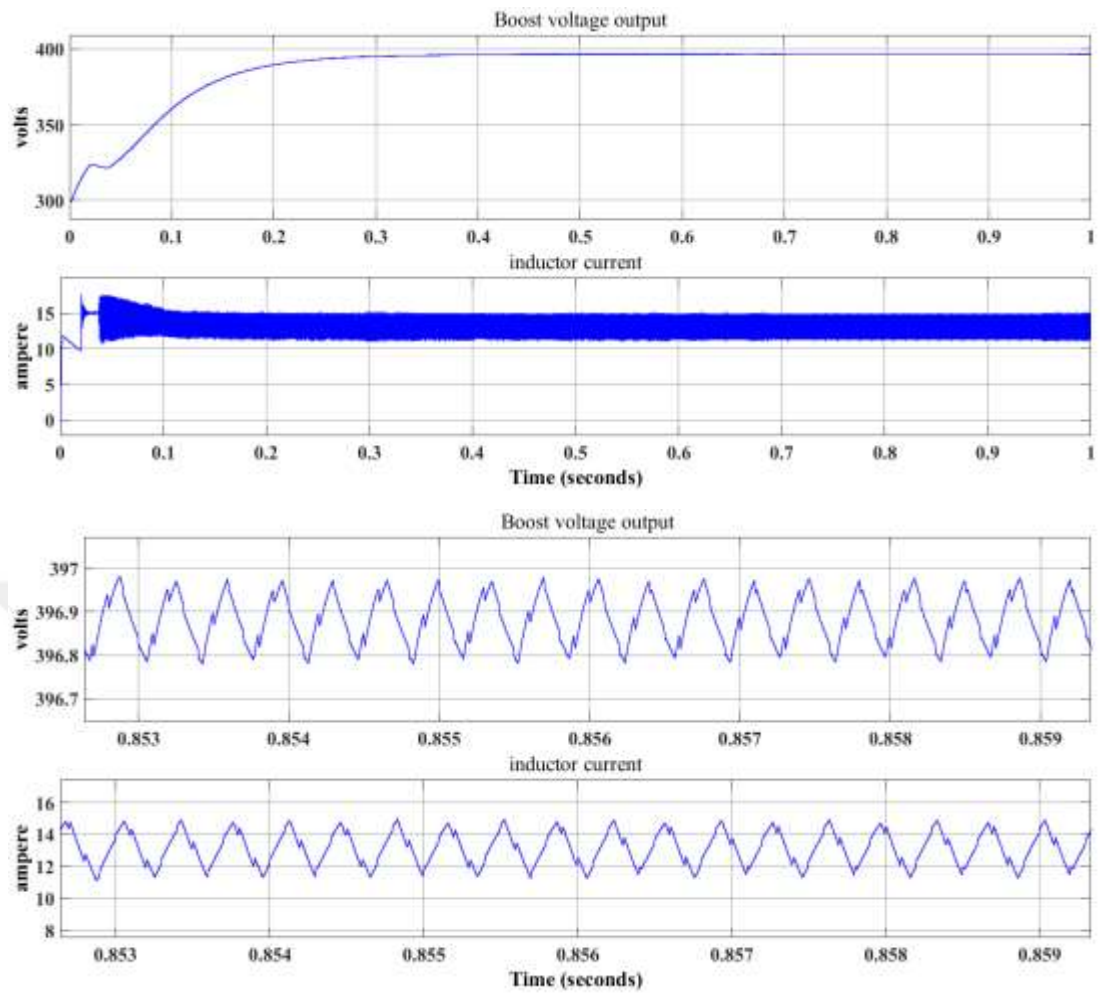


Figure 3.30 Voltage output and inductance current of the boost converter

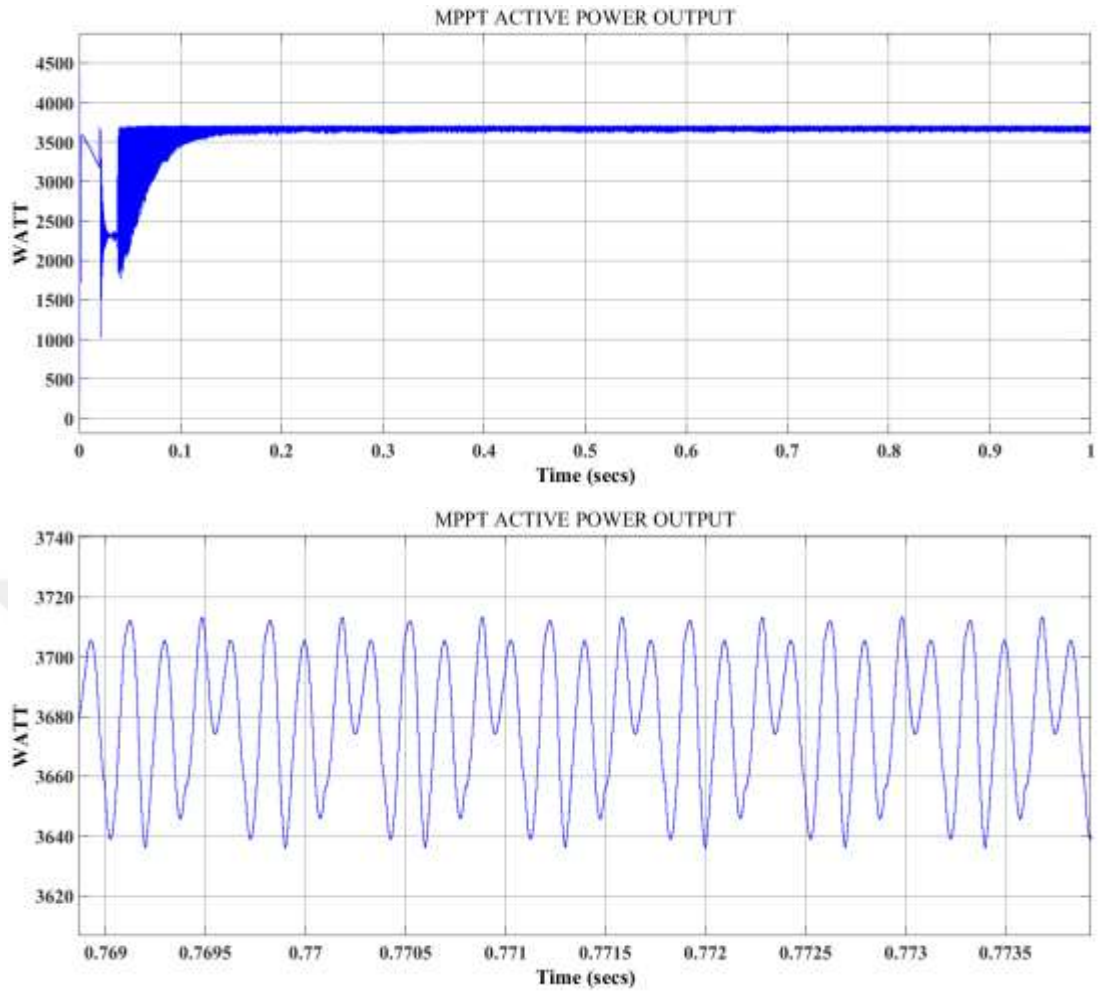


Figure 3.31 Active output power of the PV array

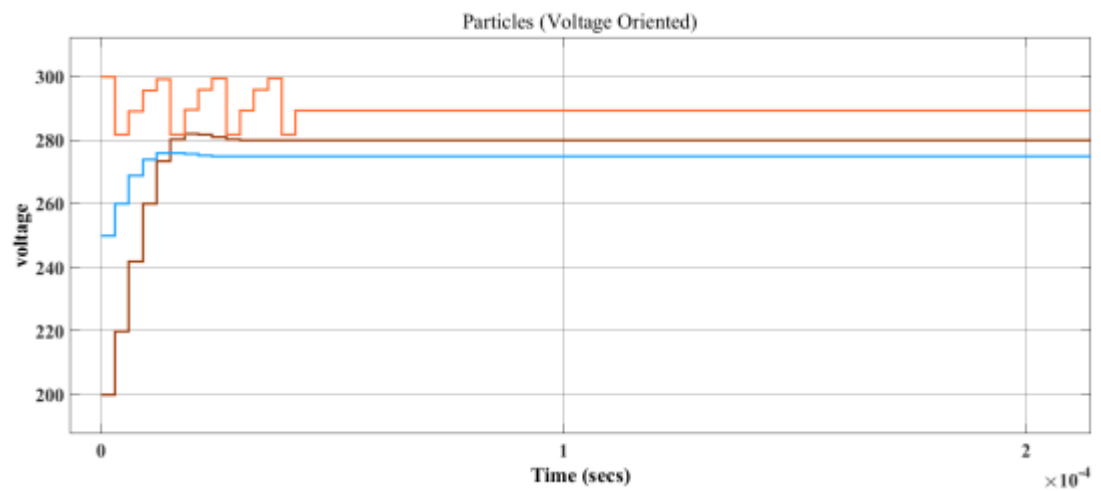


Figure 3.32 Particles of the PSO with their voltage values

### 3.8.2 MPPT Based Predictive Average Current Control

The predictive average current control methodology is identical to that of the valley current control based predictive control with one difference solely in the equation and its implementation according to equation 3.18 is shown in Figure 3.33 .

$$d[n + 1] = 1 - \left( \frac{v_{pv}}{2v_o} \right) * \left( 3 - \frac{v_{pv}}{v_o} \right) + \frac{L*(i_{ref}-i[n])}{v_o*T_s} \quad (3.18)$$

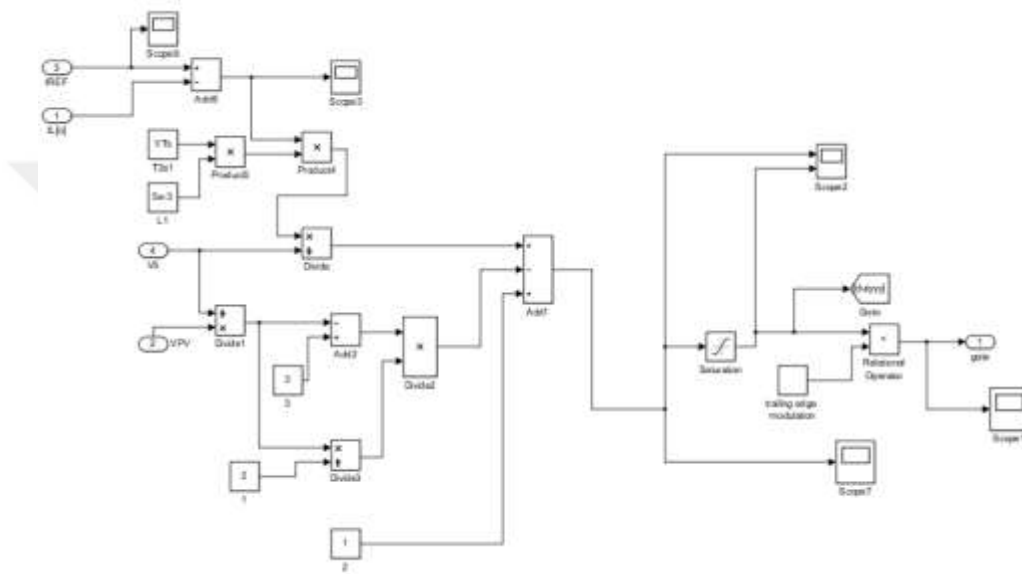


Figure 3.33 Model of the predictive average current control

#### 3.8.2.1 Voltage oriented PO based predictive average current control of PV array

In this case study the boost converter's output terminals are connected to a resistive load 3700 watt which is the maximum active power the PV array can provide under constant 1 kW/m<sup>2</sup> of irradiation and 25 degrees celcius of temperature. The outputs of the PV array in Figure 3.34 show clearly that the MPP point is met in which the voltage  $V_{pv}$  is varying between 250 and 310 volts while as the current  $I_{pv}$  is varying between 11 and 14 amperes. Both outputs of the PV array are close to the actual  $V_{mpp}$  = 282 volts , and  $I_{mpp}$  = 13.14 amperes which are extracted from the PV array's own I-V curve . Figure 3.35 represents the voltage output and inductance current of the boost converter in which an approximately constant 400 volt level is obtained with the inductance current varying similar to  $I_{pv}$ . Figure 3.36 shows the active output power extracted

from the PV array in which 3700 watts is being drawn after a 0.08 second transient period. Figure 3.37 shows the output equivalent resistance of the PV array which can be obtained from  $V_{PV}/I_{PV}$  ratio in which  $R_{mpp} = V_{mpp}/I_{mpp} = 21.5$  ohms thus proving the system was able to reach MPP conditions. Figure 3.38 represents the output reference voltage of the voltage oriented MPPT algorithm in which  $V_{ref}$  is identical to  $V_{mpp} = 282$  volts. The PI controller's constants are as follows  $K_p = 0.1$  , and  $K_i = 5$ .

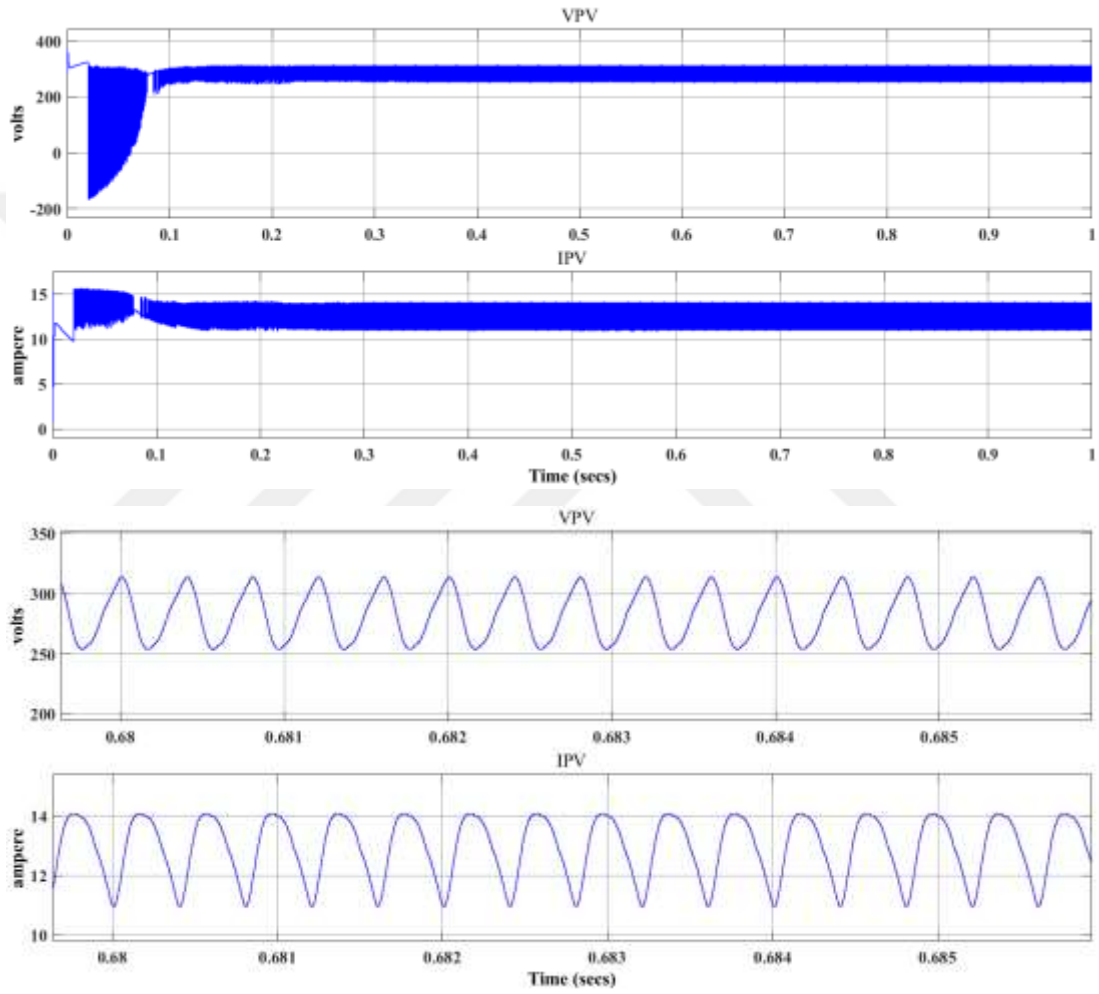


Figure 3.34 Voltage and current output of the PV array

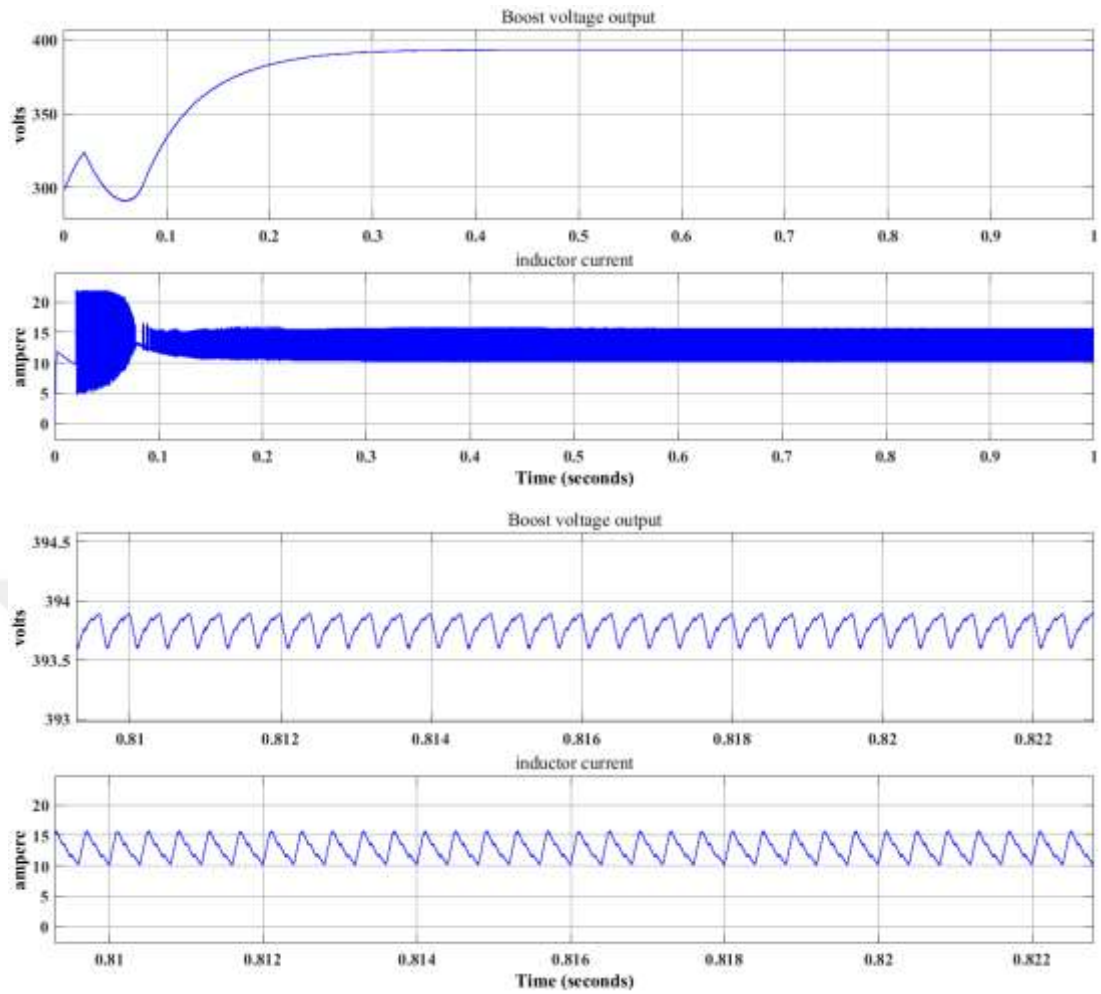


Figure 3.35 Output voltage and inductance current of boost converter

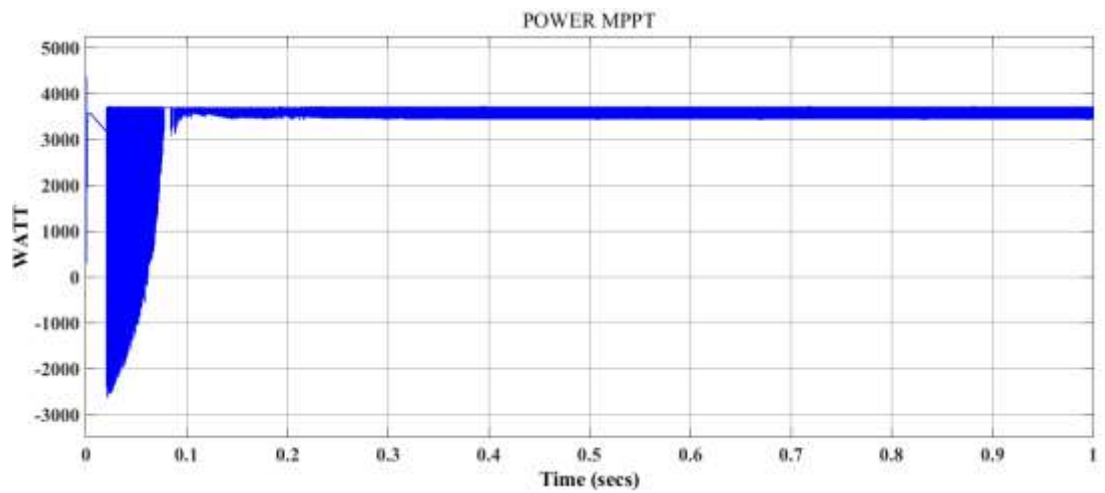


Figure 3.36 Active output power of the PV array

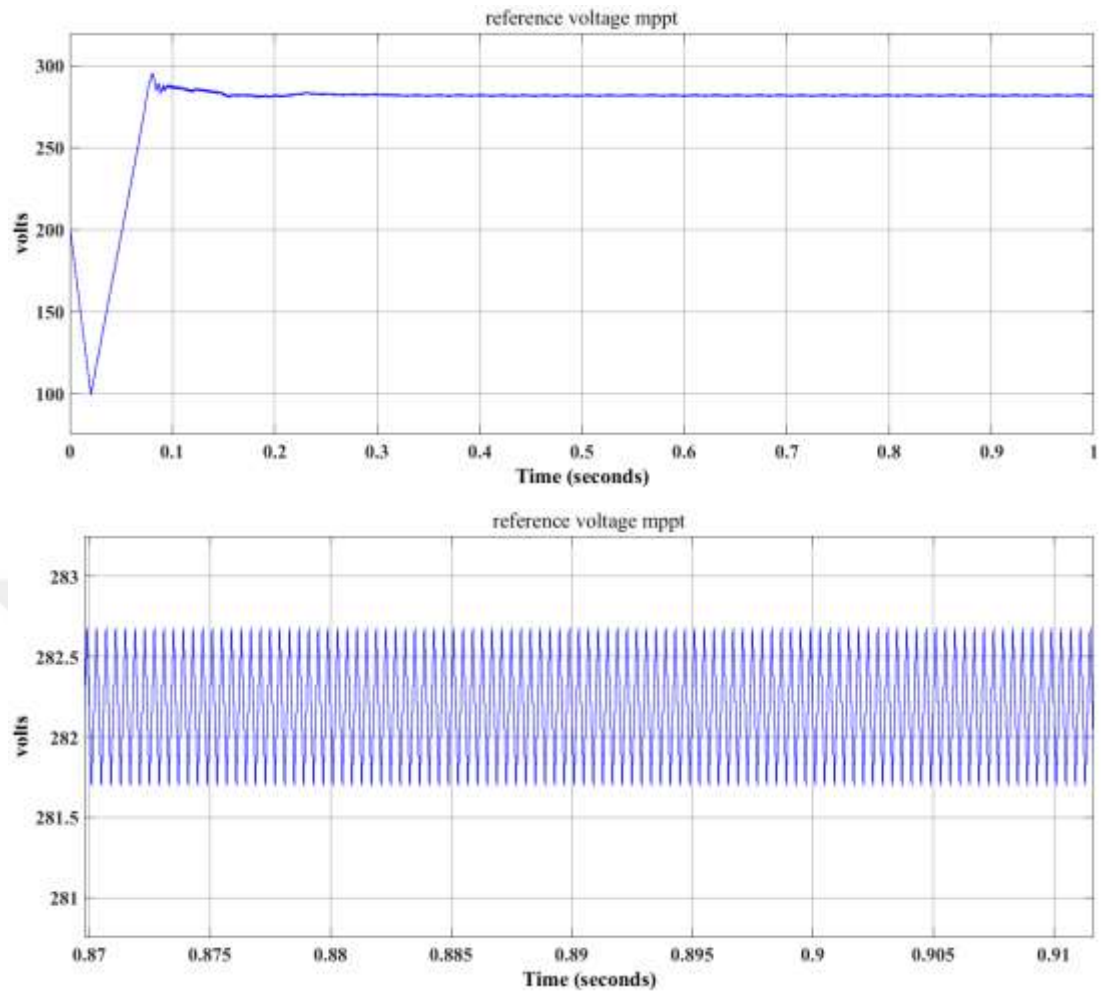


Figure 3.37 Output reference voltage of the voltage oriented PO MPPT algorithm

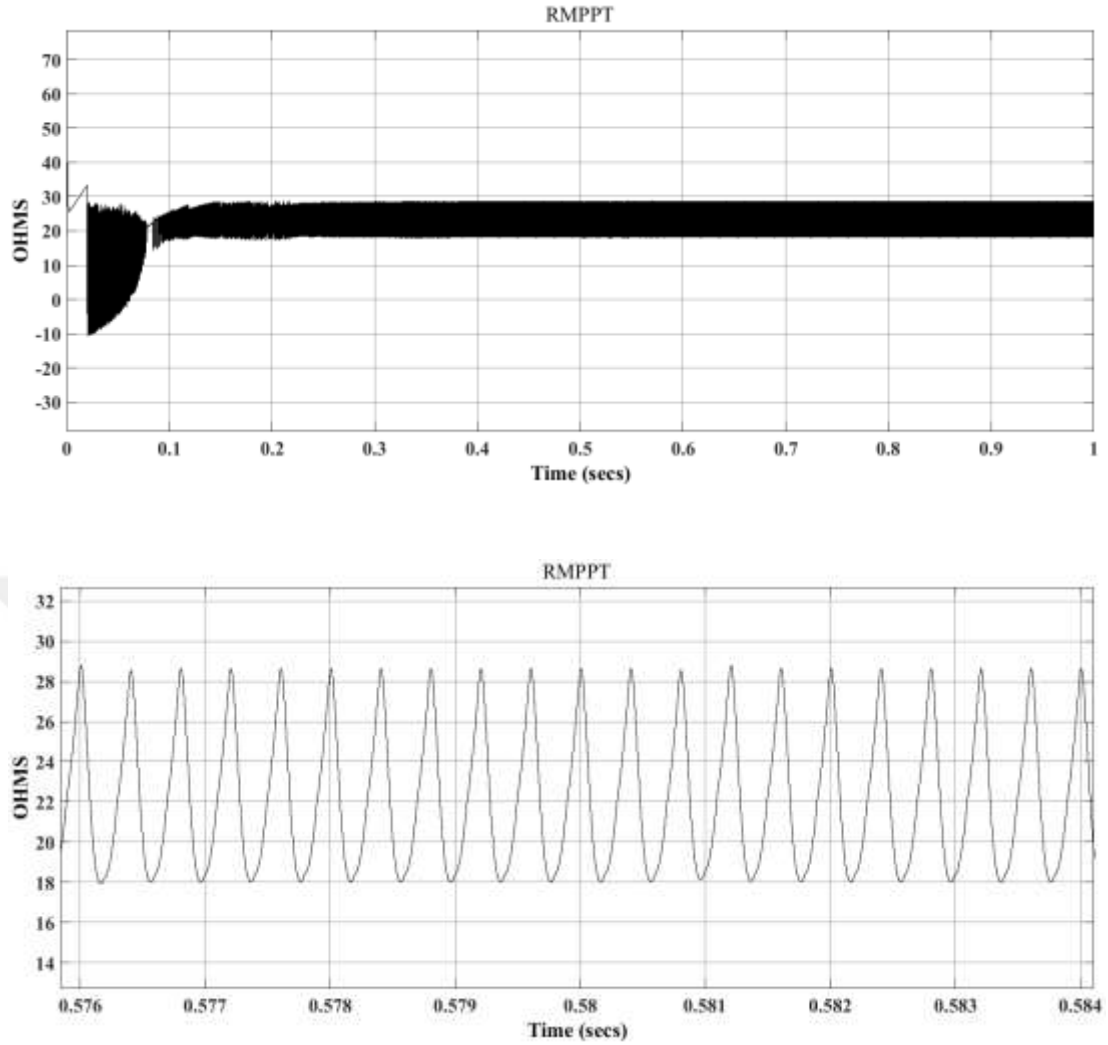


Figure 3.38 Equivalent output resistance of the PV array

### 3.8.2.2 Voltage oriented PSO based predictive average current control of PV array

In this case study the boost converter's output terminals are connected to a resistive load 3700 watt which is the maximum active power the PV array can provide under constant  $1 \text{ kW/m}^2$  of irradiation and 25 degrees celcius of temperature. The outputs of the PV array in Figure 3.39 show clearly that the MPP point is approximately met in which the voltage  $V_{pv}$  is varying between 250 and 310 volts while as the current  $I_{pv}$  is varying between 11 and 14 amperes. Both outputs of the PV array are close to the actual  $V_{mpp} = 282 \text{ volts}$  , and  $I_{mpp} = 13.2 \text{ amperes}$  which are extracted from the PV array's own I-V curve. Figure 3.40 represents the voltage output and inductance current of the boost converter in which an approximately constant 400 volt level is obtained with the inductance current varying similar to  $I_{pv}$ . Figure 3.41 shows the

active output power extracted from the PV array in which 3700 watts is being drawn after a 0.03 second transient period. Figure 3.42 shows the three particles of the PSO algorithm in which steady state is met after 0.05 ms of transient period. The PI controller's constants are as follows  $K_p=0.1$  , and  $K_i=5$ .

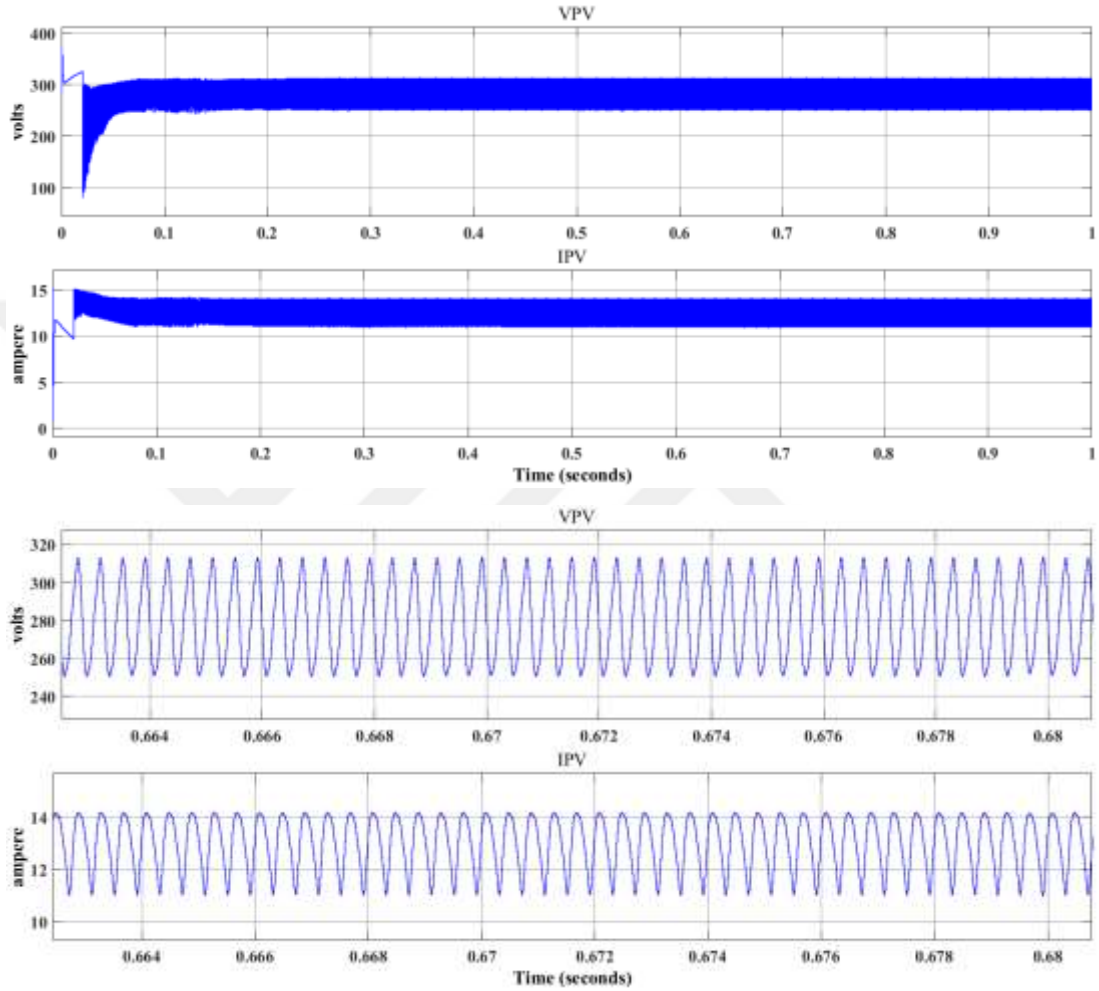


Figure 3.39 Voltage and current output of the PV array



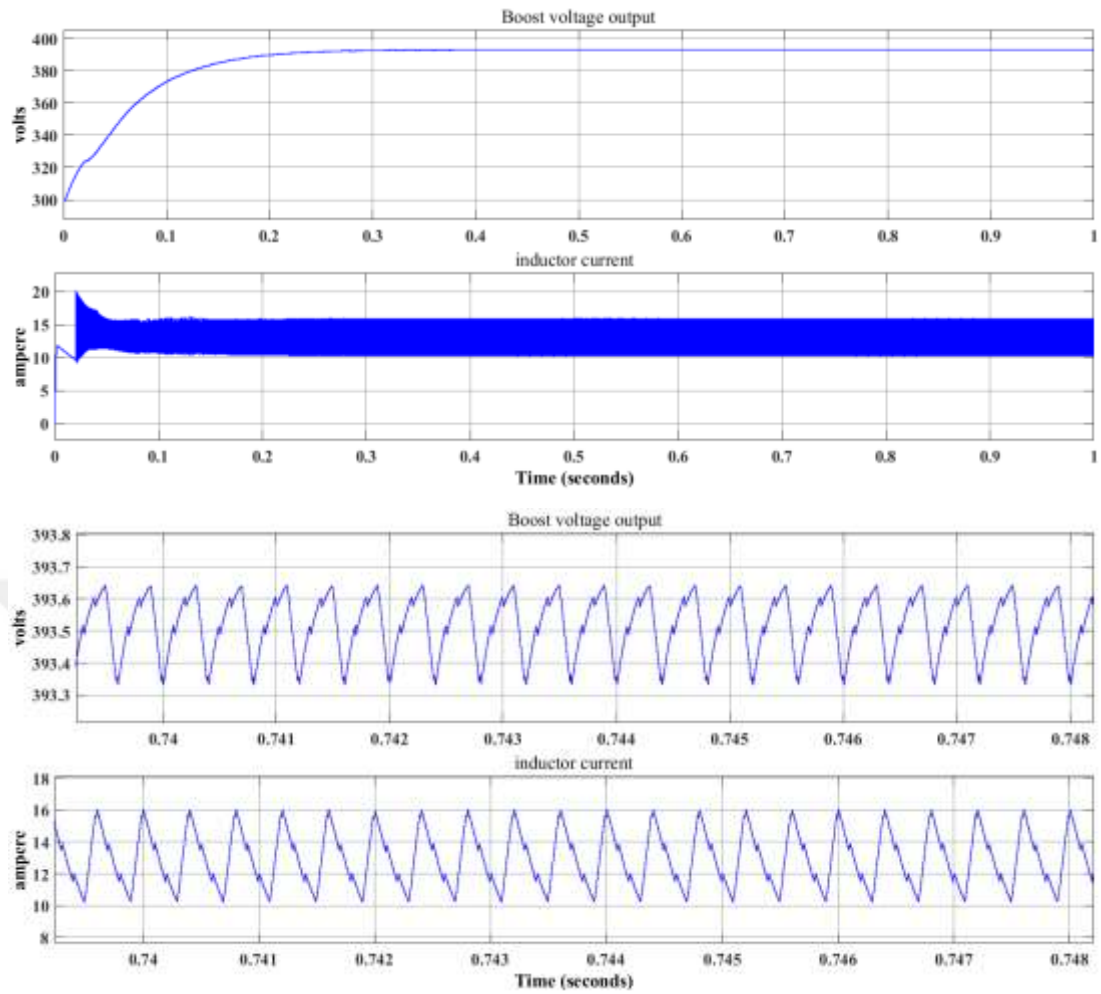


Figure 3.40 Output voltage and inductance current of the boost converter

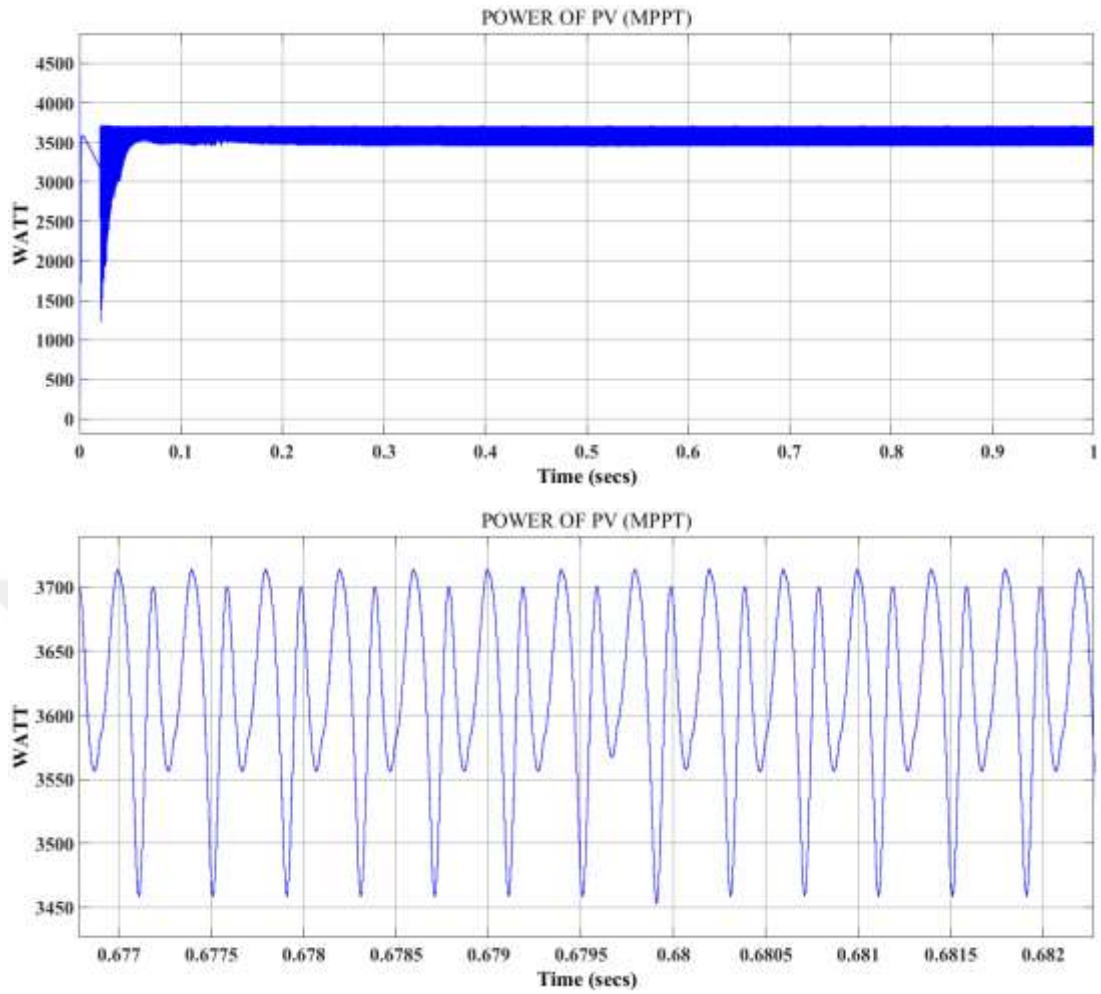


Figure 3.41 Active power output of the PV array

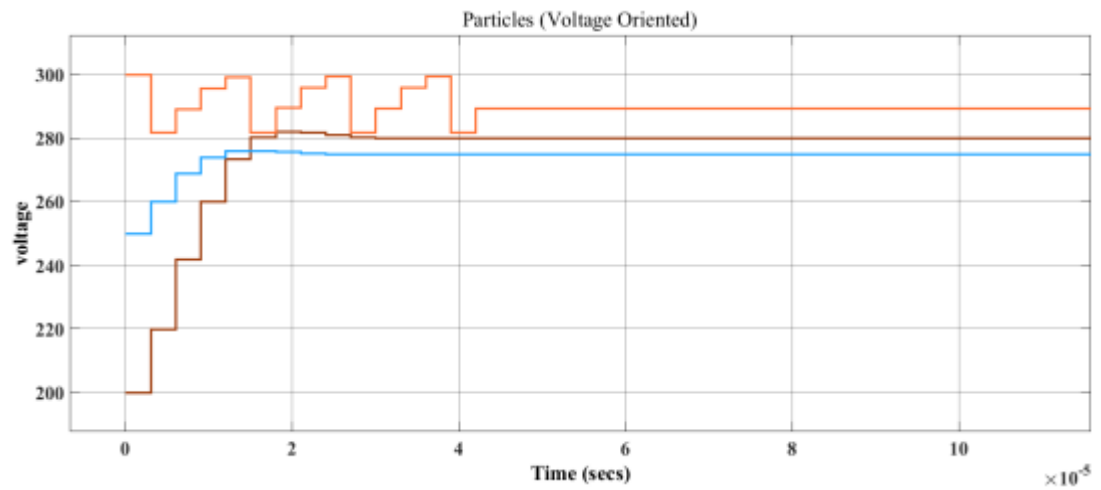


Figure 3.42 Particles of the PSO with their voltage values

## CHAPTER FOUR

### NEUTRAL POINT CLAMPED INVERTER

#### 4.1 Three level Inverter Approach:

Solar energy is converted to electrical energy with DC voltage being available using photovoltaic panels. The inverter acts as an interface between the DC solar panel output that is controlled via DC to DC converter and the grid to convert this DC voltage to AC voltage synchronized with the grid's frequency.

A neutral point-clamped pulsewidth modulation (PWM) is composed of main switching devices that are responsible for switching in PWM operation, and auxiliary switching devices that are responsible for clamping out the voltage output terminal to the neutral terminal connection. The inverter creates less harmonics in comparison with the conventional type inverters (Nabae et al ,1981). The unique PWM switching technique used in this thesis forces the common mode voltage to remain at a constant potential which is considered a crucial issue in dealing with grid connected PV arrays . In Figure 4.1 the grid connected single phase three level neutral clamped inverter's equivalent circuit is shown. The inductance between the inverter and the grid captures the instantaneous voltage difference between the inverter and grid.  $V_g$  is the grid's output voltage with  $V_o$  representing the output voltage of the boost converter which is the DC input voltage of the three level inverter.

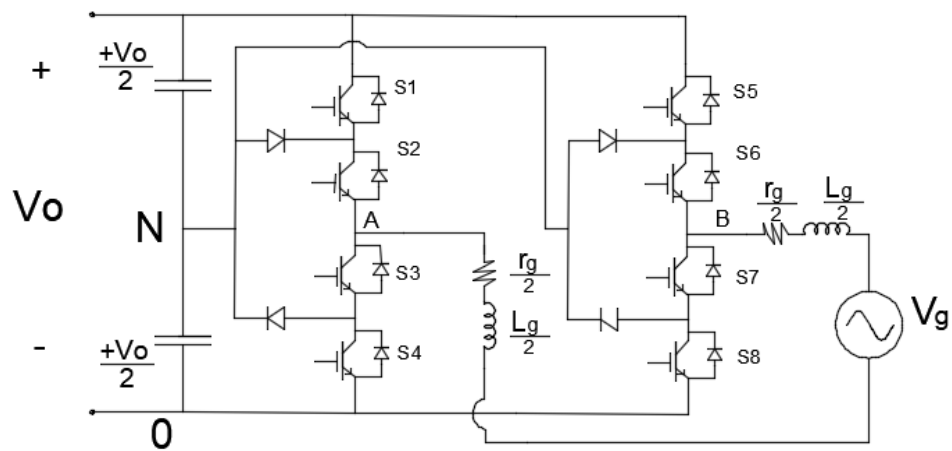


Figure 4.1 Single phase 3 level neutral clamped inverter

The general methodology of the three level inverter is to have diodes to clamp the switches to the zero level voltage thus in addition to  $\frac{V_o}{2}$ ,  $-\frac{V_o}{2}$ , a zero level voltage is obtained. This module though has more switches which act as a disadvantage to the inverter cost. With that in mind the inverter has now voltage sharing capabilities due to the clamped diodes which enables the design engineer to select half the voltage rating required from the previous model. During the positive and negative cycles the diodes provide path way for the current to proceed in freewheeling mode.

Voltage output with respect to switching sequence :

Table 4.1 switching sequence of three level inverter

S1	S2	S3	S4	VAN
1	1	0	0	$V_o/2$
0	1	1	0	0
0	0	1	1	$-V_o/2$

The IGBTs of the inverter are controlled by comparing the control signal with two carrier waves as shown in Figure 4.2. The switching logic creates pairs of complementary gate sequences fed towards the IGBTs (S1, S3) and (S2, S4). The complementary pairs of leg B (S5, S7) and (S6, S8) are obtained with comparison of  $V_{con}$  that is 180 degrees shifted with the same two carrier waves.

In the positive half cycle two different modes of operation exist, power processing (generating the output voltage  $V_{dc}$  level), and DC decoupling (generating the zero voltage via the neutral clamped diodes). S2 and S7 are always on state during the positive half cycle with S4, and S5 are turned off, in which the four switches are commutating at the grid's frequency. During this positive half cycle (S1, S3), and (S6, S8) are complementary with each other at the switching frequency of the three level inverter. The operation of these two complementary pairs allows the three level inverter to clamp out the voltage terminal with the neutral connection terminal via freewheeling diodes. S3 and S6 are always on state during the negative half cycle with S1, and S8 are turned off, in which the four switches are commutating at the grid's frequency.

During this negative half cycle (S2, S4), and (S5, S7) are complementary with each other at the switching frequency of the three level inverter. The operation of these two complementary pairs allows the three level inverter to clamp out the voltage terminal with the neutral connection terminal via freewheeling diodes. Therefore the common mode voltage is equal to half the input voltage  $V_0$  for all switching intervals. (FreeVideoLectures, 2019).

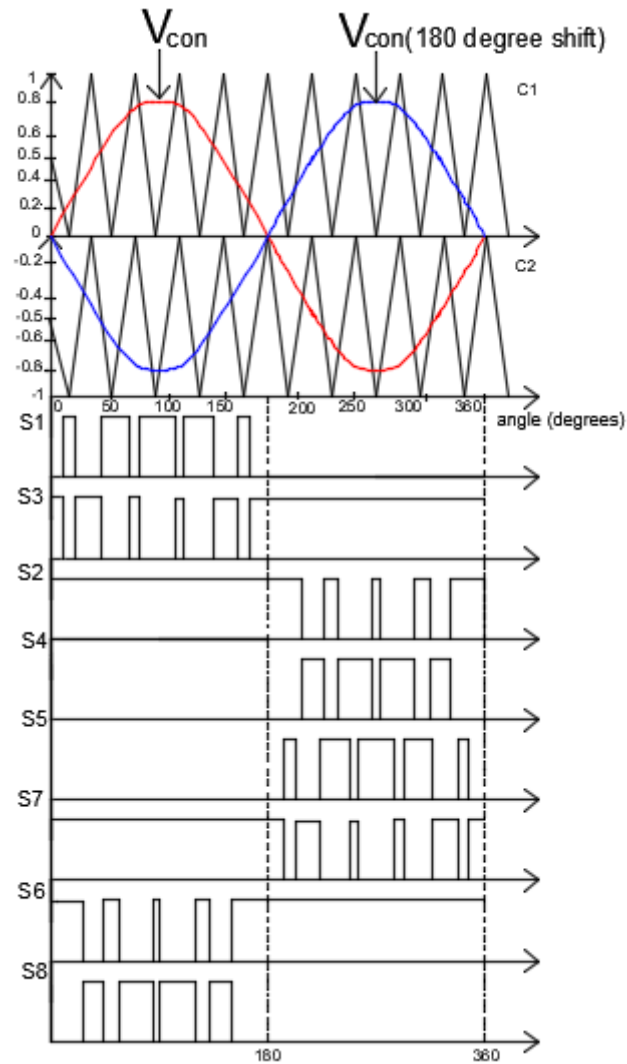


Figure 4.2 In phase modulation of three level inverter

#### 4.1.1 Selecting the proper DC bus link capacitance for NPC three-level Inverter

For grid tied PV array applications the inverter's power fluctuates at 100 hertz which is twice the frequency of the grid of 50 hertz. This power can be seen at the PV array terminal in which its active output power is reduced. Power variations due to the

single phase switching can be reduced or minimized with the proper selection of the input DC link capacitance of the inverter. According to the following equation 4.1 the DC link capacitance  $C_{DC}$  can be found (Ertasgin et al., 2019).

$$\frac{P_o}{\omega} = C_{DC}(V_{dcmax}^2 - V_{dcmin}^2) \quad (4.1)$$

where  $P_o$  the average output power of the PV ,  $\omega$  angular frequency of the grid ,  $V_{dcmax}$  , and  $V_{dcmin}$  are the minimum and maximum levels of the output voltage of the boost converter.

Bearing in mind minimizing the DC link value will decrease its overall cost, weight , and increase releability of the DC link storage of the inverter at the cost of allowing more levels of flucuations on the voltage output waveforms of both the PV , and the DC link voltage.(Ertasgin et al, 2019).

#### 4.2 Common Mode Voltage of the Neutral Point Clamped Inverter

The common mode voltage can be controlled by changing the inverter topology or by manipulating the switching logic to match a constant voltage output for all switching intervals, resulting in low leakage current.(Gonzales, 2008; Durbaba, 2018).Figure 4.3 shows the equivalent circuit of the single phase inverter connected to grid.Here, $C_p$  represents the parasitic capacitance,  $V_{gdm}$ , $V_{gcm}$  represent the grid terminal differential mode and common mode voltage. $L_1$ , and  $L_2$  represent the grid's inductance which are identical. $i_{cm}$  is the leakage current. (Durbaba, 2018).

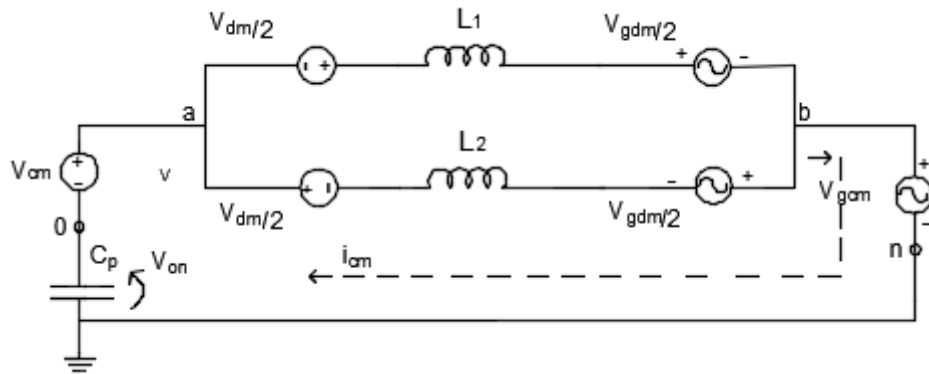


Figure 4.3 Equivalent Circuit of grid connected H Bridge based Inverter with PV array

In this thesis a study will be conducted on each cycle of the grid current to calculate the common mode voltage and see through in phase switching of the NPC inverter how it retains its value to a constant level at each cycle of the grid current. There are four modes of operation during one period of grid current. During the positive half cycle of the grid current there is active mode operation which is shown in figure 4.4 (a) and free wheeling mode of operation which is shown in figure 4.4 (b). During the negative half cycle of the grid current there is active mode operation which is shown in Figure 4.5 (a) and free wheeling mode of operation which is shown in figure 4.5 (b) .

The differential mode voltage can be written as follows (Gonzales, 2008; Durbaba, 2018):

$$V_{dm} = V_{A0} - V_{B0} \quad (4.2)$$

The common mode voltage can be written as follows (Gonzales, 2008; Durbaba, 2018):

$$V_{cm} = \frac{V_{A0} + V_{B0}}{2} \quad (4.3)$$

As seen before in the thesis leg A has 4 gate signals in which (S1,S3) ,and (S2,S4) are complementary with each other. Leg B has 4 gate signals as well in which (S5,S7) ,and (S6,S8) are complementary with each other as well.

During the positive half cycle of the grid current S2, S4, S5, and S7 are operating at grid frequency 50 Hz in which S2 and S7 are continuously conducting. During the active positive half cycle of the grid current the conducting switches are shown in figure 4.4 (a) and the common mode voltage is as follows:

$$V_{CM} = \frac{V_0 + 0}{2} = \frac{V_0}{2} \quad (4.4)$$

During the positive half cycle of the grid current, free wheeling operation is achieved with the conducting switches shown in Figure 4.4 (b) and the common mode voltage is as follows:

$$V_{CM} = \frac{\frac{V_0}{2} + \frac{V_0}{2}}{2} = \frac{V_0}{2} \quad (4.5)$$

During the whole positive half cycle of the grid current, the common mode voltage is kept at a constant voltage level which is half of the Dc link voltage  $V_0$ . During the negative half cycle of the grid current S1, S3, S6, and S8 are operating at grid frequency 50 Hz in which S3 and S6 are continuously conducting. During the negative half cycle of the grid current the conducting switches are shown in Figure 4.5(a) and the common mode voltage is as follows:

$$V_{CM} = \frac{0 + V_0}{2} = \frac{V_0}{2} \quad (4.6)$$

During the negative half cycle of the grid current, free wheeling operation is achieved with the conducting switches shown in figure 4.5 (b) and the common mode voltage is as follows:

$$V_{CM} = \frac{\frac{V_0}{2} + \frac{V_0}{2}}{2} = \frac{V_0}{2} \quad (4.7)$$

During the whole negative half cycle of the grid current, the common mode voltage is kept at a constant voltage level which is half of the Dc link voltage  $V_0$ .

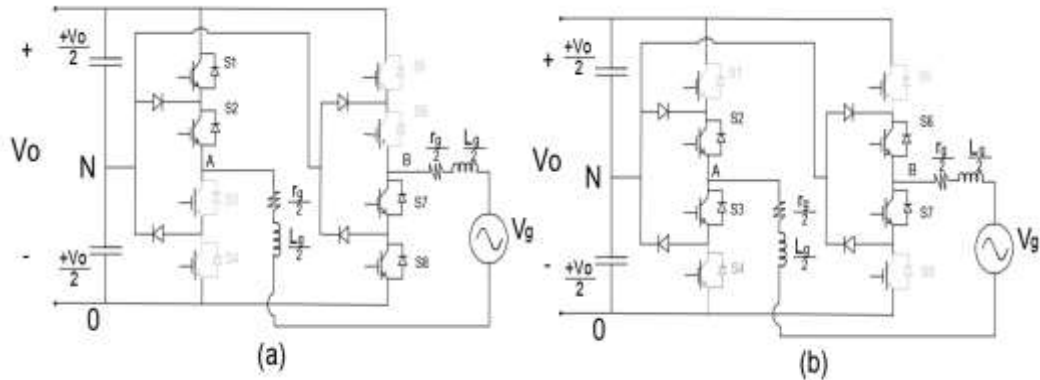


Figure 4.4 (a) Active current path of positive half cycle of grid current, (b) Freewheeling current path of positive half cycle of grid current



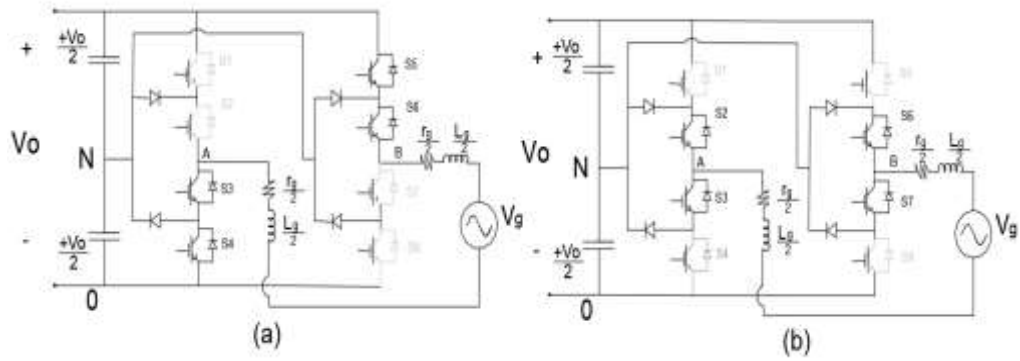


Figure 4.5 (a) Active current path of negative half cycle of grid current, (b) Freewheeling current path of negative half cycle of grid current

### 4.3 Proportional Resonant Controller for the Grid-connected Operation

The proportional resonant (PR) controllers are suitable for voltage/current control of grid interfaced converters. These controllers are useful for AC related applications in which due to their unique structure they provide infinite gain over a specific frequency thus the steady state error approaches zero. Another possibility is implementing the PR controller as selective harmonic compensators without the need for extensive computations (Islam et al, 2016). In this thesis the PR controllers are utilized for the single phase three level inverter control scheme via OSG topology.

Figure 4.6 shows the equivalent representation of the PR controller showing how it is devised from the error signal multiplying it with both sine and cosine signals synchronized with the grid's frequency using phase locked methodology also known as PLL methodology (Hu et al, 2009; Teodorescu et al, 2006).

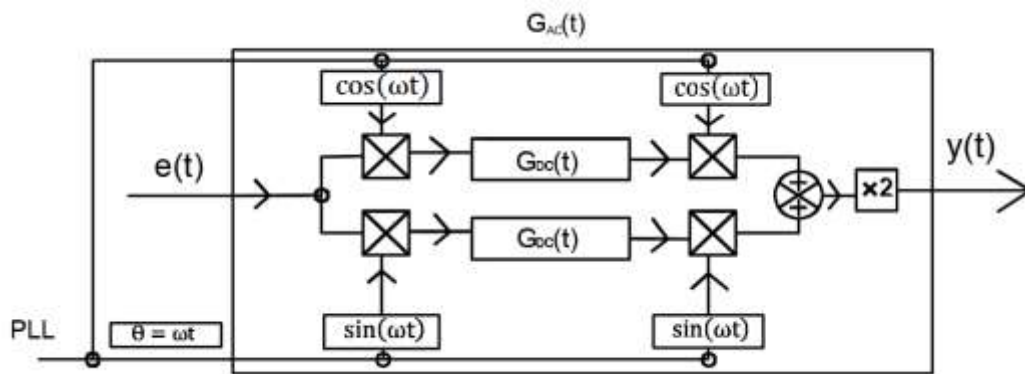


Figure 4.6 Equivalent representation of a PR controller

The equivalent transfer function of the PR controller using the ideal and non ideal integrators yields to equations 4.8, and 4.9 respectively (Hu et al, 2009).

$$G_{AC}(s) = \frac{Y(s)}{E(s)} = 2K_p + \frac{2K_i s}{s^2 + \omega^2} \quad (4.8)$$

With a propotional gain component  $K_p$  we obtain an ideal PR controller (4.8) with an infinite gain at the ac fundamental frequency in which the dynamics of the system in terms of bandwidth, phase and gain margin can be calibrated with the gain component. To avoid the problem of infinite gain we can use non-ideal PR controller (4.9) in which  $K_i$  is calibrated to shift the magnitude of the vertical output or response. Aside from PR controllers also selective harmonic compensators can be used in a cascaded form to insert and resonate at an integer multiple of the fundamental frequency in which the transfer function is of following (Teodorescu, 2006):

$$G_{AC}(s) = \frac{Y(s)}{E(s)} = \frac{2K_i \omega_c s}{s^2 + 2\omega_c s + \omega^2} \quad (4.9)$$

$$G_h(s) = \sum_{h=3,5,7} \frac{2K_{ih} s}{s^2 + (h\omega)^2} \quad (4.10)$$

$$G_h(s) = \sum_{h=3,5,7} \frac{2K_{ih} \omega_c s}{s^2 + 2\omega_c s + (h\omega)^2} \quad (4.11)$$

Considering  $k_{ih}=1$ ,  $\omega = 2\pi f$ ,  $f=50$  Hz,  $\omega_c=1$ ,  $k_p=2.5$  and  $k_{i1}=2.5$ , figures 4.7 and 4.8 represent the bode diagram for the propotional resonant controller and the harmonic compensators respectively.

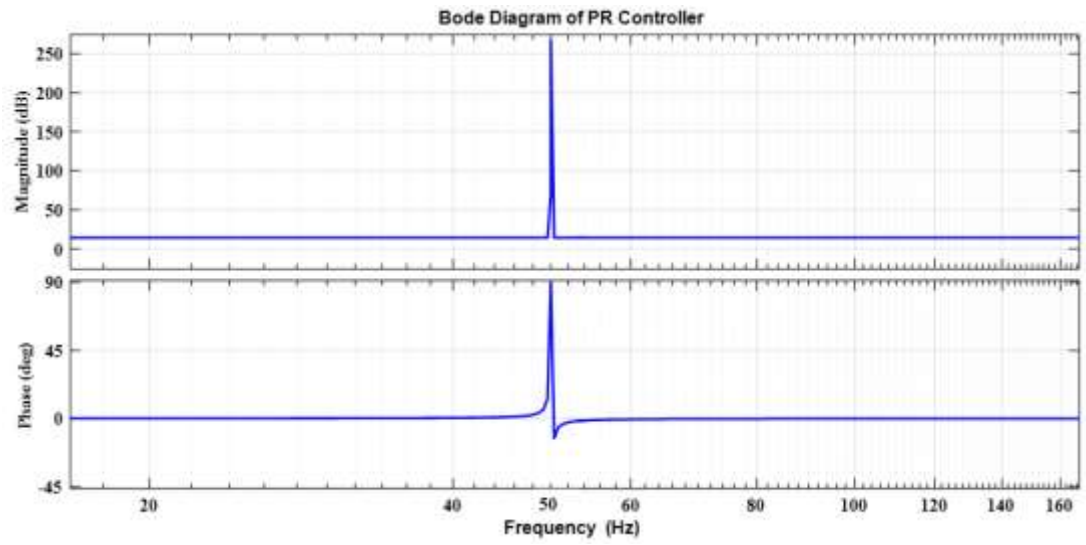


Figure 4.7 Bode diagram for PR

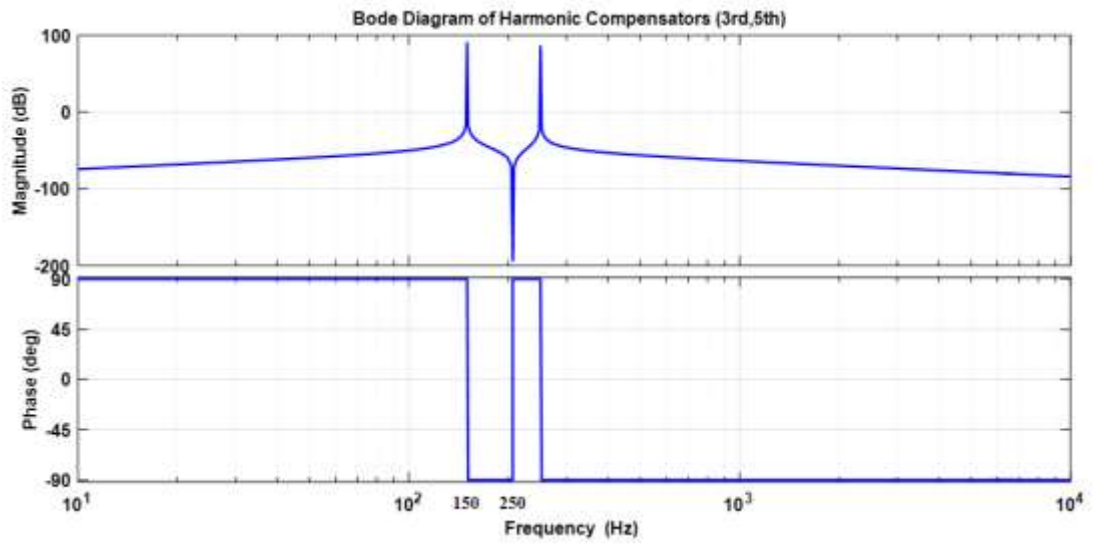


Figure 4.8 Bode diagram for HC (3rd, 5th)

#### 4.4 Orthogonal Signal Generator (OSG)

The OSG topology is used to transfer the voltage and current waveforms into alpha and beta components that are orthogonal to each other. The objective of this methodology is to be able to control the active and reactive power delivered by the three level inverter precisely and independently. Using this methodology both active and reactive power components can be calculated as shown in Figure 4.9 and following equations 4.12, and 4.13 (Islam et al, 2016).

$$P_{Cal} = \frac{1}{2} [v_{g\alpha} i_{g\alpha} + v_{g\beta} i_{g\beta}] \quad (4.12)$$

$$Q_{Cal} = \frac{1}{2} [v_{g\beta} i_{g\alpha} - v_{g\alpha} i_{g\beta}] \quad (4.13)$$

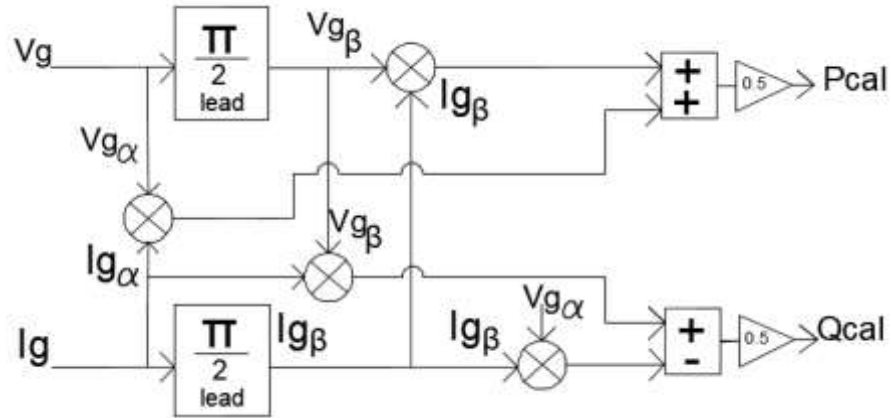


Figure 4.9 OSG control with power calculation

After obtaining the corresponding calculated real and reactive powers, the reference grid current that will force the grid current to follow it and deliver the reference active and reactive power can be calculated as follows (Islam et al, 2016):

$$i_g^* = \frac{[(P_{ref} - P_{cal}) * G_p(s) * v_{g\alpha} + (Q_{ref} - Q_{cal}) * G_q(s) * v_{g\beta}]}{v_{\alpha}^2 + v_{\beta}^2} \quad (4.14)$$

where  $G_p(s)$ , and  $G_q(s)$  are the transfer functions of the PI controllers shown in Figure 4.10.

successful. Thus obtaining independent instantaneous reactive and active power control of the inverter to the grid. Finally, DC link PI controller is used to maintain the DC link voltage to a constant 400 volt in order for the system to run properly.

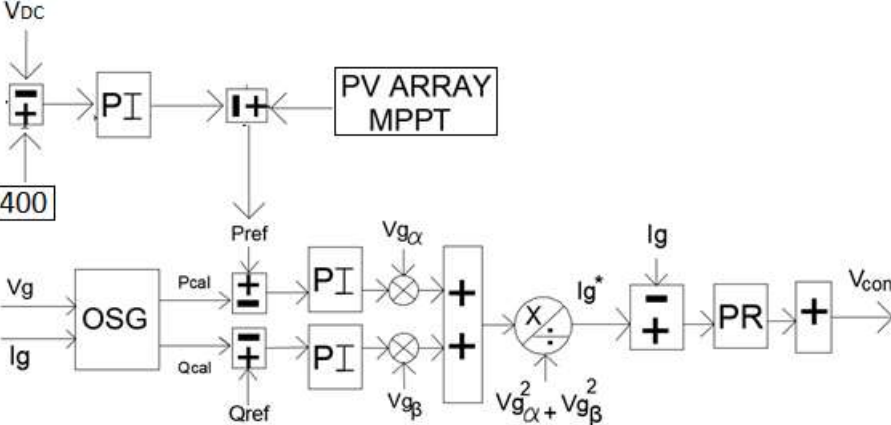


Figure 4.10 Active and reactive power control using OSG

## CHAPTER FIVE

### GRID CONNECTED NEUTRAL POINT CLAMPED INVERTER WITH PV ARRAY

#### 5.1 Duty Cycle-based P&O and Neutral Point Clamped Inverter

In this thesis, the PV array is operated with various MPPT algorithms such as duty based perturb and observe, voltage oriented perturb and observe, and particle swarm optimization algorithm. A comparative study is conducted between the various MPPT algorithms in which the PV array is controlled by the DC to DC boost converter. The DC to DC boost converter controls the PV array either directly by the duty cycle generated from the MPPT algorithms or by the reference voltage generated from the voltage oriented perturb and observe algorithm, in which predictive valley current control methodology is implemented. In addition, a DC to AC neutral clamped three level inverter is used to interface the DC voltage of the PV array to the grid. An orthogonal system generation based control scheme is implemented on the three level inverter to precisely deliver and control both active and reactive power components independently in which the PV array's maximum output power  $P_{mppt}$  is used as active power reference component  $P_{ref}$  for the OSG control scheme to follow upon. Figure 5.1 represented the overall structure of the entire system .

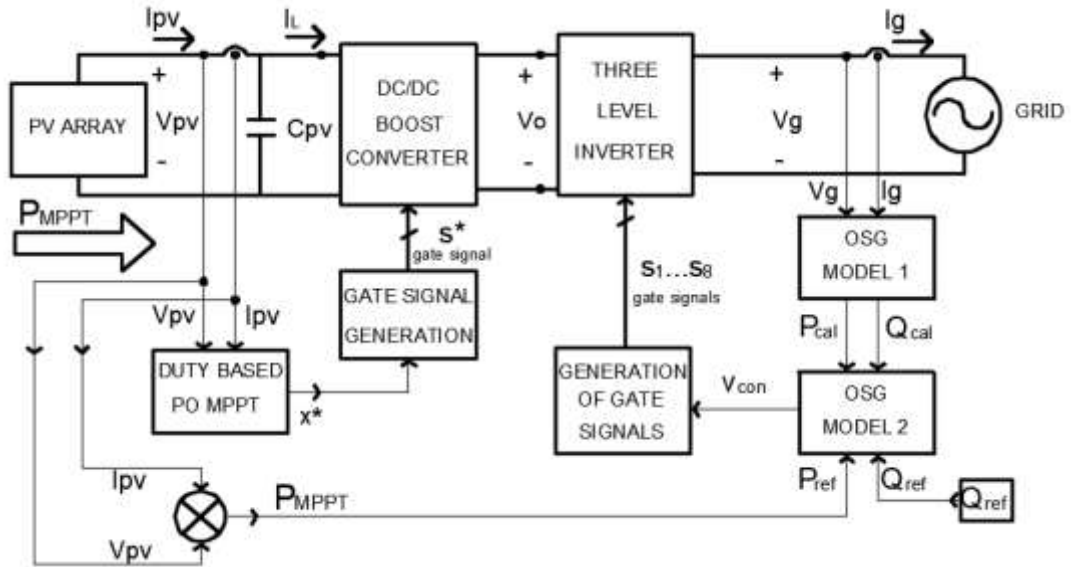


Figure 5.1 General structure of the entire grid connected PV array with duty based PO MPPT algorithm

The duty based perturb and observe algorithm is implemented according to equations 3.1, and 3.2 and the flowchart shown in Figure 3.1 in which  $x^*$  is the reference output duty cycle which represents the MPP of the PV array.  $V_{pv}$ , and  $I_{pv}$  represent the voltage and current outputs of the PV array respectively.  $S^*$  is the gate signal for the DC to DC boost converter to operate upon in which Figure 5.2 illustrates how a triangular carrier signal C1 is compared with the reference duty cycle  $x^*$  to obtain reference gate signal  $S^*$  at 10000 Hz switching frequency. Using the components of the DC to DC boost converter that were designed and calculated according to contents of Chapter 2, and the input capacitance of the boost converter  $C_{pv}$  according to equation 3.24 the PV array is connected directly to the boost converter in which an output voltage  $V_o$  is acquired from the overall operation.

A neutral clamped three level inverter is connected directly to the DC to DC output voltage of the boost converter in which the inverter overall structure and generation of the gate signals  $S1...S8$  are acquired as discussed in Chapter 4. The outputs of the two legged three level inverter have identical resistance and reactive components  $r_g$ , and  $L_g$  to capture the instantaneous voltage difference between the three level inverter and the grid. The neutral clamped three level inverter is connected afterwards to the grid thus feeding active and reactive power directly and solely from the PV array via orthogonal system generation (OSG) control methodology.  $V_g$ , and  $I_g$  represent the voltage and current outputs of the grid respectively in which they are used as inputs for the OSG model 1 block.

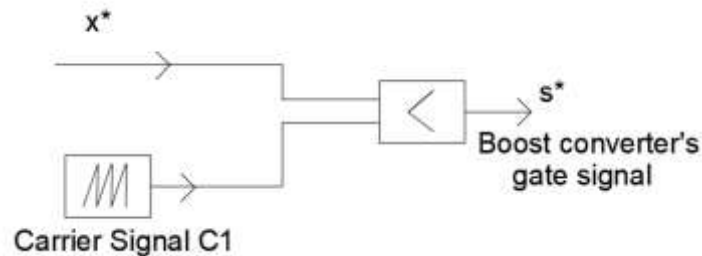


Figure 5.2 Gate signal generation of the duty based perturb and observe MPPT algorithm

OSG model 2 block takes four inputs,  $Q_{ref}$  is the reference reactive power that the user inputs, and  $P_{ref}$  is obtained from the subtraction between the output power of the

MPPT driven PV solar array using various algorithms mentioned earlier, and the output difference between the DC link voltage, and reference DC link voltage after being regulated by the PI controller. The output of the OSG model 2 block is the control voltage  $V_{con}$  in which from this control voltage gate signals are acquired for operating the three level inverter. Therefore, active power is directly being delivered from the PV array through DC to DC conversion via boost converter, and DC to AC interfacing using the three level inverter to the grid. It is worth noting that grid synchronization of the three level inverter is acquired due to the fact that an image of  $V_g$  and  $I_g$  is taken from the grid and operated upon is OSG model 1 block. In addition, the operation of the proportional resonant integrator, and the presence of the harmonic compensators in OSG model 2 block are tuned to the grid's own frequency which is 50 Hz. Figure 4.10 illustrates how the OSG model 2 block uses its four inputs to acquire the control voltage. It is worth noting that  $I_g^*$  is the reference current that forces the grid current  $I_g$  to follow its path in which it is obtained according to the equation 4.14.

$V_{con}$  is used as input for generation of the gate signals block in which Figure 5.3 illustrates how in phase switching of the three level inverter occurs. The control voltage is shifted 180 degrees in which both the original control voltage and the 180 degree phase shifted control voltage are compared with two trailing edge triangular carrier waveforms C3, and C4 respectively in which in phase switching occurs thus obtaining a constant common mode voltage as discussed earlier in Chapter 4.



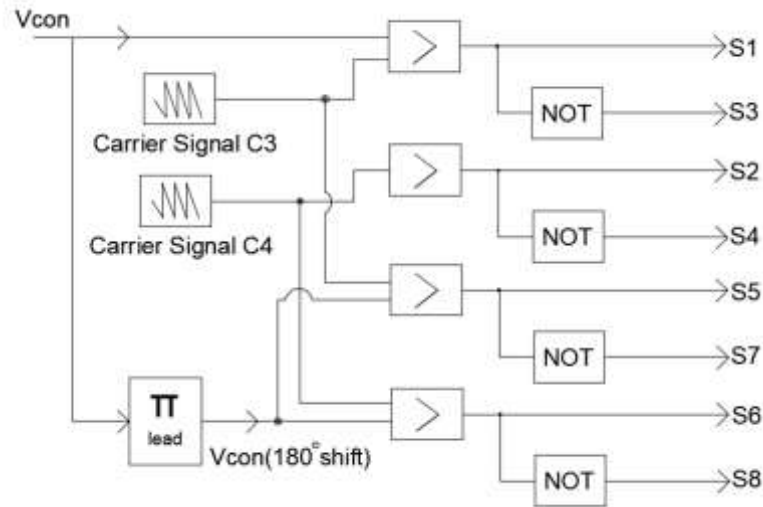


Figure 5.3 Generation of inverter gate signals block

## 5.2 Duty Cycle-based PSO and Neutral Point Clamped Inverter

The entire system is operating under the same conditions as mentioned earlier as seen in Figure 5.4 however, PV array array now being driven by the particle swarm optimization MPPT algorithm according the flowchart mentioned in Chapter 3 and shown in Figure 3.5. The PSO methodology is quick to survey the non linear I-V curve of the PV array to track down and lock the MPP in which the main advantage of this method is at steady state there is no need for the attenuation of the duty cycle any longer. Unlike the conventional perturb and observe MPPT algorithm the attenuation of the duty cycle never ceases to stop thus creating unnecessary fluctuations in both the output voltages of the PV array and the inductance current of the boost converter.

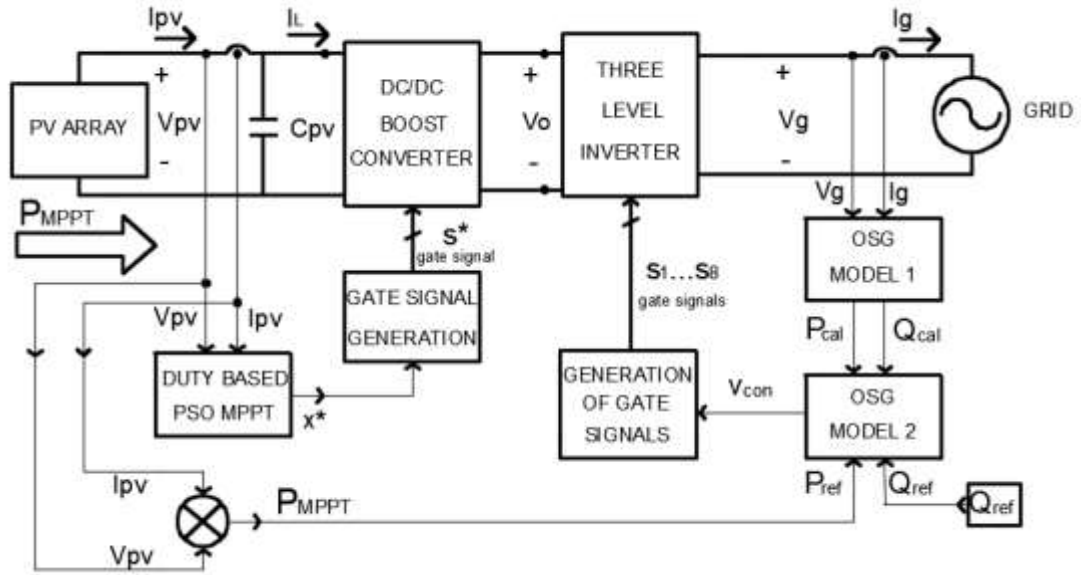


Figure 5.4 General structure of the entire grid connected PV array with duty based PSO MPPT algorithm

### 5.3 Voltage Oriented P&O with predictive current control and Neutral Point Clamped Inverter

In this section, the DC to DC boost converter is now controlled or driven by predictive control in which the valley, and average based predictive current control methodology are adopted. The conventional perturb and observe MPPT algorithm is voltage oriented meaning attenuation occurs on the output voltage of the PV array  $V_{pv}$ , and the output of this algorithm is the reference voltage  $v^*$  that guides the predictive model to control the valley or average current of the inductance current  $I_L$ . Figure 5.5 is the general structure of the current topology in which a proportional integrator PI is necessary for this kind of operation. The output voltage of the PV  $V_{pv}$ , and the voltage oriented PO MPPT block are subtracted from each other and the error  $e$  is fed through the PI controller. The output current  $I_v$  is summed up with the PV output current  $I_{pv}$  in which the output  $I_{ref}$  represents the current reference for the predictive current control operation of the boost converter.

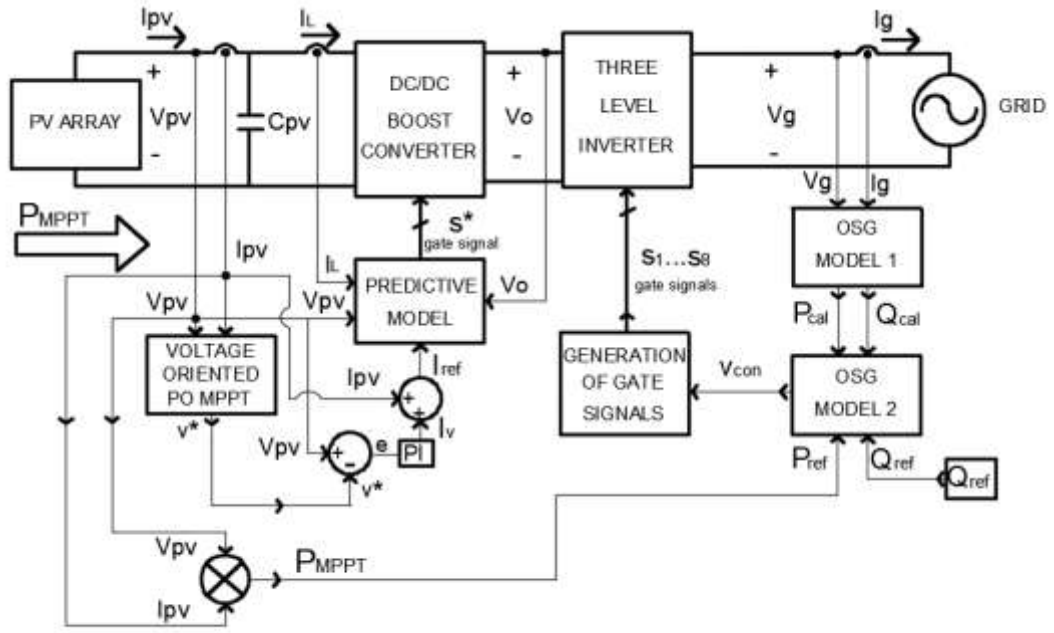


Figure 5.5 general structure of the entire grid connected PV array with voltage-oriented PO MPPT algorithm, and Predictive current control

According to the equation 2.18, two step horizon valley based predictive current control can be implemented on the DC to DC boost converter. The block takes the inductance current  $I_L$ , the output voltage of the DC to DC boost converter  $V_o$ , and the current output of the PV array  $I_{pv}$  as inputs. Using trailing edge triangular modulation the carrier signal  $C_2$  is compared with the output duty cycle  $d$  to obtain  $s^*$  which represents the boost's gate signal. This methodology also at steady state ceases to attenuate the duty cycle thus no unnecessary fluctuations exist on the output voltage of the PV array  $V_{pv}$ , and the inductance current  $I_L$ . The implementation can be illustrated as shown in Figure 5.6. The same can be applied for average based predictive current control in which implementation is based upon equation 2.24 as shown in Figure 5.7.

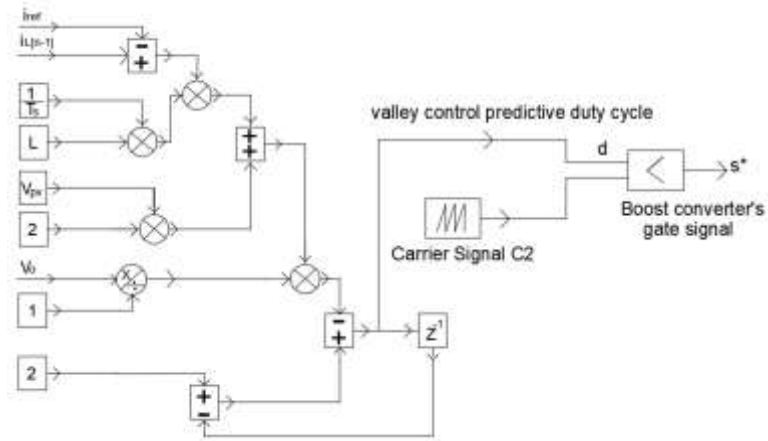


Figure 5.6 Predictive model block (Valley based)

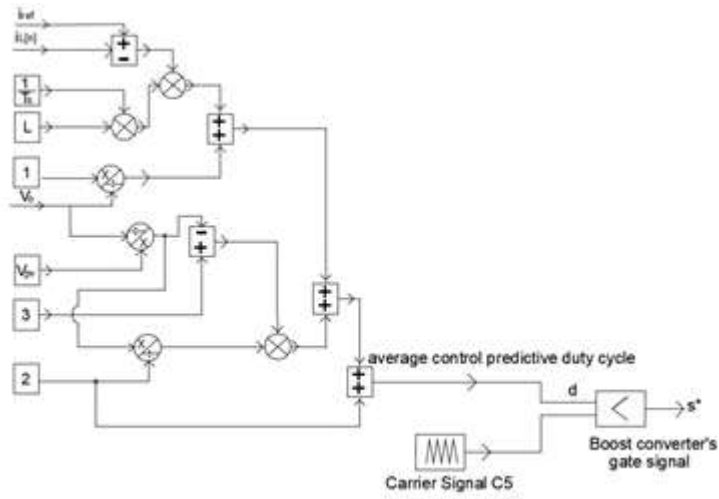


Figure 5.7 Predictive model block (Average based)

#### 5.4 Voltage Oriented PSO with predictive current control and Neutral Point Clamped Inverter

In this section, the DC to DC boost converter is now controlled by the predictive control in which the valley or average based predictive current control methodology are adopted. Particle swarm optimization MPPT algorithm is voltage attenuated, and the output of this algorithm is the reference voltage  $v^*$  that guides the predictive model to control the valley or average current of the inductance current  $I_L$ . Figure 5.8 is the general structure of the current topology in which a propotional integrator PI is necessary for this kind of operation. The output voltage of the PV  $V_{pv}$ , and the voltage output of the oriented PSO MPPT block are subtracted from each other and the error  $e$  is fed through the PI controller. The output current  $I_v$  is summed up with the PV output current  $I_{pv}$  providing the output  $I_{ref}$  represents the current reference for the predictive current control operation of the boost converter.

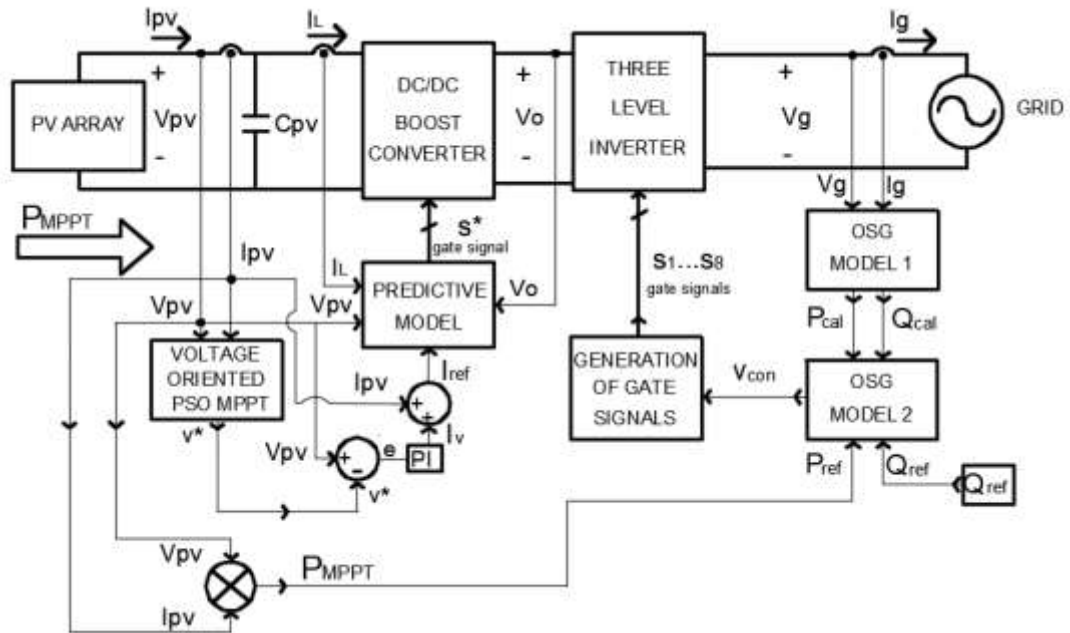


Figure 5.8 General structure of the entire grid connected PV array with PSO MPPT algorithm, and Predictive current control.

## **CHAPTER SIX**

### **SIMULATION RESULTS**

The simulations have been carried out for single phase grid connected PV array under the control of the DC to DC boost converter with various MPPT algorithms , and under the control of the DC to AC three level inverter with it being controlled by the OSG topology as mentioned in chapters 2, 3, and 4 in which the whole system has been merged together according to chapter 5. In this thesis a comparative study has been made between various MPPT algorithms with the implementation being done on the system as a whole. All the simulations have been carried out in the MATLAB/SIMULINK environment in which the figures below show how implementation was carried out possible. The system parameters are given in Table 6.1. The simulations are all carried out under a constant  $1 \text{ kW/ m}^2$  irradiance , and a constant 25 degree celcius temperature conditions.

#### **6.1 Control of Inverter Connected to grid (OSG)**

Figure 6.1 shows clearly how the assembly of the three level inverter in which phase A, and B are connected with the grid inductance to capture the instantaneous voltage difference between the inverter and the grid as mentioned in chapter 5. In addition , figure 6.2 shows how the three-level inverter is connected directly towards the grid in which synchronization and power control is achieved via orthogonal system generator, PI, and PR controllers as mentioned in Chapter 5.

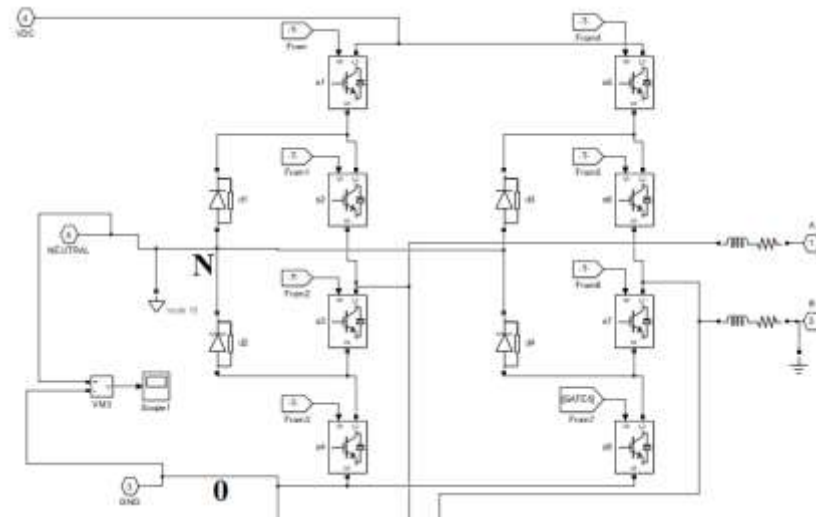


Figure 6.1 Structure of three level inverter

Table 6.1 Parameters of the grid connected PV array (including the boost converter and the three-level inverter)

Symbol	Parameter	Value
$V_g$	Grid voltage	220 V (RMS)
$f_g$	Grid Frequency	50 Hz
$V_o$	DC Bus Voltage	400 V
$C_{DC}$	Buss capacitance (each)	7.69 mF
$L_g$	Line Filter inductance	4 mH
S1...S8	Gate signals for three level inverter	(0,1)
$f_{s1}$	Switching frequency of three level inverter	4000 Hz
$f_{s2}$	Switching frequency of Boost converter	10000 Hz
$f_{MPPT}$	Switching frequency of MPPT algorithm	1000 Hz (PO) 1000 Hz (PSO) 1000 Hz (voltage oriented PO MPPT Based Predictive) 1000 Hz (duty oriented PSO MPPT Based Predictive)
$C_{pv}$	input capacitance of boost converter	3.705 $\mu$ F
$C_{out}$	output capacitance of boost converter	2.77 mF
$L_b$	boost inductance	5 mH
$r$	Internal resistance of boost inductance	2m $\Omega$
$T_{delay}$	Time delay for boost gate signal, and OSG control system.	0.02 s
$K_{p1}, K_{i1}$	DC link PI controller constants	7 , 0.4
$K_{p2}, K_{i2}$	$P_{ref}$ PI controller constants	0.96 , 2.8
$K_{p3}, K_{i3}$	$Q_{ref}$ PI controller constants	0.96 , 2.8
$K_{p4}, K_{i4}$	PR controller constants	5 , 5.5
$K_{i5}$	HC(3 <sup>rd</sup> harmonic) controller constants	1
$K_{i6}$	HC(5 <sup>th</sup> harmonic) controller constants	1

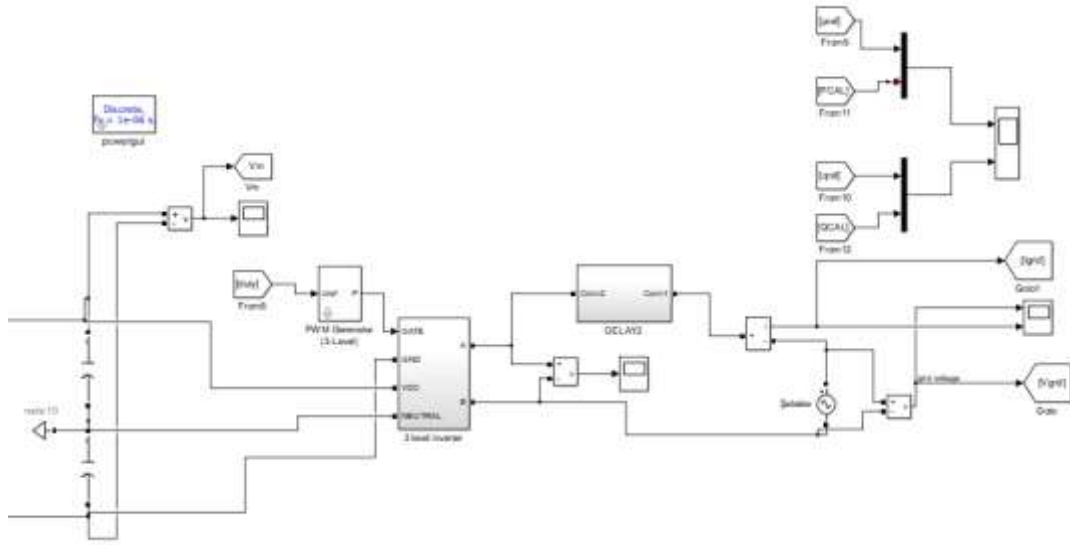


Figure 6.2 The DC to AC three level inverter connected to the grid

Using the equations 4.12 and 4.13 the calculated active and reactive power components of the OSG can be obtained as shown in Figure 6.3. Synchronization with the grid is obtained since both voltage and current outputs of the grid are used for the generation of the power reference components via OSG, and with the help of the PR controller used in Figure 6.6 that uses PLL to eliminate the AC steady state error as mentioned in chapter 4. All the calculated powers, voltage, and current waveforms are taken from the OSG block into the control module as shown in Figure 6.4, and 6.5. A reference current  $I_g^*$  is obtained according the equation 4.14 in which the grid current is forced to follow it.  $P_{ref}$ , and  $Q_{ref}$  represent the reference power points for the system in which  $P_{ref}$  is obtained from the subtraction between the output power of the MPPT driven PV solar array using various algorithms mentioned earlier, and the output difference between the DC link voltage, and reference DC link voltage after being regulated by the PI controller as discussed earlier.



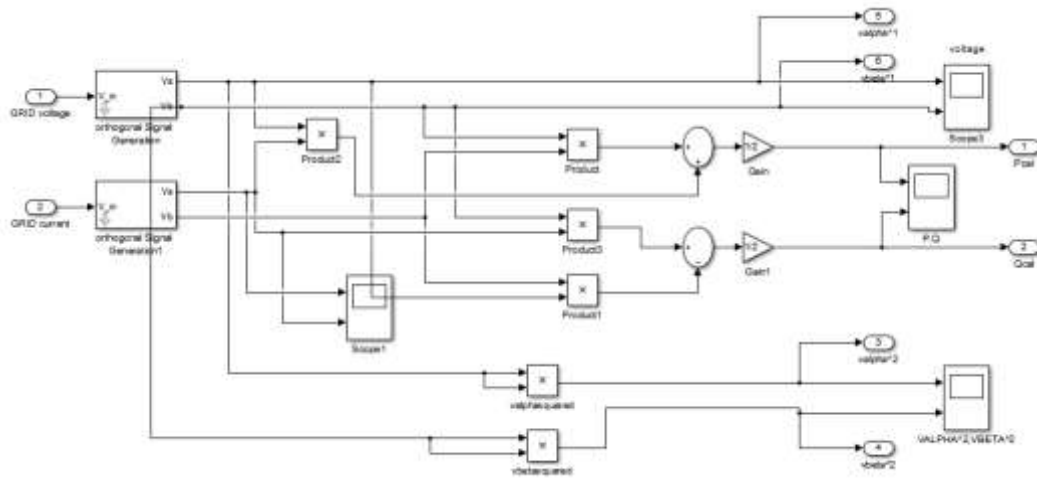


Figure 6.3 OSG with power calculation

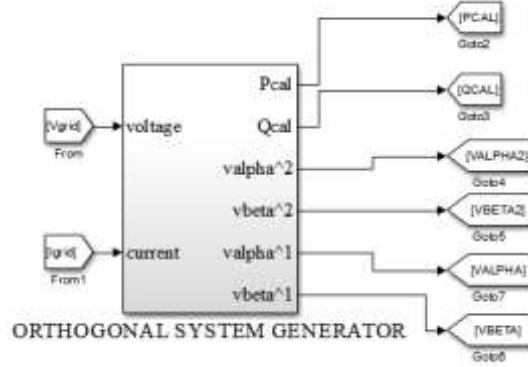


Figure 6.4 Orthogonal System Generator

Proportional integrators found in Figure 6.5 have the following discrete equation in which all of their respective gain and integral constants are given in table 6.1

$$PI(z) = K_P + K_I \left( \frac{1}{z-1} \right) \quad (6.1)$$

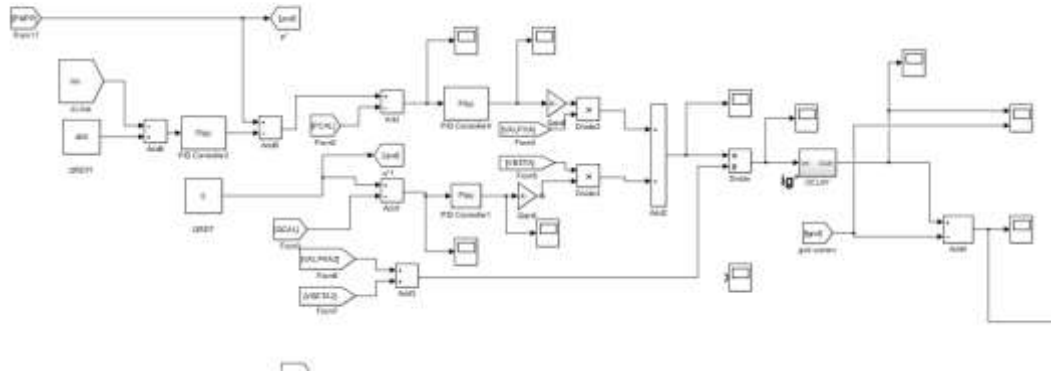


Figure 6.5 OSG scheme with independent active and reactive control

Using equations 4.10 and 4.11 the transfer functions of both PR controller and Harmonic compensator have been implemented with the HC accounted up to the 7<sup>th</sup> harmonic. In addition, a PI controller is used for the control of the DC link voltage at 400 volts. Figure 6.6 represent the Simulink block diagrams of the PR, and HC in which the output will be  $V_{con}$  which represents the voltage control that creates the gate signals that control the three-level inverter. Figure 6.7 represents how in phase switching has been implemented, and Figure 6.8 represents the output gate signals as a result of in phase switching in which it can be seen clearly how two complementary pairs of signals are obtained for each leg as mentioned in Chapter 4.

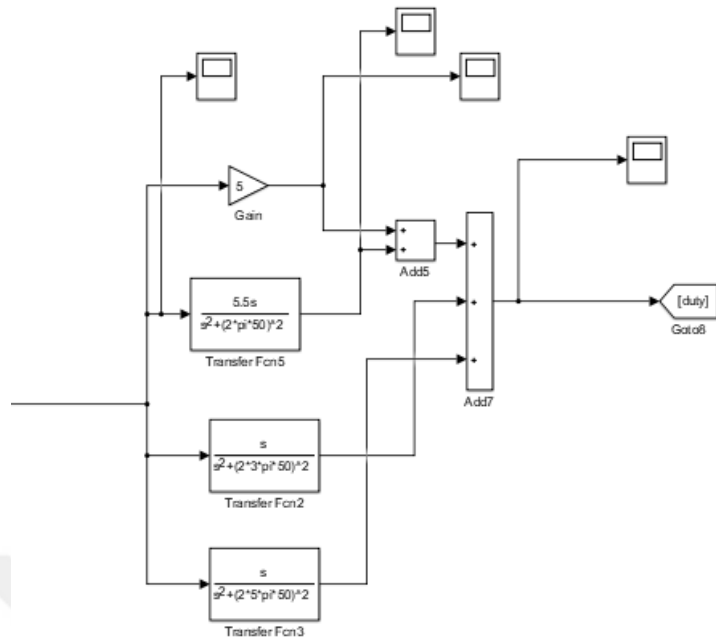


Figure 6.6 PR and HC controllers

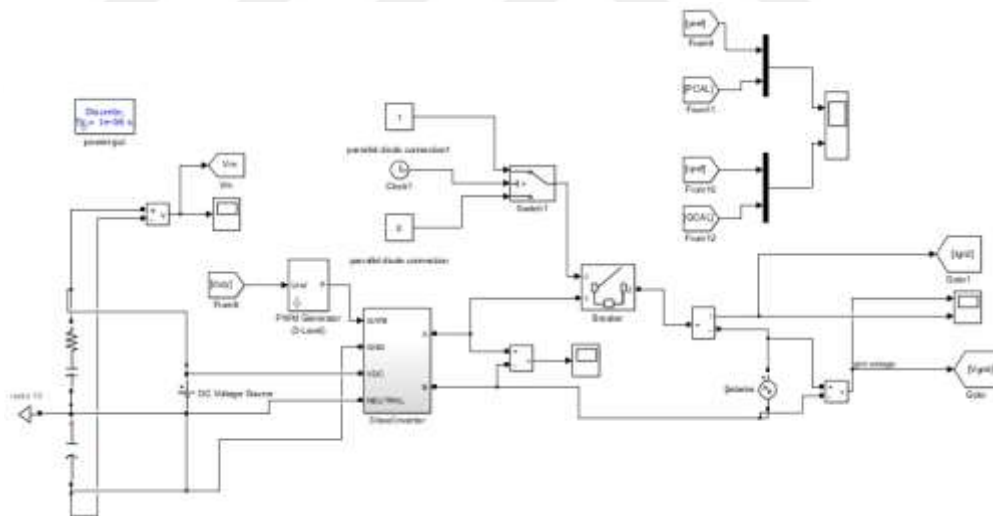


Figure 6.7 Simulink PWM Generator (3-level) Block

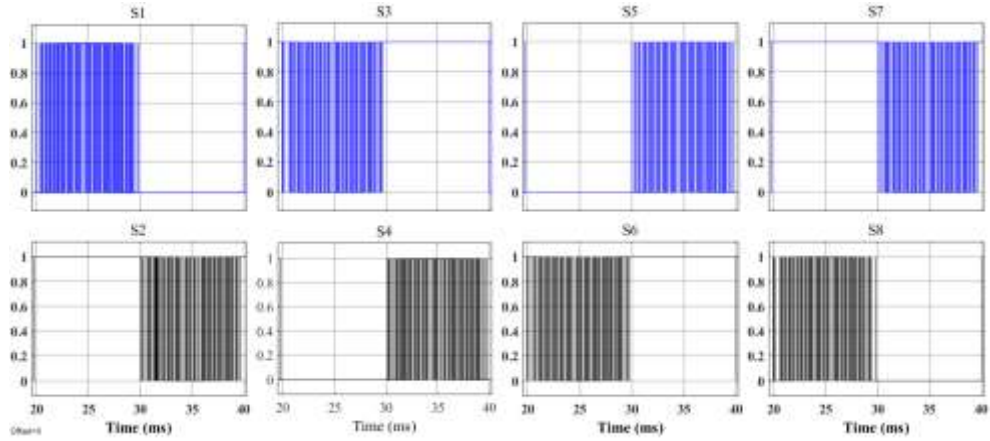


Figure 6.8 In phase switching gate signals

### 6.1.1 Implementing OSG with Inverter

Figure 6.9 show the phase to DC ground output voltages of the three-level inverter in which Figure 6.10 represents the subtraction between the phases of these voltage output waveforms. Using the in phase switching the three-level inverter has successfully forced the common mode voltage which is half of the summation of the output voltage waveforms to appear constant as seen in figure 6.11 which in fact represents the main advantage of the three-level inverter over the conventional two-level inverter. Both  $P_{ref}$  and  $Q_{ref}$  are reference inputs inserted by the user for the purpose of changing them independently to see if there is any mutual response. The input voltage of the three level inverter is a constant 400-volt battery. The orthogonal system generator with the help of both PI and PR controllers both active and reactive power outputs have successfully tracked the reference power with zero steady state error, in which no unnecessary fluctuations have been encountered.

The overshoot of both active and reactive powers is approximately 10 percent as it is seen in Figure 6.12. Figure 6.13 shows the grid current being forced to follow the OSG reference current  $I_g^*$ . It is worth noting that the main advantage of the OSG system is that the active and reactive power are completely independent from one another. Finally, in Figure 6.14 the calculated instantaneous active and reactive power outputs of the inverter by OSG are observed

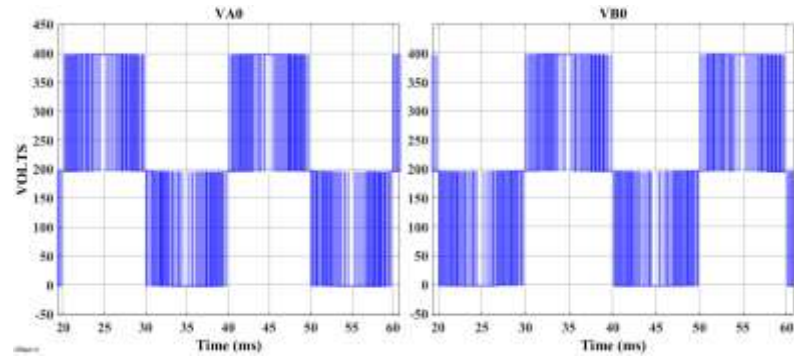


Figure 6.9 Phase to DC Gnd output voltages of 3 level inverter

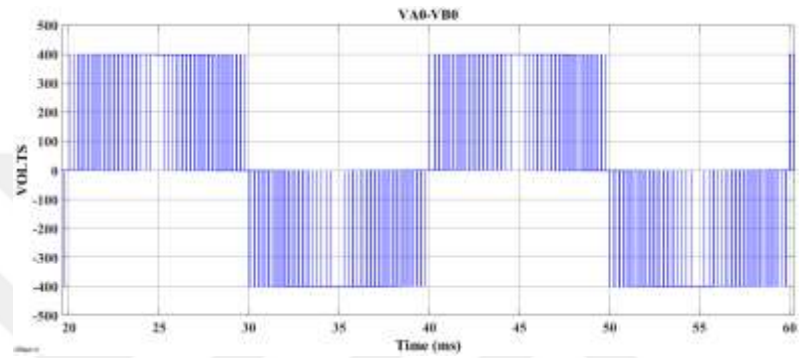


Figure 6.10 Phase to phase inverter output voltage waveform

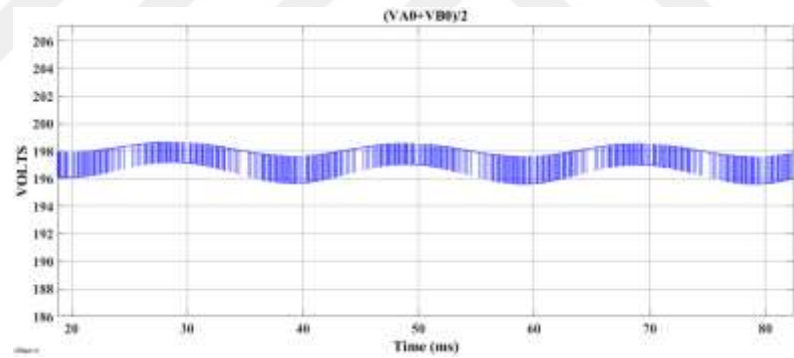


Figure 6.11 Common mode voltage waveform

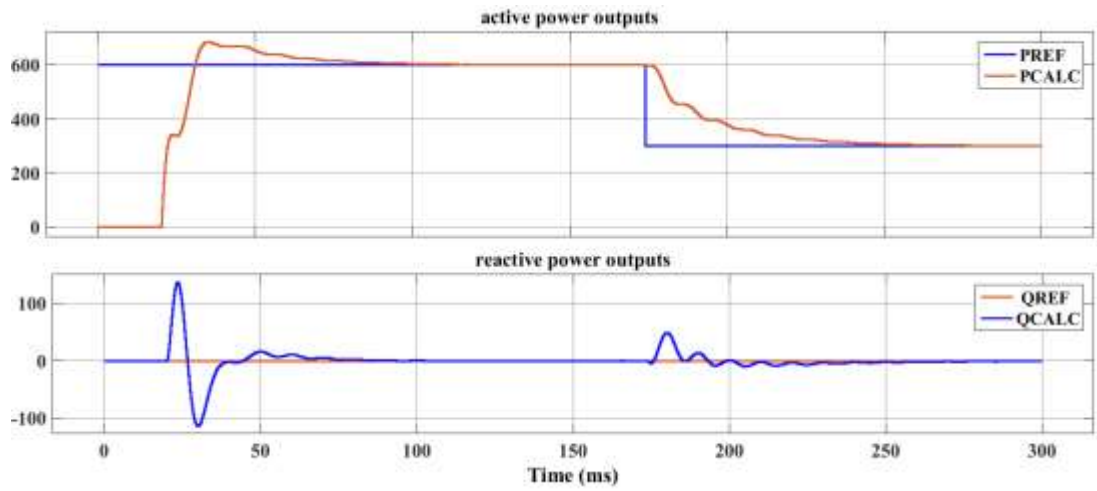


Figure 6.12 Active and reactive output of three level inverter

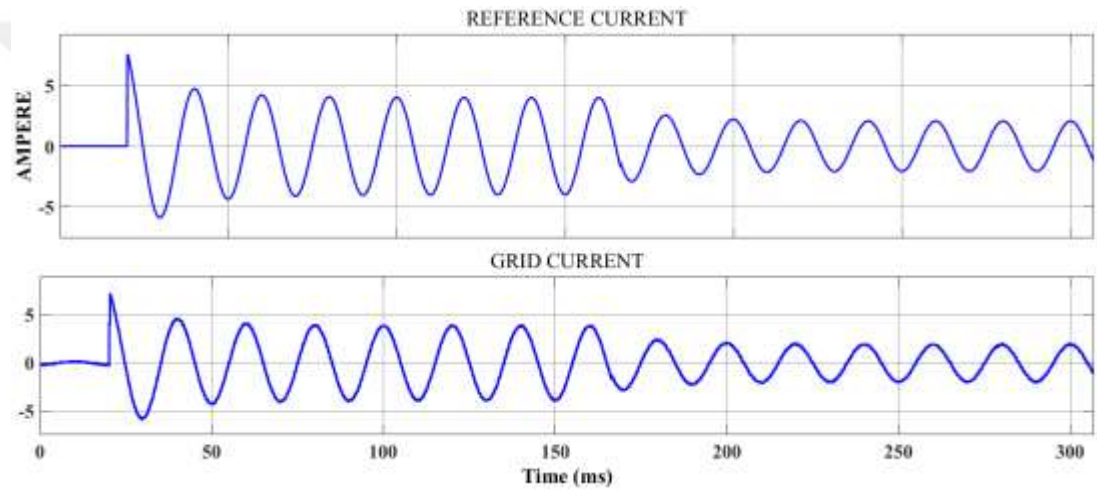


Figure 6.13 Reference and inverter current waveforms

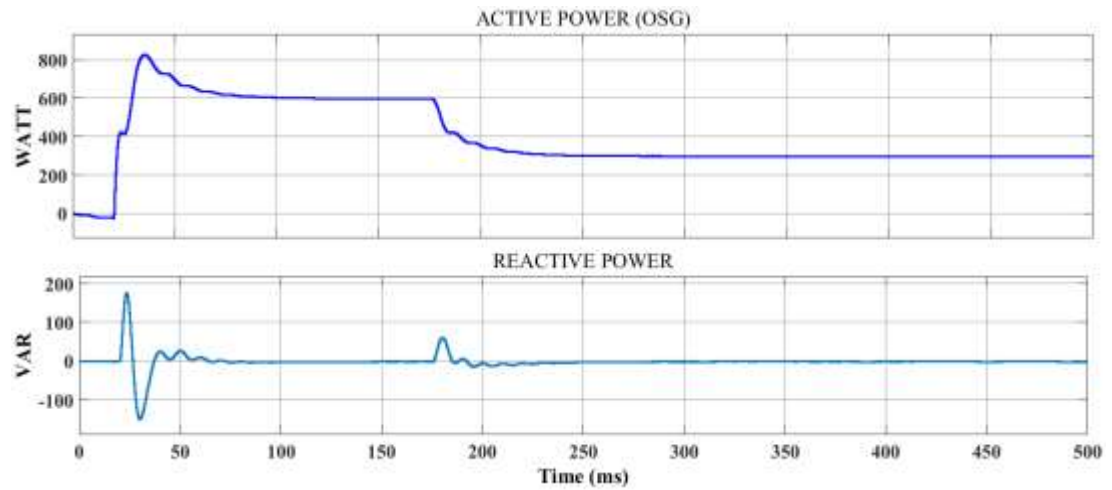


Figure 6.14 Calculated active and reactive power outputs of OSG

## 6.2 Two Different MPPT Methods with Inverter Connected to the Grid

### 6.2.1 Duty Cycle Based Perturb and Observe

The duty cycle is disturbed at 1000 Hz in which the constant irradiance, and temperature are  $1000 \left(\frac{W}{m^2}\right)$ , 25 degrees Celsius respectively. The system is now connected as a whole identical to what has been mentioned in chapter 5 in which figure 6.5 illustrates how the Simulink model of the entire system is connected.

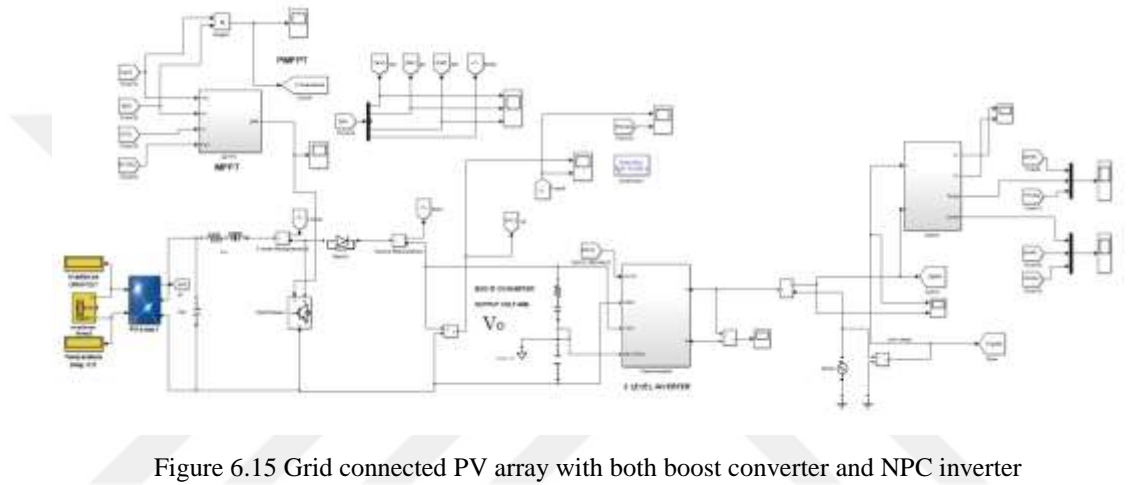


Figure 6.15 Grid connected PV array with both boost converter and NPC inverter

The oscillation of the inductance current due to the step change of duty cycle in both Figures 3.6, and 3.9 is successfully damped out as it is observed in Figures 6.16 and 6.17 which proves that correct selection of the frequency of perturbation is key for damping out unnecessary 2<sup>nd</sup> order fluctuations. The current flows through the inductance within a similar shape to the waveform in the case of constant input voltage of the continuous conduction mode of the boost converter. Due to the algorithm of PO, there is a continuous search for MPP in which the peak to peak PV voltage fluctuations reached 3.5 %. The PV output current and grid current are shown in Figure 6.16, and Figure 6.18 respectively. The PV current has the envelope similar to the inductance current switched at 10 kHz and the grid current is sinusoidal at grid frequency. It takes 50 ms of time to arrive from the zero level of PV output power to the steady-state level with PO MPPT search algorithm finding MPP as seen in Figure 6.19. Even at steady state operation small fluctuations still exist since the duty cycle is constantly being altered which is considered a huge drawback for grid tied PV arrays.

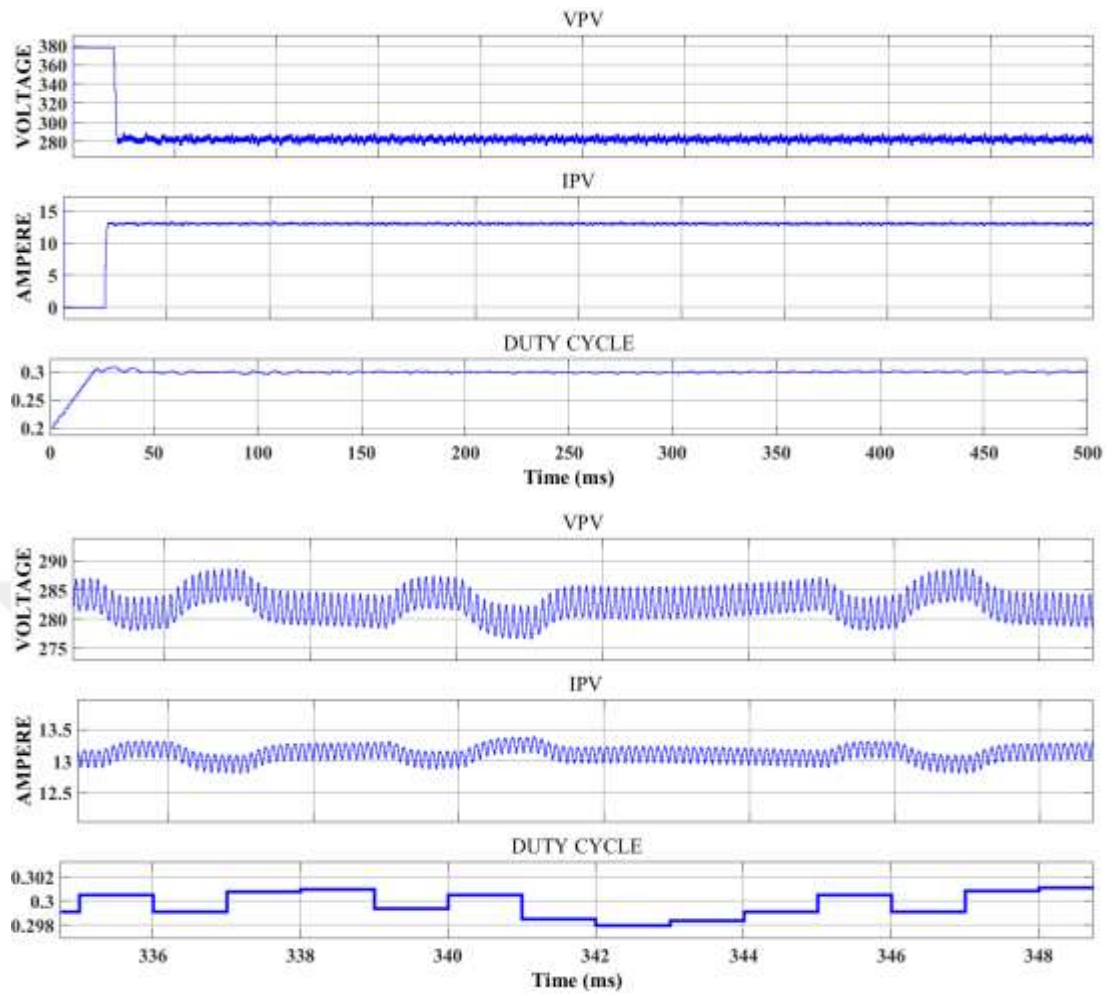


Figure 6.16 PV array voltage and current output waveforms



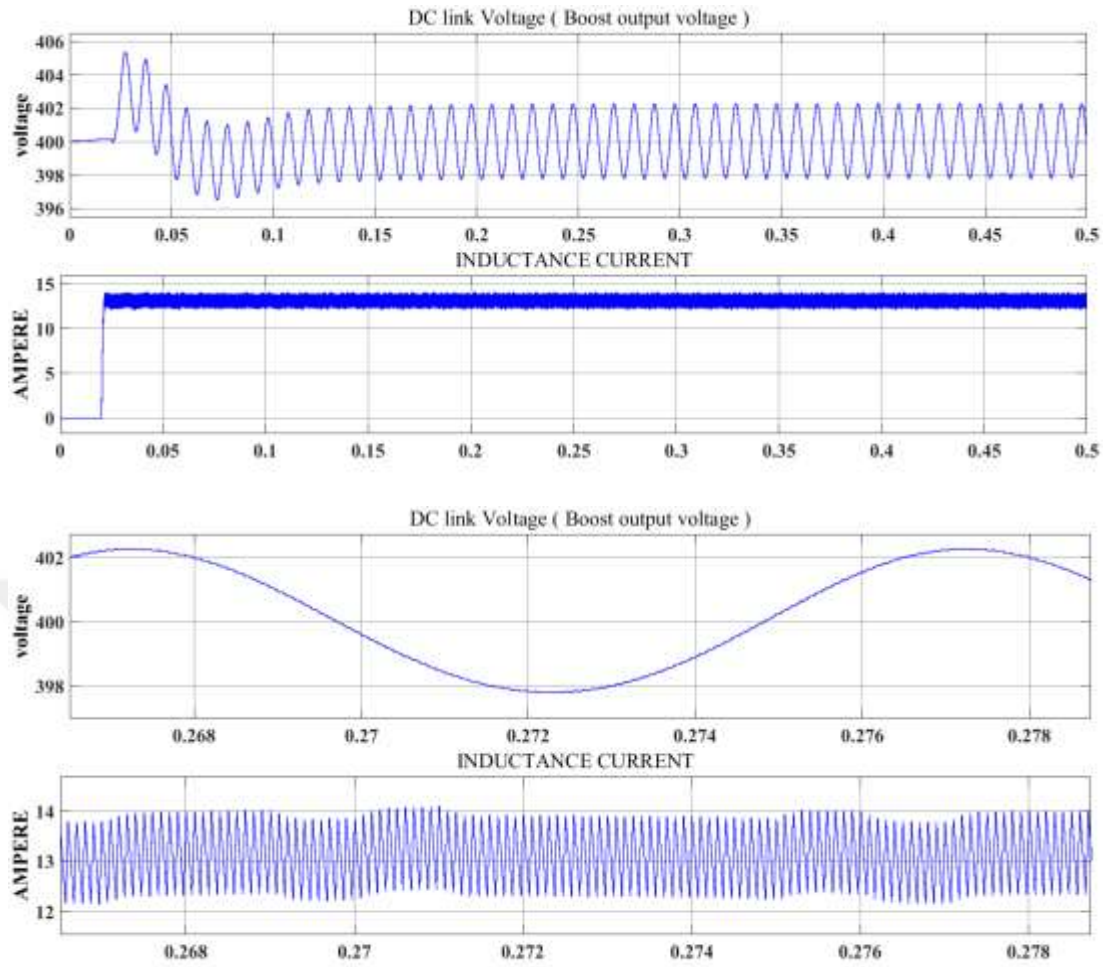


Figure 6.17 Boost voltage and inductance current output waveforms

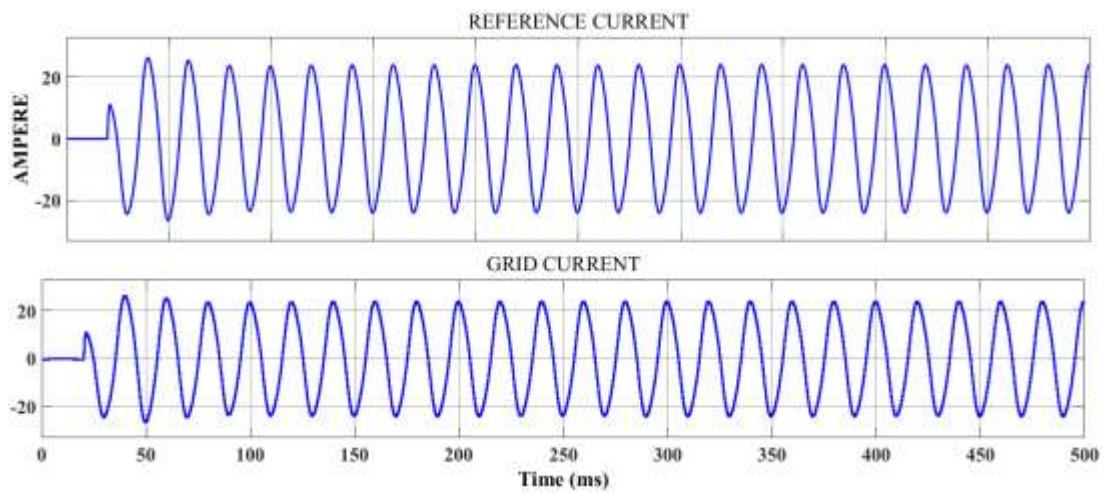


Figure 6.18 Grid current output waveform

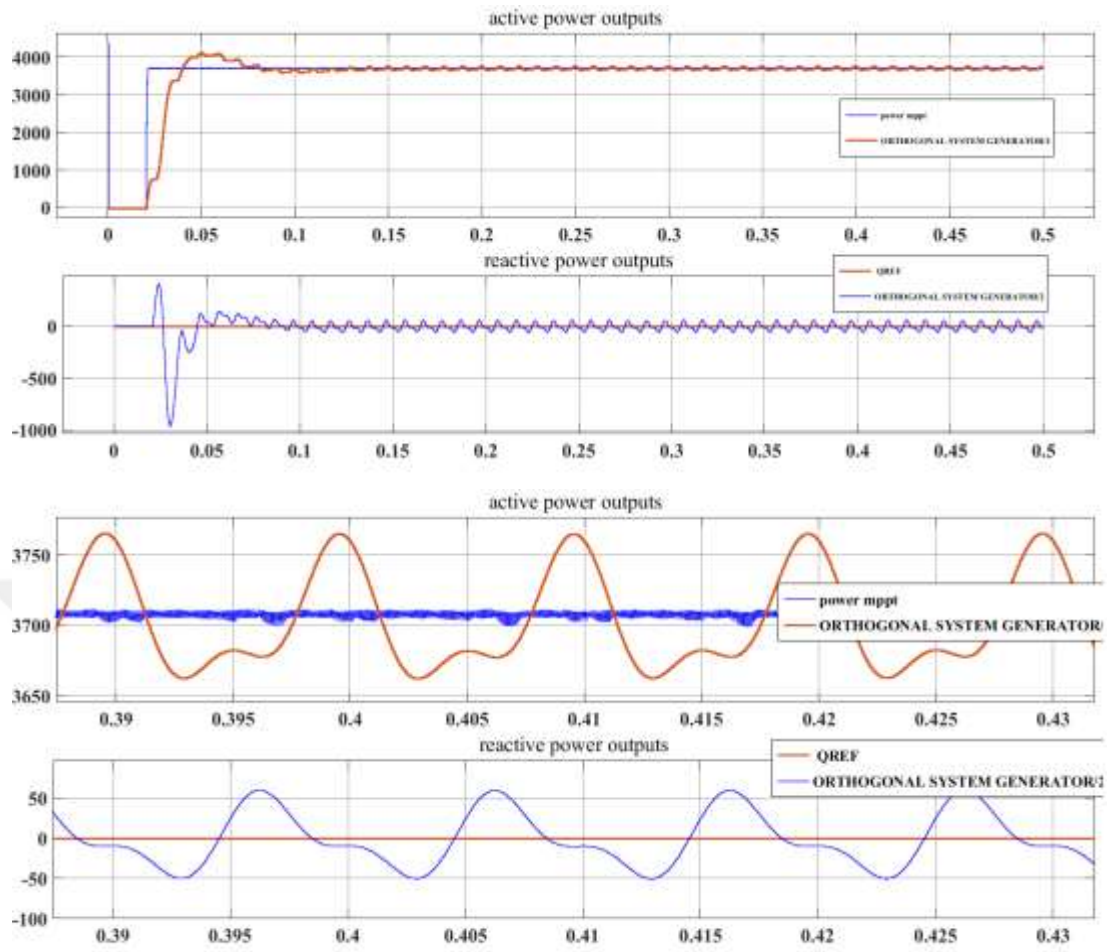


Figure 6.19 Real output power of inverter connected to grid

### ***6.2.2 Duty Cycle Based Particle Swarm Optimization***

The duty cycle of the boost converter is disturbed at 1000 Hz. It takes 50 ms of time to arrive from the zero level of PV output power to the steady-state level under PSO algorithm as it is shown in Figure 6.22. The PSO is finding the maximum power point at close rate to that of the PO algorithm. The voltage ripples are smaller than those of the conventional PO method applied during the search of MPP. Considering the frequency of its operation which is 1000 Hz, the PSO gives relatively low steady state error on the real power as shown in Figure 6.23 with severe power fluctuations during transient time intervals. It is worth noting with the PSO modulation neither steady state error nor 2<sup>nd</sup> order fluctuations exist on both the voltage and current outputs of the PV array, and of the boost converter as seen in Figures 6.20 and 6.21. The grid current following the reference current obtained from the control system is shown in Figure 6.24.

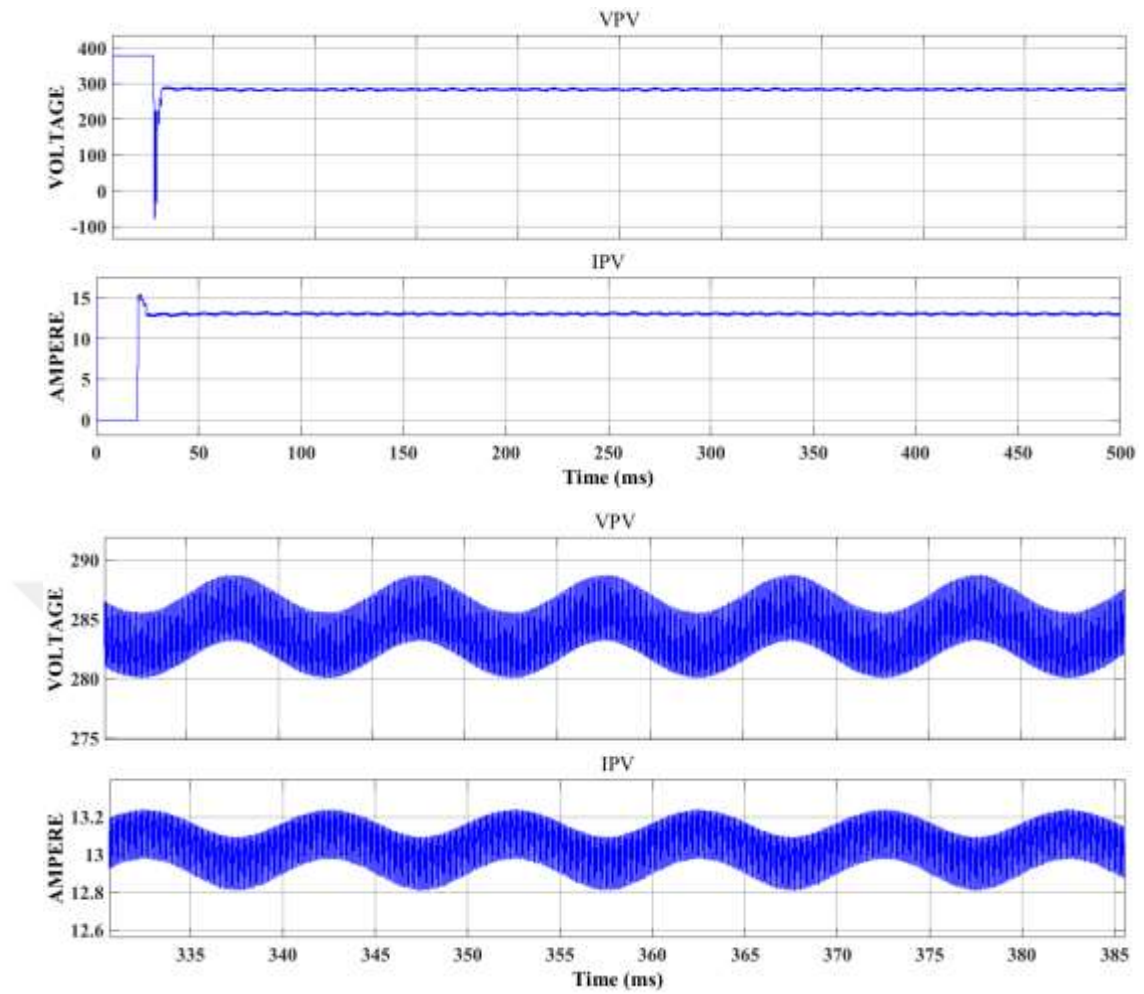


Figure 6.20 PV array voltage and current output waveforms

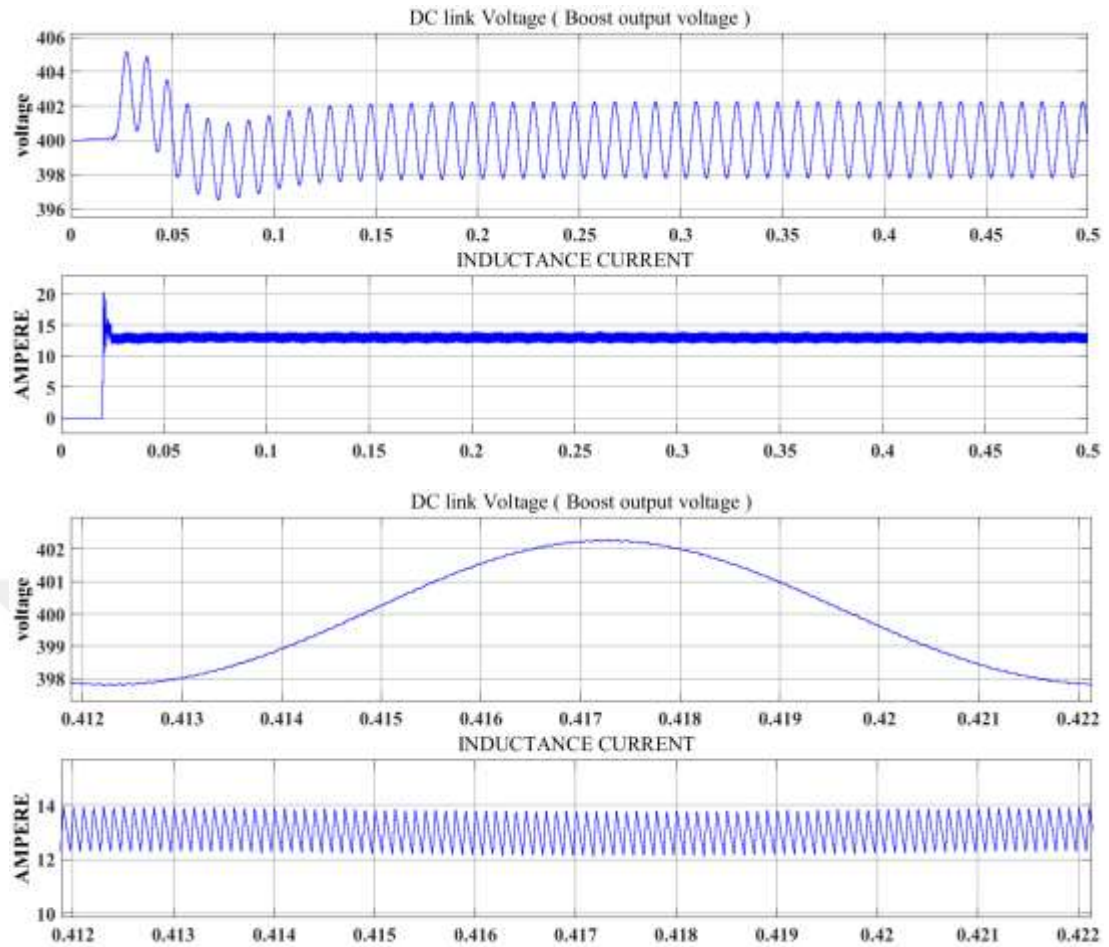


Figure 6.21 Boost voltage and inductance current output waveform

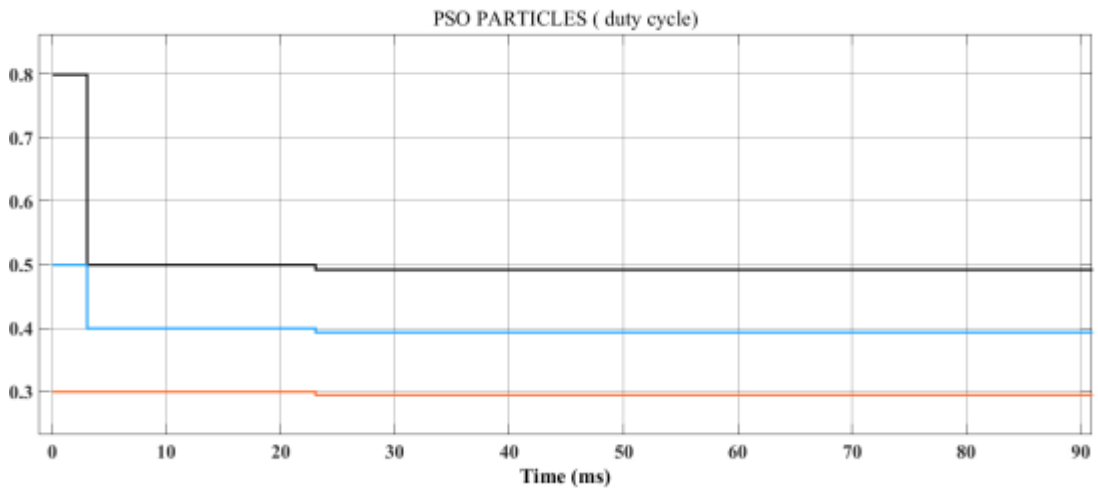


Figure 6.22 Particle Swarm Particles w.r.t time

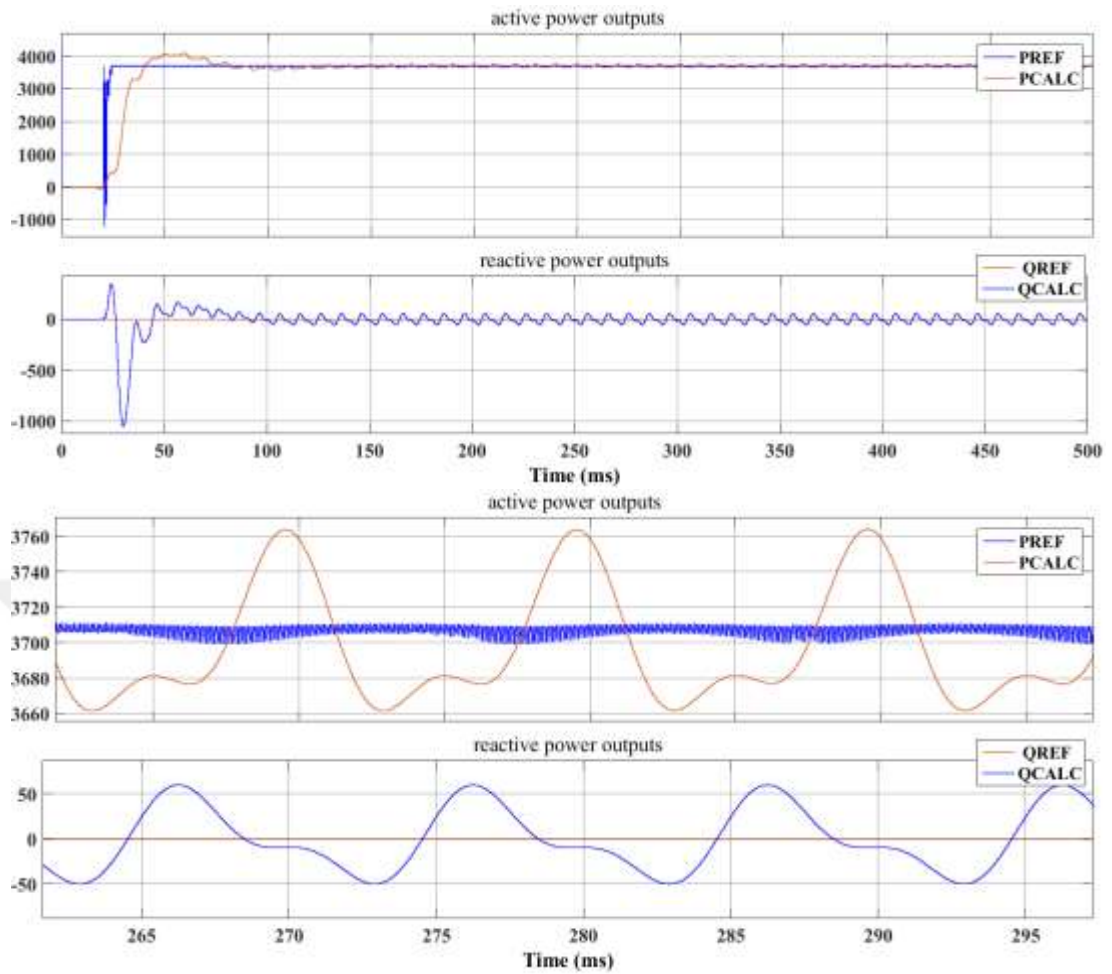


Figure 6.23 Real output power of inverter connected to grid

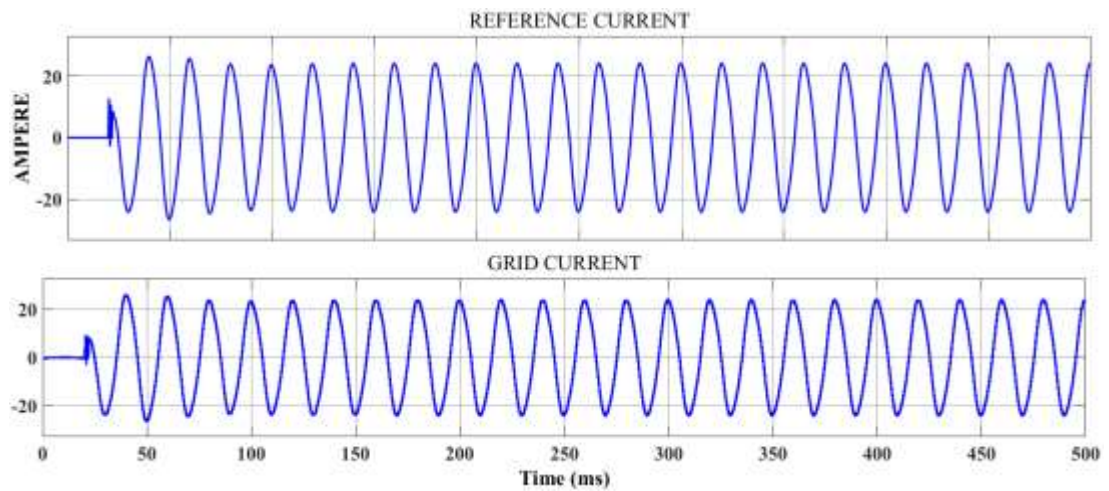


Figure 6.24 Grid current output waveform



### ***6.2.3 Voltage Oriented Perturb and Observe Based Predictive Valley Current Control***

The predictive current controller is used for the inductance current control and the MPP of the PV array is searched by disturbing the PV output voltage. In this simulation the control technique utilizes the perturbation of the voltage of  $V_{pv}$  to successfully track the MPP in which the output voltage is used to find the reference current  $I_{ref}$  for the predictive control as discussed earlier in Chapter 5. The steady state error and 2<sup>nd</sup> order fluctuations cease to exist on both the voltage, and current outputs of the PV array as well as the voltage and current output waveforms of the boost converter as shown in Figures 6.25 and 6.26. The perturbation is carried out at 1000 Hz with the voltage reference obtained as shown in Figure 6.27. The predictive valley current control of the inductance current generates the duty cycle under the reference current obtained at the MPP from the PI controller operation between the PV output voltage and the voltage oriented duty cycle. The output voltage of the boost converter which is the input voltage of the inverter is controlled by the DC link voltage controller of the inverter. The operation of the system at the MPP is stable but the voltage and current fluctuations at steady state are larger. However, it takes 6 ms of time to arrive from the zero level of PV output power to the steady-state level under this search algorithm which has relatively faster response than that of the conventional PO, and PSO as shown in Figure 6.28. The PI controller constants for the voltage oriented MPPT are  $K_P=0.2$ , and  $K_I=10$ .

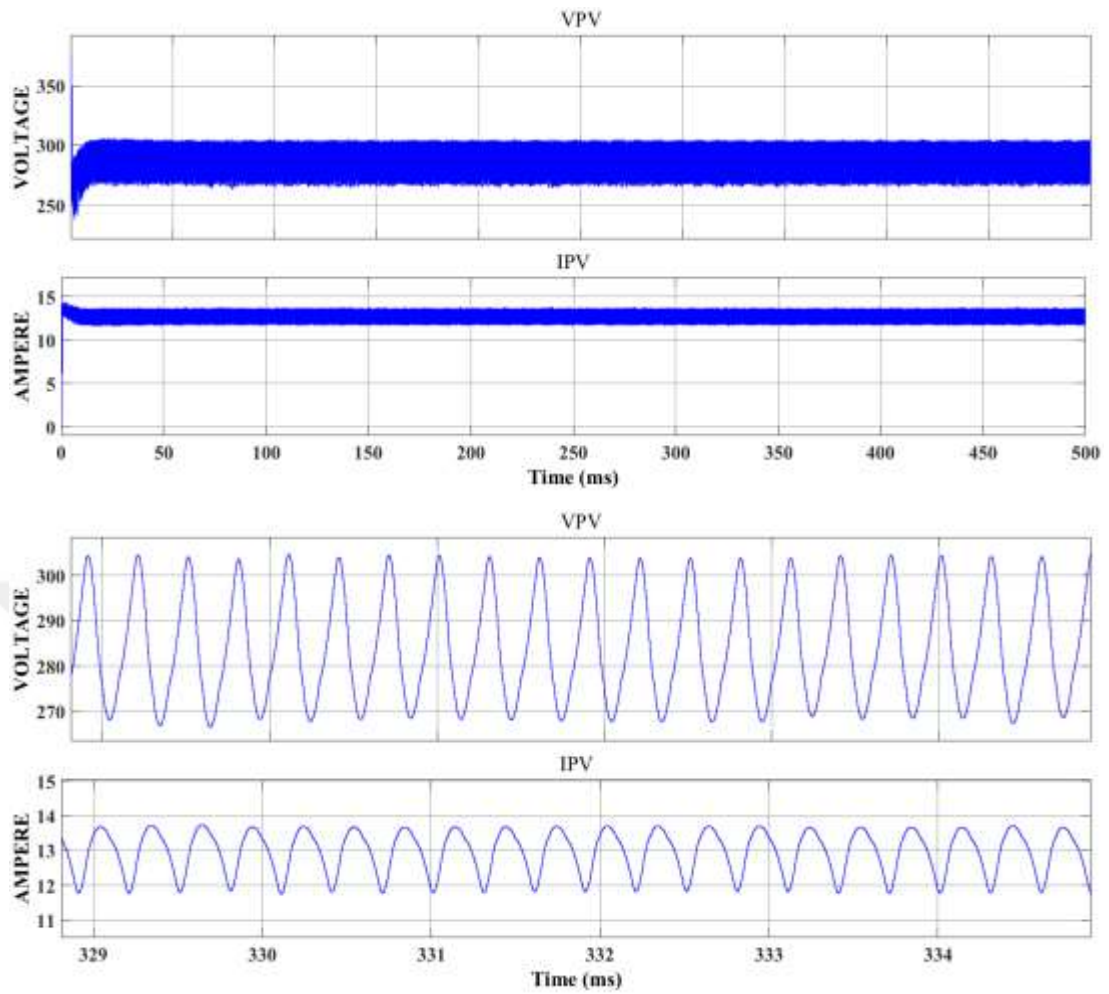


Figure 6.25 PV array voltage and current output waveforms



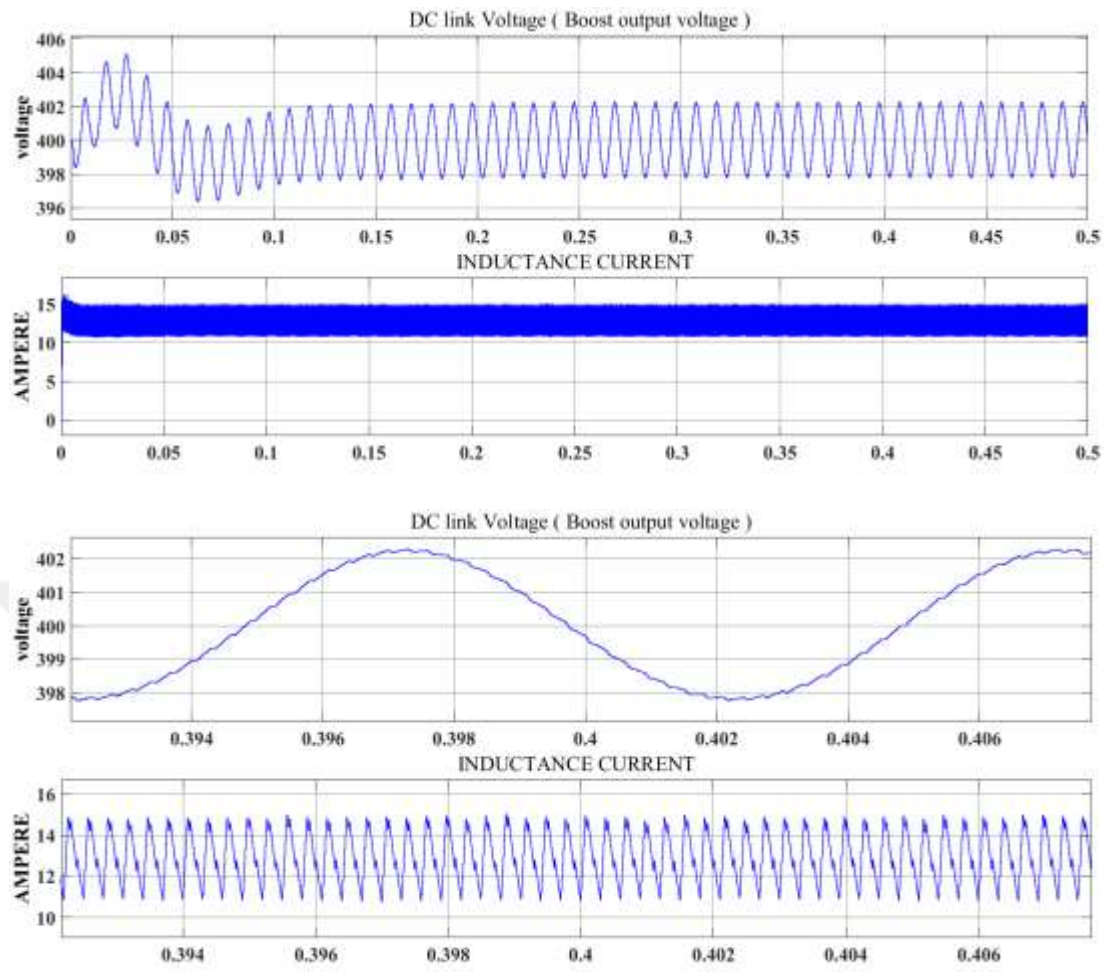


Figure 6.26 Boost voltage and inductance current output waveforms

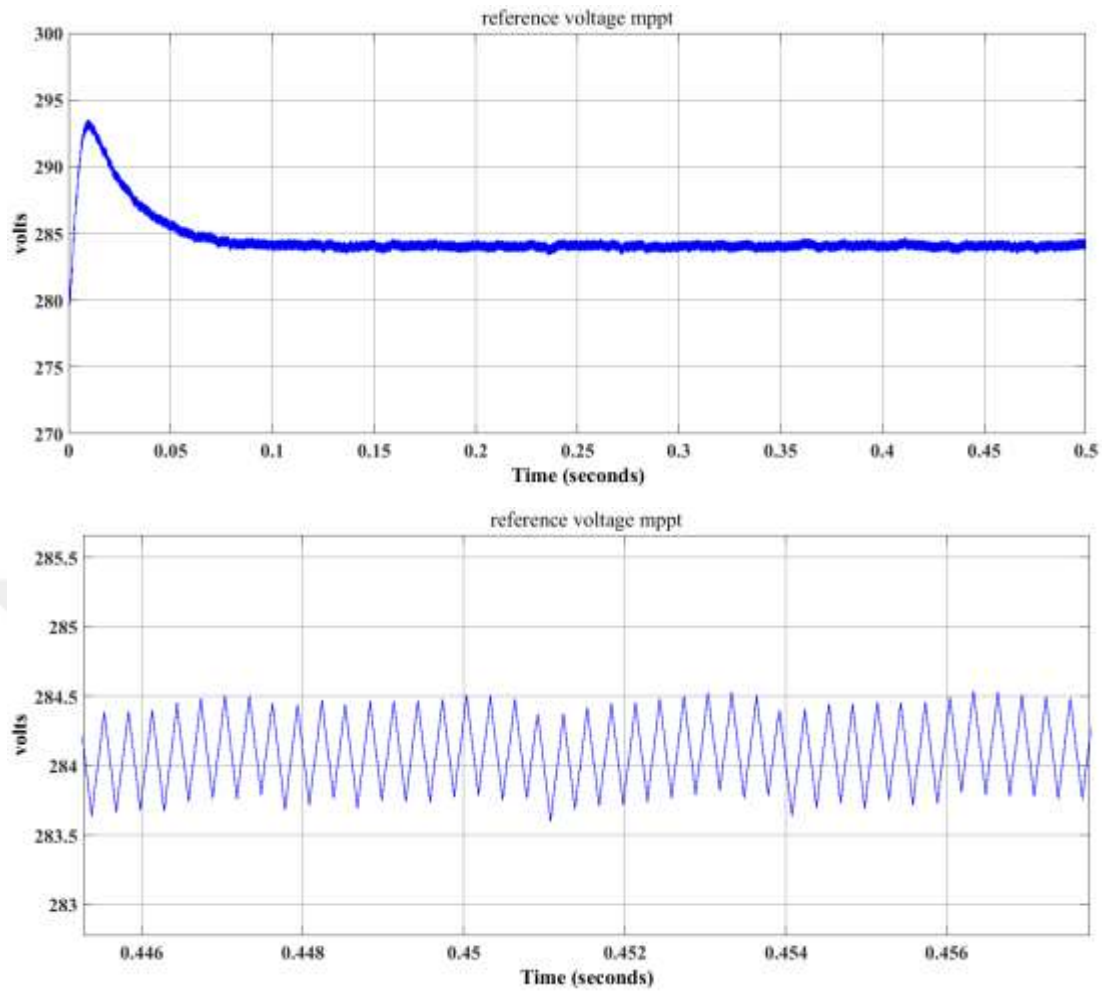


Figure 6.27 Predictive valley current control voltage reference output waveform (MPPT)

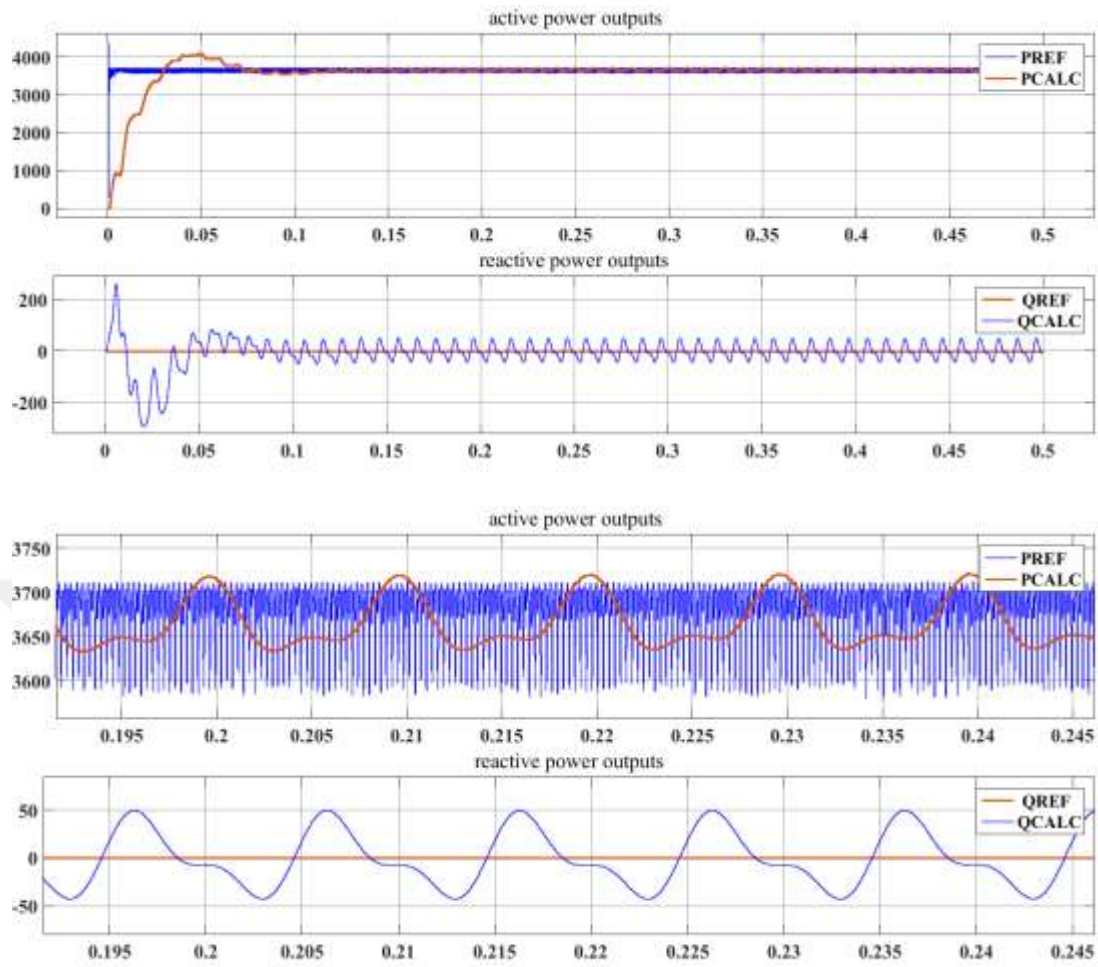


Figure 6.28 Output real power of inverter connected to grid

#### ***6.2.4 Voltage Oriented PSO Based Predictive Valley Current Control***

The fluctuations on the output voltage and current of the PV array are kept almost same as seen in Figure 6.29. In addition, both voltage and current outputs of the boost converter are approximately constant without any 2<sup>nd</sup> order fluctuations that are occurring at steady state as shown in Figure 6.30. It takes 4 ms of time to arrive from the zero level of PV output power to the steady-state level under this search algorithm as shown in Figure 6.31 in which 0.02 ms of time is needed to find MPP. This methodology has successfully reached the MPP at steady state with peak to peak power fluctuations reaching 2.7%. The perturbation is applied at 1000 Hz as shown in Figure 6.32. The real power is being delivered with minimum fluctuations in the process. It is significantly less than the response time of the conventional PO, and PSO method applied. The PI controller constants for the voltage oriented MPPT are  $K_P=0.4$ , and  $K_I=0.2$ .

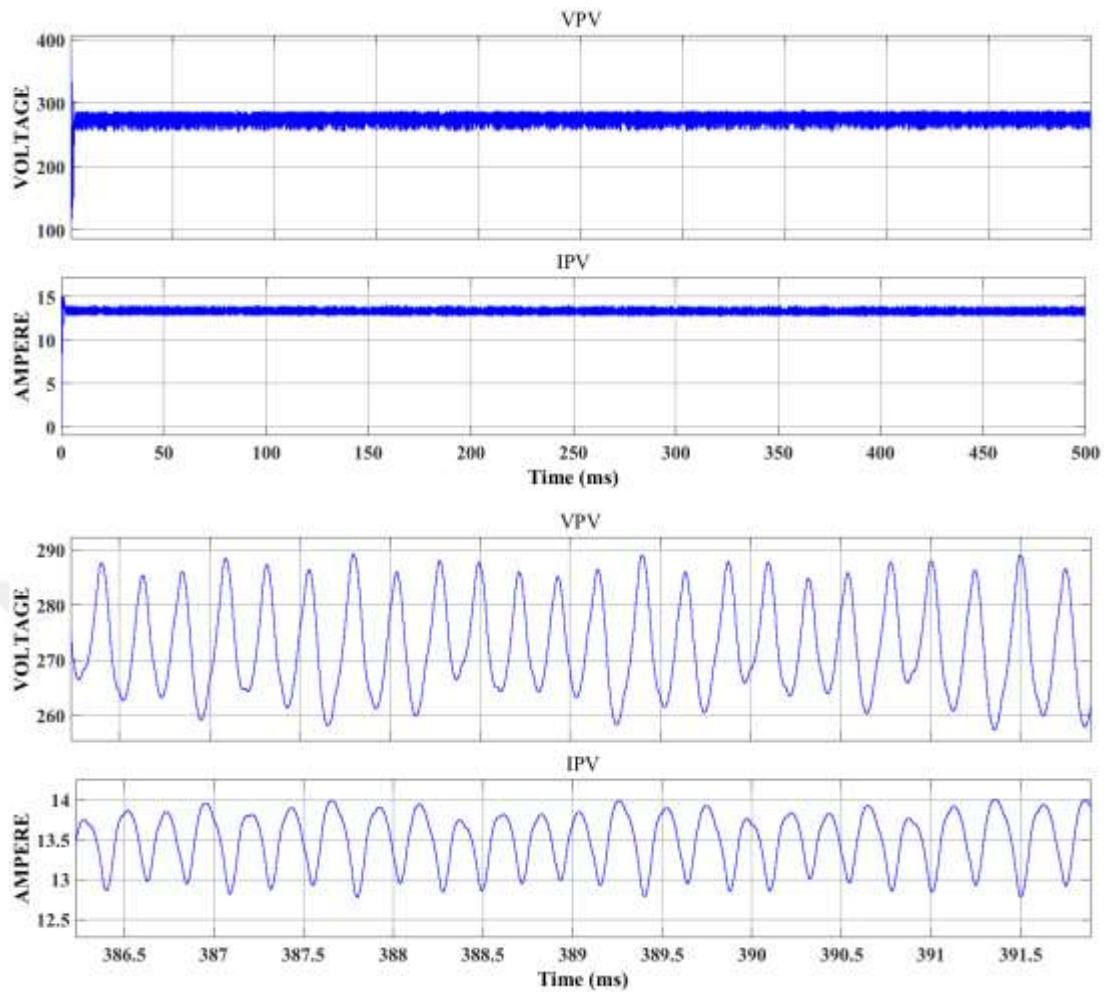


Figure 6.29 PV array voltage and current output waveform

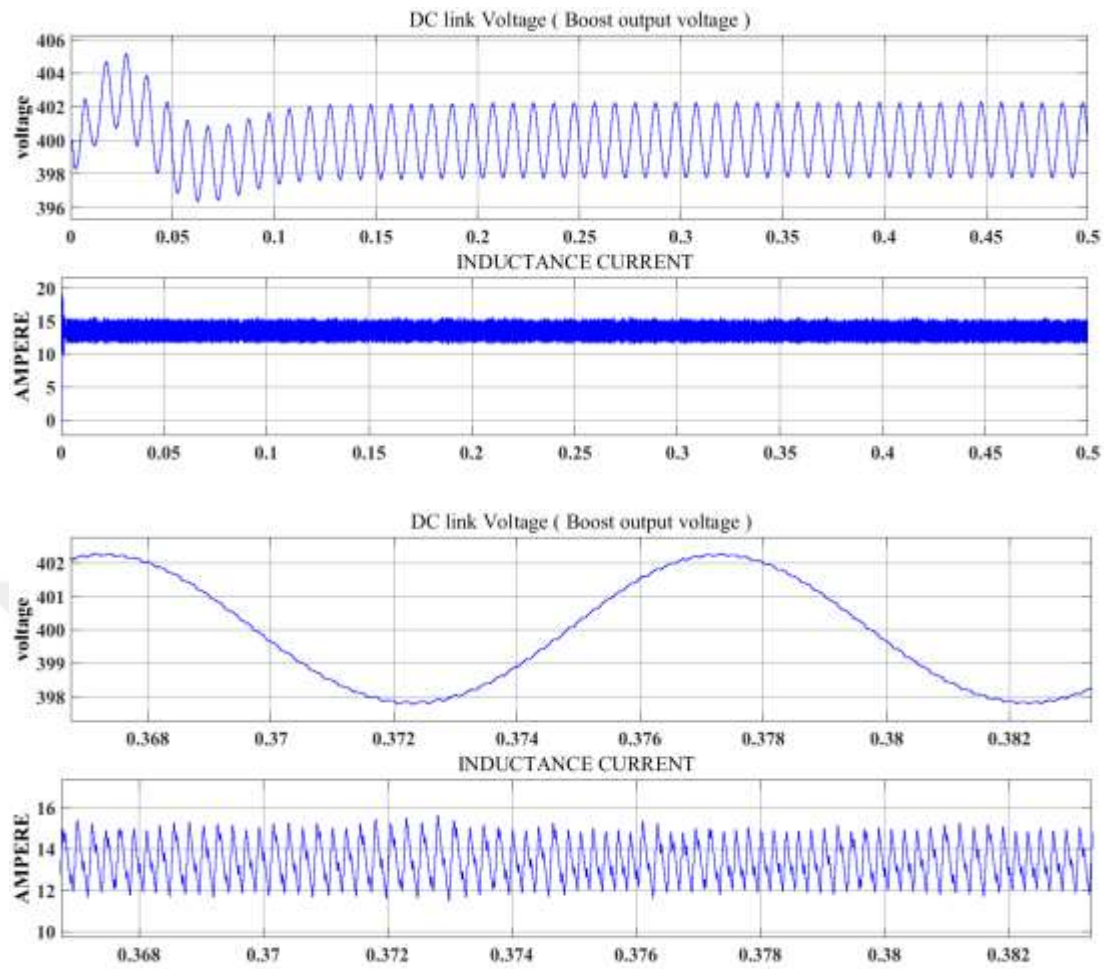


Figure 6.30 Boost voltage and inductance current output waveforms

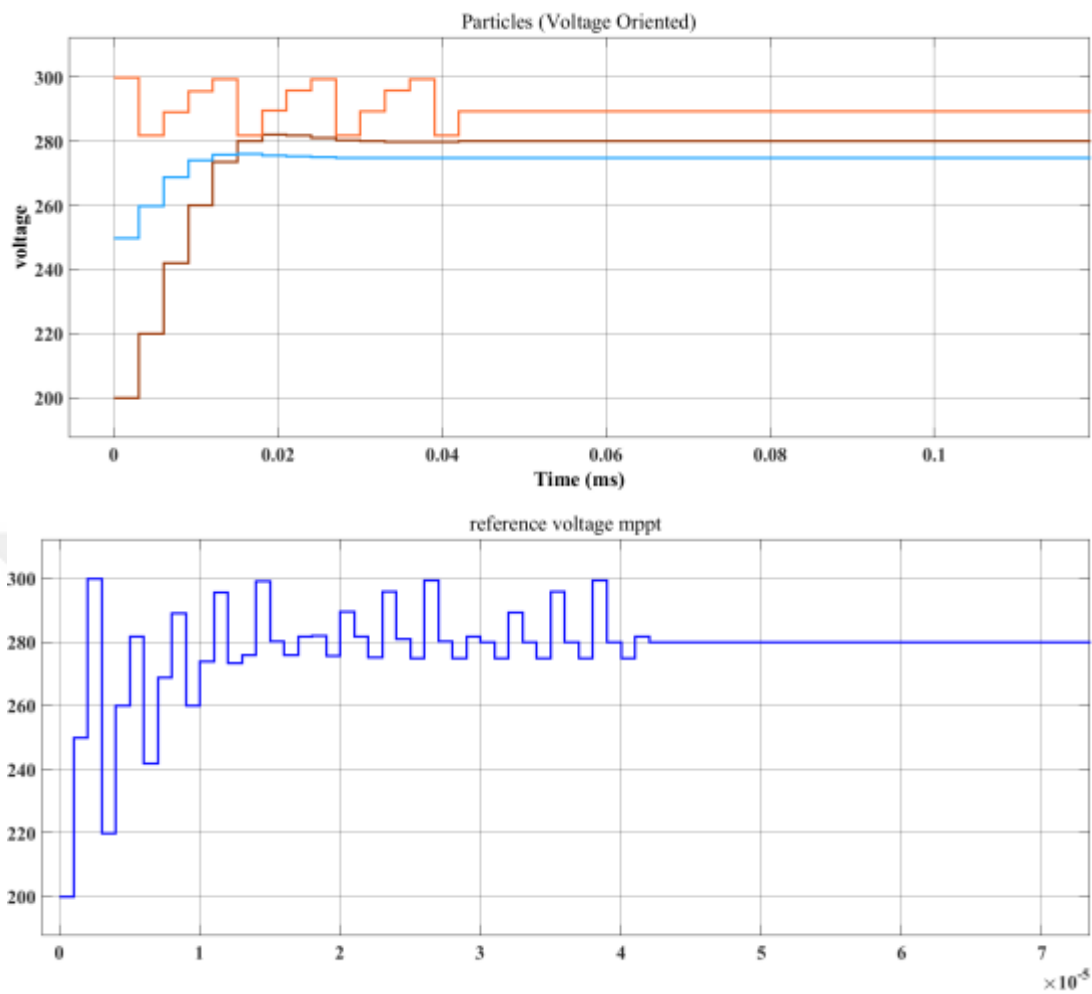


Figure 6.31 Particle Swarm Particles w.r.t time



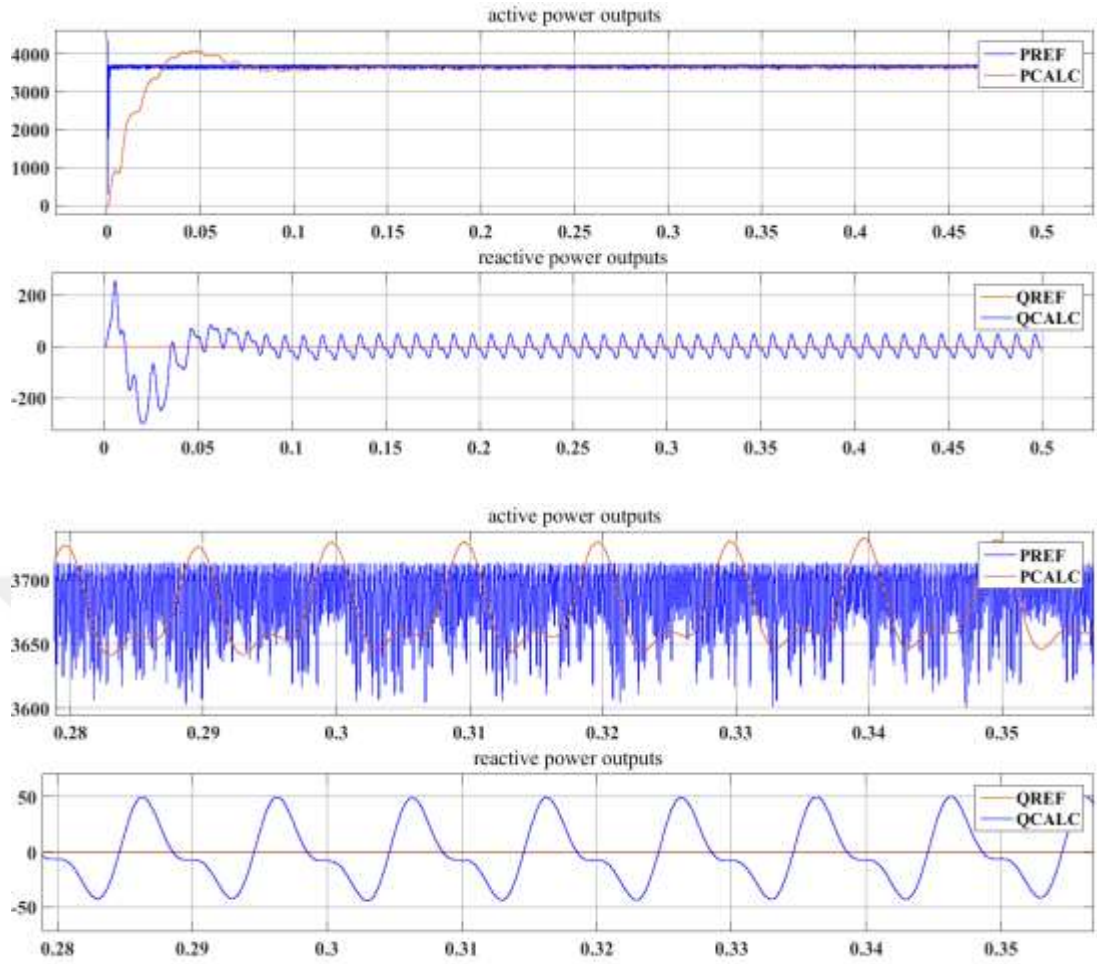


Figure 6.32 Output real power of inverter connected to grid

### 6.2.5 Voltage Oriented PO Based Predictive Average Current Control

The average based predictive current control is similar to the working of the valley based predictive current control in which both are used for the control of the inductance current. The only difference between them as mentioned in chapter 2, and 5 is that the average based predictive current control utilizes equation 2.24 to control the average current of the inductance current  $I_L$  hence the reference for the system will be the average value and not the valley. The fluctuations cease to exist on both the voltage, and current outputs of the PV array and of that of the inductance current and boost's output voltage as seen in Figures 6.33, and 6.34.

The reference voltage output of the voltage oriented MPPT PO algorithm is shown in Figure 6.35 in which a constant voltage is reached. As seen in Figure 6.36 the methodology is slow to track down and lock MPP in which it takes 115 ms of time to



arrive from the zero level of PV output power to the steady-state level taking into consideration the 20 ms delay applied. However, it is worth noting that this methodology yields also to very small steady state power fluctuations in which these fluctuations are smaller than all the above mentioned methodologies as seen in all the figures observed below. The PI controller constants for the voltage oriented MPPT are  $K_p=3$ , and  $K_i=0.7$ .

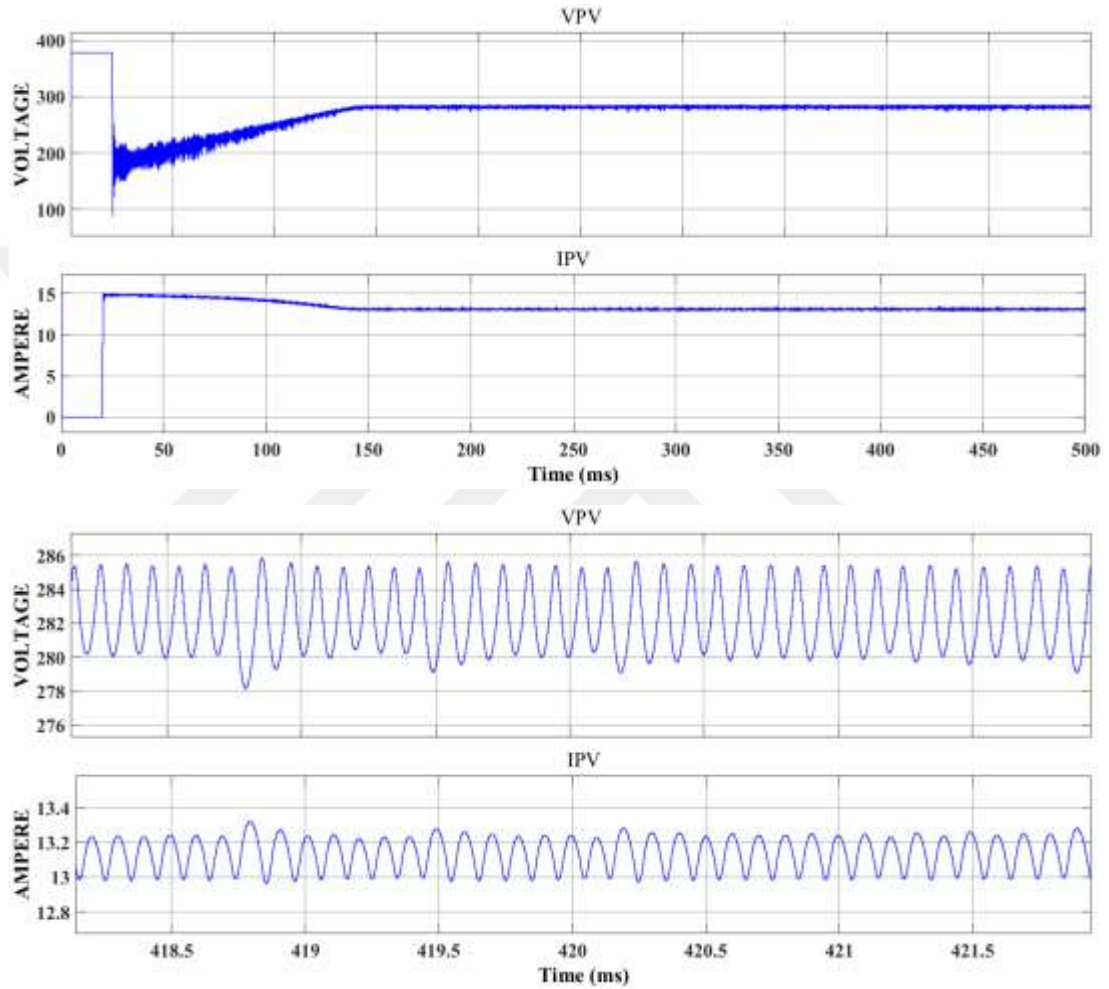


Figure 6.33 PV array voltage and current output waveforms

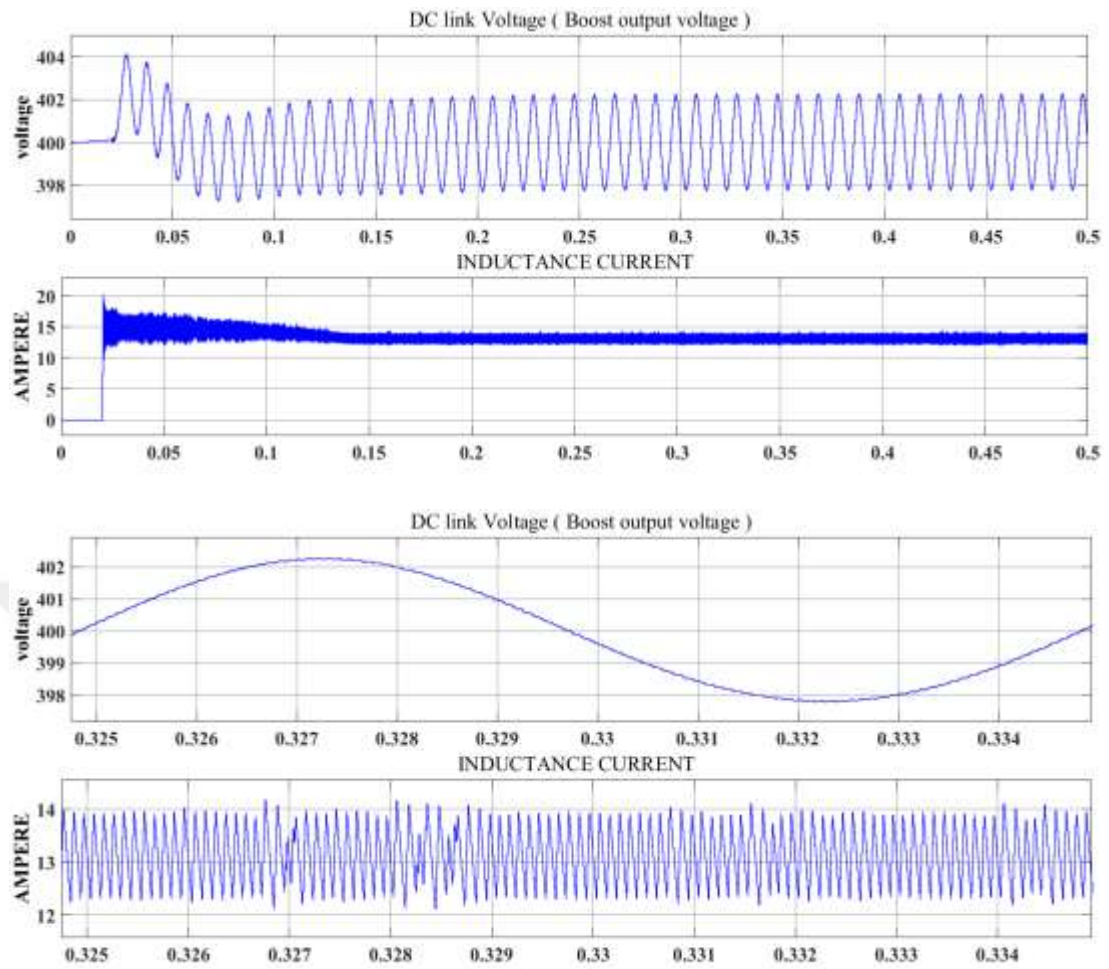


Figure 6.34 Boost voltage and inductance current output waveforms

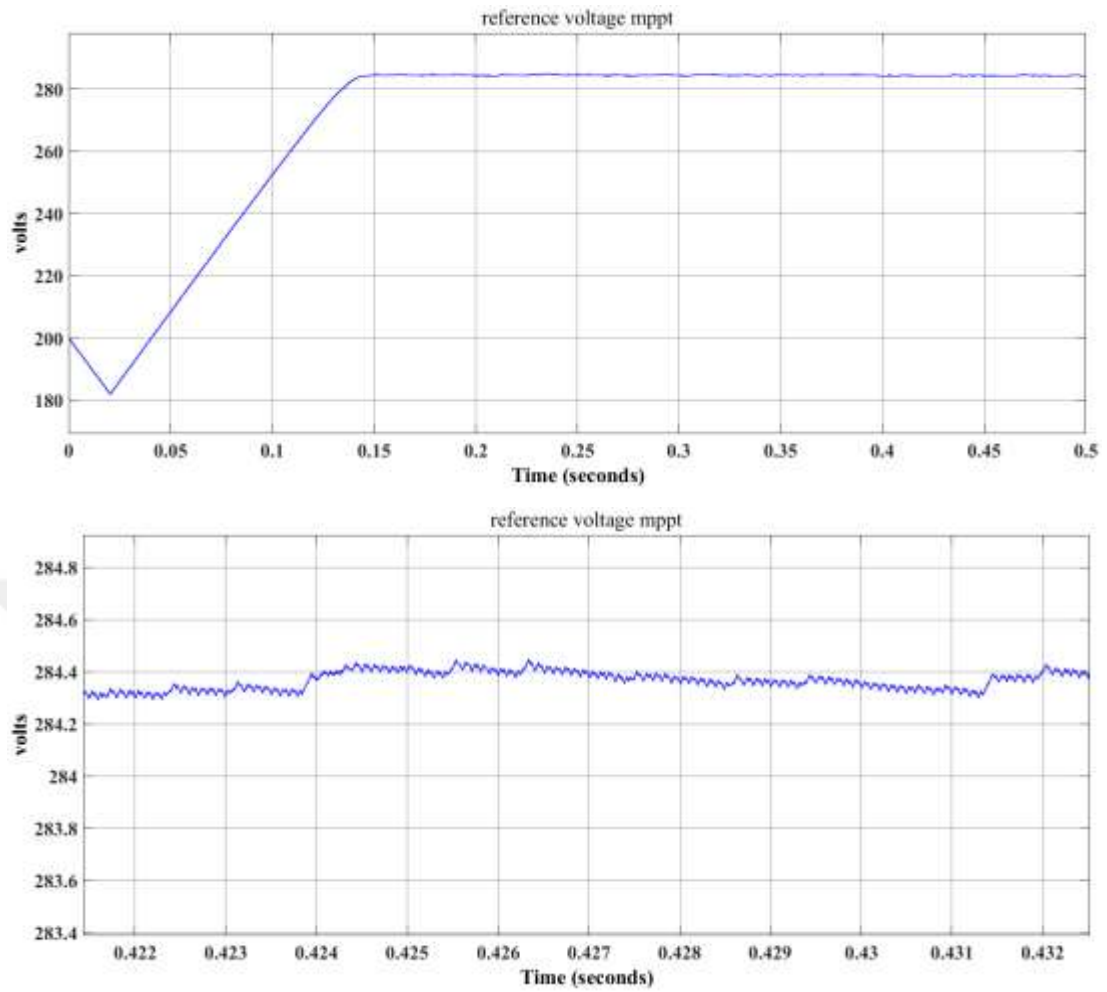


Figure 6.35 Predictive valley current control voltage reference output waveform (PO MPPT)

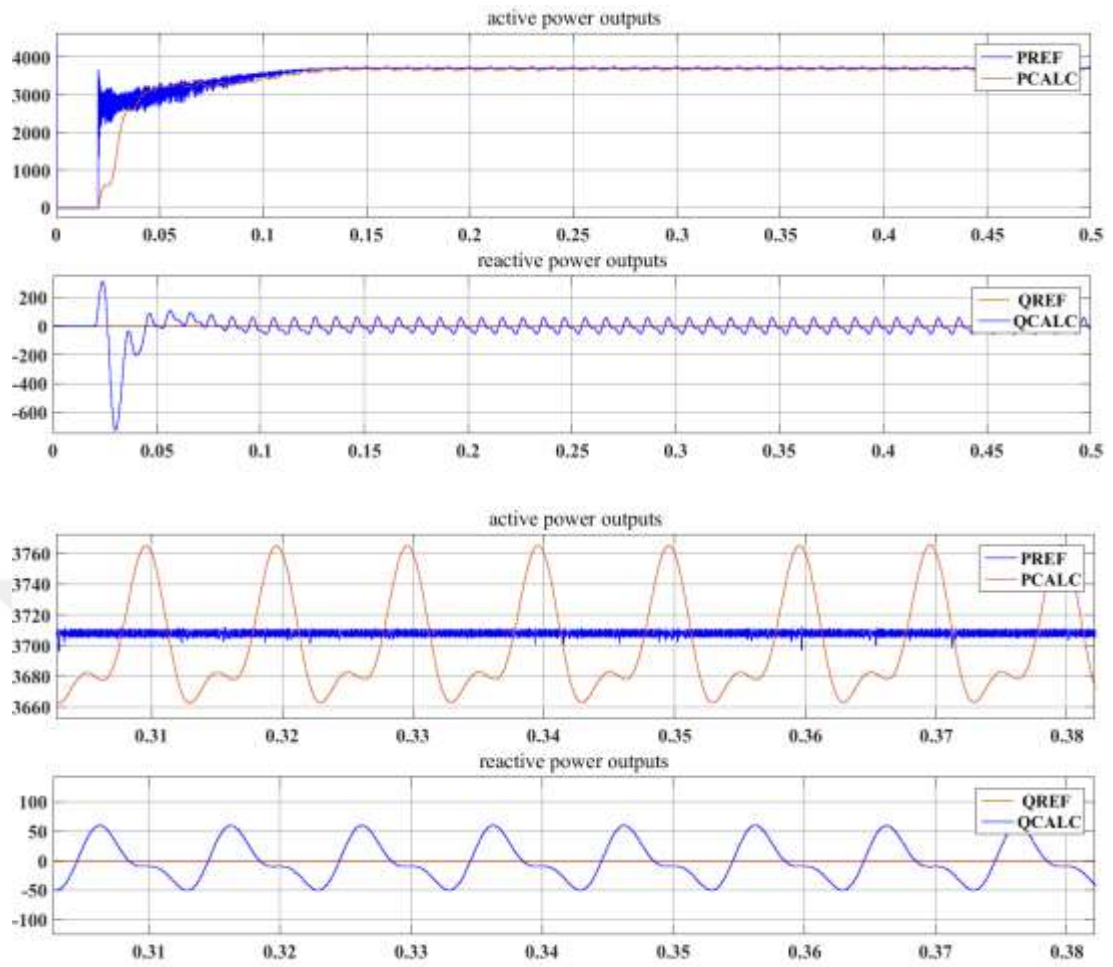


Figure 6.36 Output real power of inverter connected to grid

### ***6.2.6 Voltage Oriented PSO Based Predictive Average Current Control***

The fluctuations on the output voltage and current of the PV array are kept almost same as seen in Figure 6.37. The fluctuations cease to exist on the inductance current and the output voltage of the boost converter as seen in Figure 6.38. PSO was able to obtain the MPP voltage point in under 0.05 ms as shown in Figure 6.39. This methodology has successfully reached the MPP with 0.7 % peak to peak power fluctuations whereas the perturbation is applied at 1000 Hz as shown in Figure 6.40. It takes 1 ms of time to arrive from the zero level of PV output power to the steady-state level under this search algorithm as shown in Figure 6.40. It is significantly less than the response time of the voltage oriented PO valley predictive control method applied as well. The PI controller constants for the voltage oriented MPPT are  $K_P=3$ , and  $K_I=0.7$ .

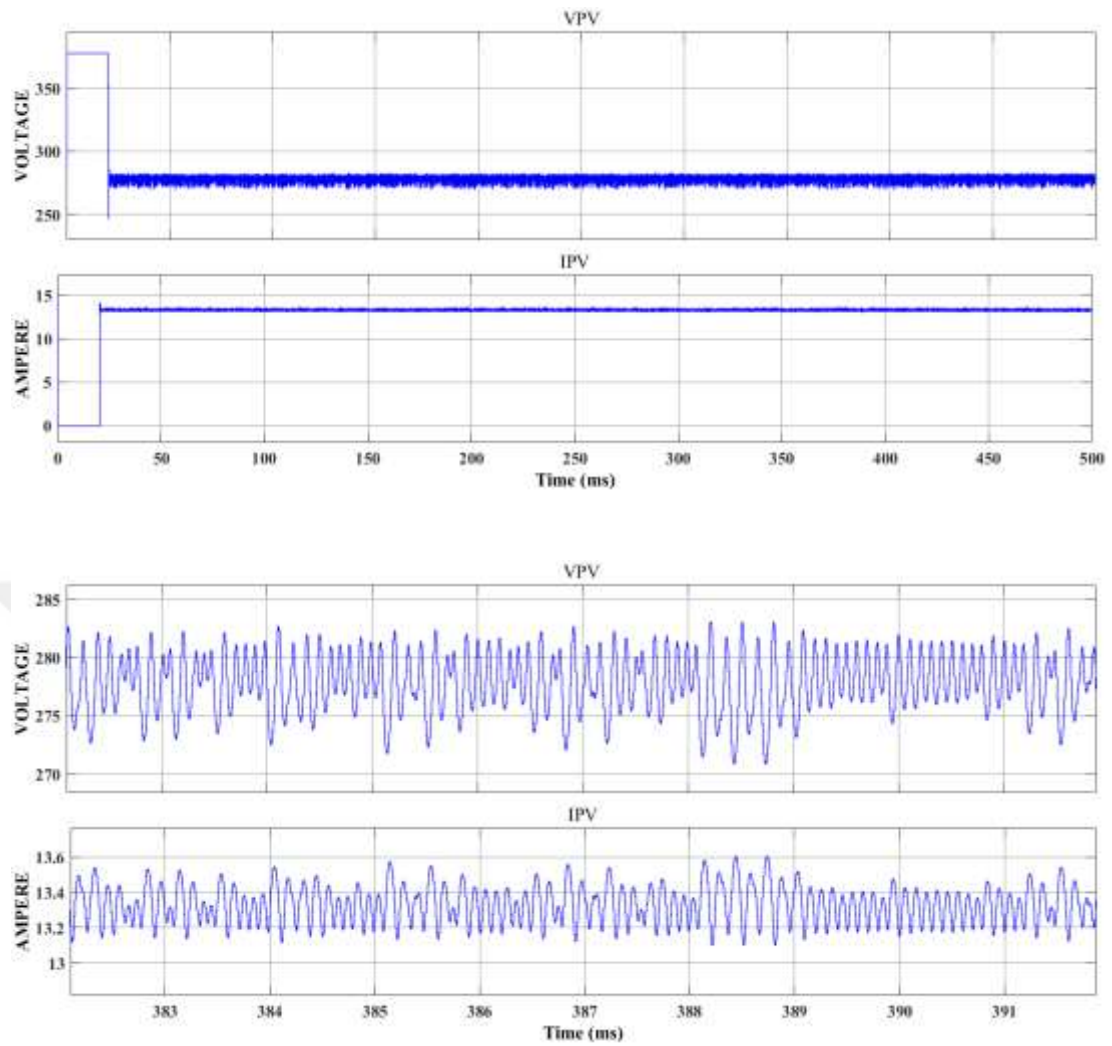


Figure 6.37 PV array voltage and current output waveform

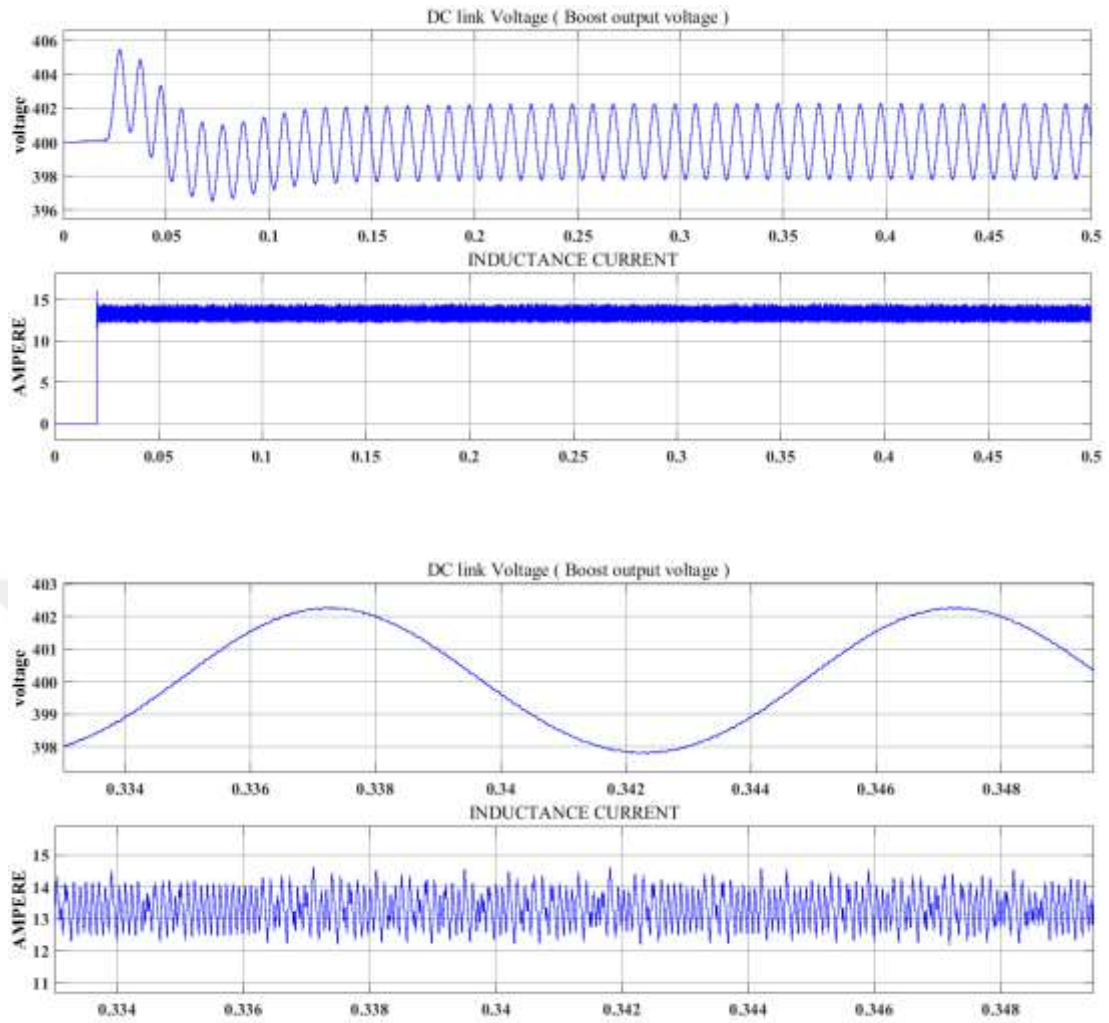


Figure 6.38 Boost voltage and inductance current output waveforms

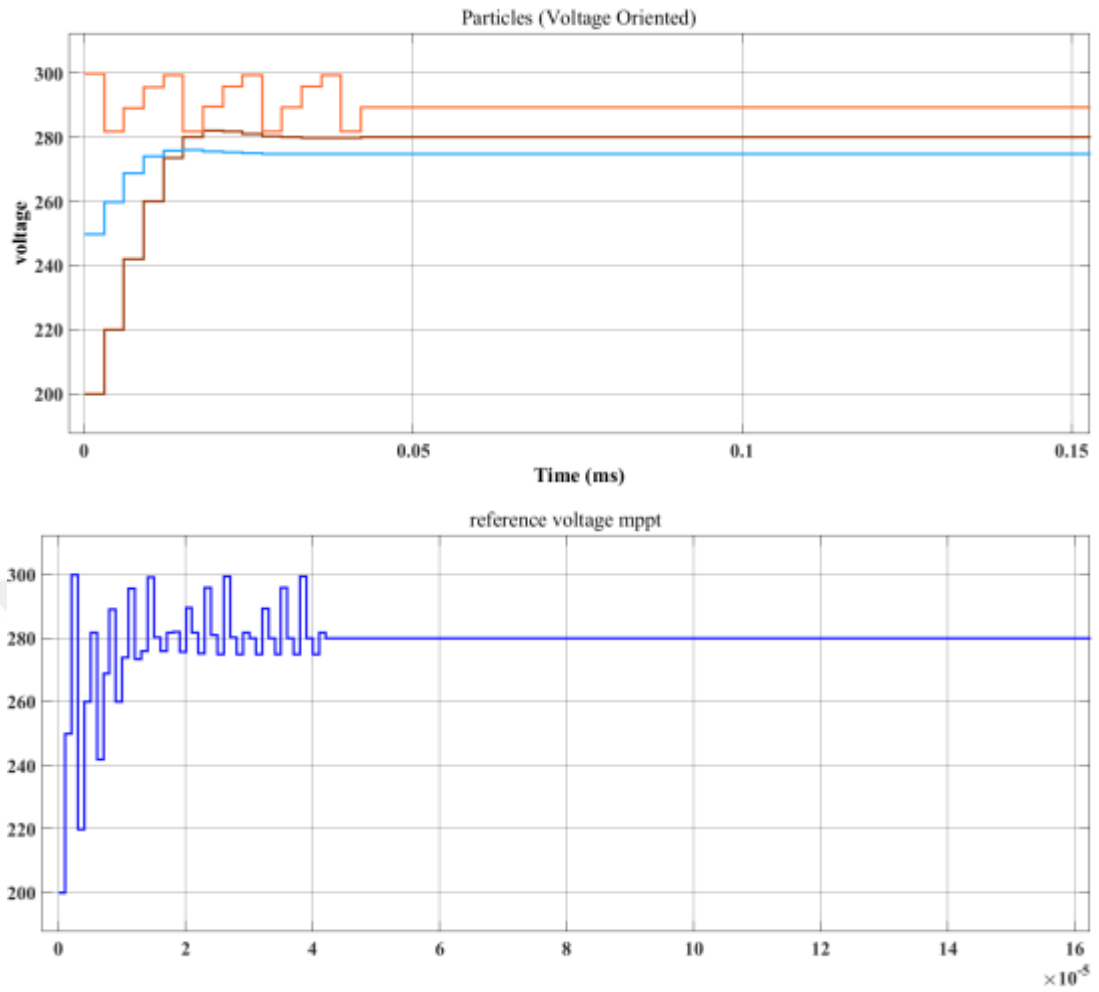


Figure 6.39 PSO Particles and reference voltage output w.r.t time



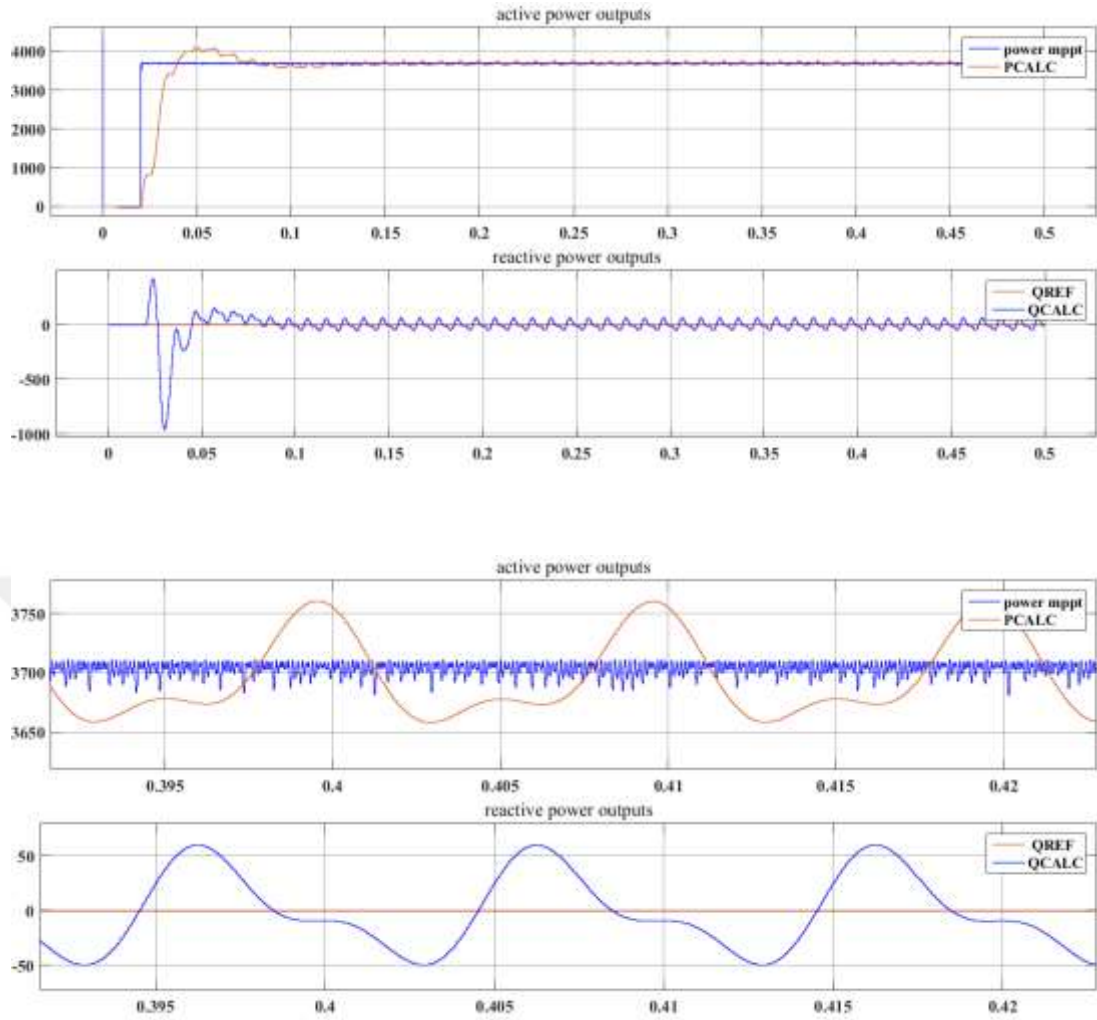


Figure 6.40 Output real power of inverter connected to grid

Table 6.2 Summary of the results obtained

Method	Settling time	Steady state reference power fluctuations %	Voltage $V_{pv}$ peak to peak fluctuations %
Duty Cycle Based Perturb and Observe	50 ms	0.27	3.5
Duty Cycle Based Particle Swarm Optimization	50 ms	0.4	2.8
Voltage Oriented Perturb and Observe Based Predictive Valley Current Control	6 ms	2.97	11.93
Voltage Oriented PSO Based Predictive Valley Current Control	4 ms	2.83	11.27
Voltage Oriented Perturb and Observe Based Predictive Average Current Control	115 ms	0.13	2.83
Voltage Oriented PSO Based Predictive Average Current Control	1 ms	0.7	3.5

## **CHAPTER SEVEN**

### **CONCLUSIONS**

In this thesis, a study involving grid tied PV array is conducted in which the PV array is directly connected to a boost converter with various MPPT methodologies adopted and simulated as such to be able to compare these methodologies between one another. In addition, the boost converter is directly connected to the grid tied three level inverter in which OSG control topology has been adopted. Furthermore, the boost converter is driven by predictive current control. All simulations are conducted within the MATLAB/SIMULINK environment.

The use of neutral clamped three level inverter is convenient for grid tied two stage PV arrays in which the common mode voltage is kept constant which is considered an advantage. The PR controller successfully forced the grid current to follow the reference current produced by the OSG control system. With the help of PI, and PR controllers, the power reference acquired from the PV array was successfully tracked and controlled with minimum oscillations in which overshoot does not exceed 5 %.

The conventional MPPT perturb and observe methodology gives unnecessary fluctuations in voltage and current output waveforms due to the constant search for MPP which is shown in the duty cycle distortion. However, the fluctuations due to the natural response of the boost converter as discussed in Chapter 3 has been successfully avoided with the correct selection of MPPT steps. The PSO needs high frequency to reach zero percentage steady state power fluctuations. In addition the PSO creates power oscillations to the grid in the process of acquiring of the MPP. The MPPT system creates the reference real power for the grid connected inverter, and the OSG control creates the reference current successfully for the grid current to follow.

The fast robust characteristics of the PSO, with the precision of the predictive current control, it can be deduced that the hybrid methodology is the optimum option for grid tied two stage PV arrays. In addition, settling time taken to reach steady state power is reduced dramatically by the PSO method. It is worth noting that for PV grid

connected application, the voltage oriented PSO based predictive average current control gave best results in simulations. It should be taken into consideration that this methodology has low settling time value and with its precision and low voltage fluctuations on  $V_{pv}$  from which it can be considered a suitable choice. Also the PI controller gains of the voltage oriented MPPT system greatly affects the system's transient response. The optimum choice of controller gains for the best transient response is considered as the future work of this study.



## REFERENCES:

- Bryant B, & Kazimierczuk M (2004) .Small-signal duty cycle to inductor current transfer function for boost PWM DC-DC converter in continuous conduction mode. *IEEE International Symposium on Circuits and Systems I*, 5, 856-857
- Bryant B, & Kazimierczuk M (2005). Open-loop power-stage transfer functions relevant to current-mode control of boost PWM converter operating in CCM. *IEEE Transactions on Circuits and Systems I*, 52, 2158–2164.
- Chen J, Prodic A, Erickson R, & Maksimovic D (2003). Predictive digital current programmed control. *IEEE Transactions on Power Electronics*, 18, 411–419.
- Durbaba E, (2018). *PV system connected to grid through dc/dc buck- boost converter and dc/ac unipolar switching inverter*. M.Sc. thesis, Dokuz Eylül University, Izmir.
- Hart, D. (2011). *Power electronics*. New York: McGraw-Hill.
- Enrique J, Durán E, Sidrach-De-Cardona M, & Andújar J (2007). Theoretical assessment of the maximum power point tracking efficiency of photovoltaic facilities with different converter topologies. *Solar Energy*, 81, 31–38.
- Ertasgin, G., Whaley, D., Ertugrul, N, & Soong, W. (2019). Analysis of DC Link Energy storage for Single-Phase Grid-Connected PV Inverters. *Electronics*, 8(6), 601.
- Femia N, Petrone G, Spagnuolo G, & Vitelli M (2005). optimization of perturb and observe maximum power point tracking method. *IEEE Transactions on Power Electronics*, 20, 963–973.
- Gonzalez, R., Gubia, E., Lopez, J, & Marroyo, L. (2008). Transformerless Single-Phase Multilevel-Based Photovoltaic Inverter. *IEEE Transactions on Industrial Electronics*, 55(7), 2694-2702.

- Hu W, Ma W, & Liu C (2009). A novel AC PI controller and its applications on inverters. *2009 4th IEEE Conference on Industrial Electronics and Applications*, Xi'an, 2247–2251.
- Ishaque K, Salam Z, Amjad M, & Mekhilef S (2012). An improved particle swarm optimization (PSO)-Based MPPT for PV with Reduced Steady-State Oscillation. *IEEE Transactions on Power Electronics*, 27, 3627–3638.
- Islam M, Afrin N, & Mekhilef S (2016). A new high efficient transformerless inverter for single phase grid-tied photovoltaic system with reactive power control. *IEEE Transactions on Sustainable Energy*, 7, 1205–1215.
- Kjaer, S., Pedersen, J, & Blaabjerg, F. (2005). A Review of Single-Phase Grid-Connected Inverters for Photovoltaic Modules. *IEEE Transactions on Industry Applications*, 41(5), 1292-1306.
- Kakosimos PE, Kladas AG, & Manias SN (2013). fast photovoltaic-system voltage- or current-oriented MPPT employing a predictive digital current-controlled converter. *IEEE Transactions on Industrial Electronics*, 60, 5673–5685
- FreeVideo Lectures. (2019). *Pulse Width Modulation for Power Electronic Converters (Prof. G.Narayanan, IISc Bangalore): Lecture 38 - PWM for Three-level Neutral-point-clamped Inverter*. Retrieved September 5, 2019, from [https://freevidelectures.com/course/3345/pulse-width-modulation-for-power-electronic-converters/4 courses /electronics / PWM For Power Electronic Converters –IISc-Bangalore/lecture-38.html](https://freevidelectures.com/course/3345/pulse-width-modulation-for-power-electronic-converters/4%20courses%20/electronics%20/%20PWM%20For%20Power%20Electronic%20Converters%20%E2%80%93IISc-Bangalore/lecture-38.html).
- SolarPower Europe. (2018). *Global market outlook for solar power*. Retrieved February 1, 2018, from <http://www.solarpowereurope.org/wp-content/uploads/2018/09/Global-Market-Outlook-2018-2022.pdf>.

- Mattavelli P (2001). A closed-loop selective harmonic compensation for active filters. *IEEE transactions on Industry Applications*, 37, 81–89
- Nabae A, Takahashi I, & Akagi H (1981) A New Neutral-Point-Clamped PWM Inverter. *IEEE Transactions on Industry Applications IA-17*, 518–523.
- Teodorescu R, Blaabjerg F, Liserre M, & Loh P (2006). Proportional-resonant controllers and filters for grid-connected voltage-source converters. *IEE Proceedings - Electric Power Applications*, 5, 153-750
- Zengin S, Deveci F, & Boztepe M (2013). Decoupling Capacitor Selection in DCM Flyback PV Microinverters Considering Harmonic Distortion. *IEEE Transactions on Power Electronics*, 28, 816–825.